DYNAMIC MODELING OF SOLID OXIDE FUEL CELL SYSTEMS

FOR COMMERCIAL BUILDING APPLICATIONS

by

Andrew T. Schmidt

A thesis submitted to the Faculty and the Board of Trustees of the Colorado School of Mines in partial fulfillment of the requirements for the degree of Master of Science (Engineering).

Golden, Colorado

Date _____

Signed: _____

Andrew Schmidt

Signed: _____

Dr. Robert Braun

Thesis Advisor

Golden, Colorado

Date _____

Signed: _____

Dr. John Berger

Acting Department Head

Department of Mechanical Engineering

ABSTRACT

Integrating emerging distributed generation and renewable energy sources in a building has the potential to drastically improve the site's environmental impact, energy cost, and energy efficiency. With impending energy and environmental challenges, the successful application of these technologies is becoming increasingly important. There have been many technological and cost advances in photovoltaics, solid oxide fuel cells (SOFC), small-scale wind turbines, advanced batteries and thermal storage, which may lend themselves towards a commercial building or building cluster application on a micro-grid. When simulating these integrated systems, high-level steady-state optimization studies have shown several desired operating modes for the SOFC system including load-following and part-load operation. However, the proper control scheme (supervisory and/or detailed) of a solid-oxide fuel cell system in coordination with intermittent renewable energy sources remains unknown.

A dynamic SOFC system model has been developed for the purposes of performing an engineering feasibility analysis on recommended integrated system operating strategies for building applications. Included in the system model are a dynamic SOFC stack, dynamic steam pre-reformer and other balance-of-plant components, such as heat exchangers, pumps and a tail gas combustor. Model results show suitably fast electric power dynamics (~15 min) due to the fast mass transport and electrochemical dynamics within the SOFC stack. The thermal dynamics are slower (~25 min) due to the thermal coupling and thermal capacitance of the system. However, these transient results are shown to be greatly dependent upon SOFC system operating conditions. In addition, system design implications on system dynamic response are revealed. Results are summarized within the context building load profiles and demand requirements.

TABLE OF CONTENTS

LIST OF FIGURES

LIST OF TABLES

CHAPTER 1

INTRODUCTION

In this age of resource limitations, international tension and environmental concern, it is evident that energy efficiency, independence, and cleanliness are important to our way of life. Diminishing energy availability and international energy source security, as well as increasing energy costs and pollution levels are driving research into efficient and renewable energy conversion technologies. Centralized electric power production is and will remain to be a fundamental part of the energy infrastructure in the United States, but other options are becoming available that improve efficiency, reduce emissions, and have the potential to decrease costs to the end user. Distributed generation, specifically for building applications, is a customizable and versatile solution that can include any number of efficient technologies and can help manage the world's hunger for energy. This chapter explores the background in distributed generation, commercial building applications, and solid oxide fuel cell (SOFC) systems as a motivation for the research in this thesis.

1.1   Distributed Generation

Traditionally, large (>1MW) coal and/or natural gas fired power plants are situated outside densely populated areas to avoid polluting and congesting these areas. This necessitates the need for a transmission and distribution system that imparts a 7-8% busbar power loss [6]. As an alternative, decentralized electric power production systems, or distributed generation (DG) systems, can be adopted. Example DG systems may consist of a solitary photovoltaic array on a homeowner's property or a series of microturbines on a university campus. These systems may operate in order to keep the

owner completely disconnected from a centralized power plant (off-grid) or may only be used to supplement the power purchased from the local utility (on-grid). These systems are widely varied in application, design, use and purpose.

With erratic and unpredictable renewable resources like solar and wind power, a DG system has the potential to drastically under-perform as designed. Adding prime movers in the system that are controllable and fed by natural gas or renewable hydrogen will not only improve the DG system's consistency and reliability, but cost per kWh has the potential to be much less as the capacity factor is much higher. In addition, prime movers can produce thermal energy as well as electricity to integrate into a building heating ventilating and air conditioning (HVAC) or district heating system and improve system efficiency. This production and harnessing of thermal and electrical power is termed as combined heat and power (CHP) and can provide thermal efficiencies greater than 90%. An example prime mover is a microturbine which combusts fuel and turns a generator, much like centralized natural gas-fired turbines. Microturbines are versatile in terms of fuel sources but are not very electrically efficient. SOFC systems provide higher electrical efficiencies (~45%) and are also versatile with fuel sources. In addition, SOFCs produce electrical power with fewer moving parts and the potential for less maintenance when compared to microturbines.

There are many benefits and some drawbacks to this decentralized approach to power production. First, DG produces electricity very near to the end user, all but eliminating transmission losses and increasing overall efficiency. Second, DG has the potential to cost less than grid electricity, depending on the system location. Third, certain DG systems can be used to produce CHP thermal efficiencies greater than 90% whereas the U.S. national average for centralized power plant efficiency is closer to 30%. Many other advantages exist, including the potential for reduced emissions, improved reliability, and improved efficiency due to small-scale technologies not yet available for centralized applications. Unfortunately, these DG systems, no matter how simple, are quite expensive and require an initial capital investment. In addition, the location spark spread parameter, or the ratio between natural gas and grid electricity prices, dictate the attractiveness of DG as many DG systems are fueled by natural gas [34]. Essentially, the

spark spread parameter provides insight into the ratio of cost of energy from DG to cost of energy from centralized grid sources. Locations ideal for DG application have high grid electricity prices compared to natural gas price. This discrepancy in price must overcome the initial capital and operating costs of the DG system in order to be cost effective.

1.2   Commercial Building Applications for DG

Commercial buildings are ideal candidates for hosting DG systems. Commercial buildings comprise about 40% of the electricity demand in the United States [12]. This consumption of electricity and its associated emissions can be reduced by the application of DG. Rooftops and building sides are good locations for renewable technologies, such as photovoltaics, while prime movers, including microturbines and SOFC systems, can be installed close to the packaged HVAC units.

However, until recently, building integrated DG systems have not been optimized for cost or performance, but were typically installed to reduce the building's bottom line energy costs. In order to properly design the DG system, the building thermal and electric load profiles are considered as well as the renewable source profiles, such as wind speed and solar irradiance, at the intended system location. Figure 1-1 shows a yearly representative mid-week electric load profile for a medium office building located in Boulder, CO. In the evenings, the load is minimized by shutting the HVAC system off and turning off most lights, computers and other electrical devices. The HVAC system turns on at 5 am to prepare the building for occupancy. As the morning continues, the internal gains in the building increase, increasing the load on the HVAC system and electrical devices are switched on. During normal work hours, the non-HVAC load is relatively constant but the electrical load of the HVAC system is increasing due to the increasing ambient temperature and solar gains. Finally, in the evening electrical equipment is shut off, the HVAC system is turned off, and the process repeats. Due to the application, there is a peak in electrical load during the day and minimum demand at night. This follows the general profile of photovoltaic arrays where daily solar irradiance

is shaped as a bell curve with a peak in the early afternoon, suggesting photovoltaics may reduce the building's peak electricity demand and therefore energy cost.
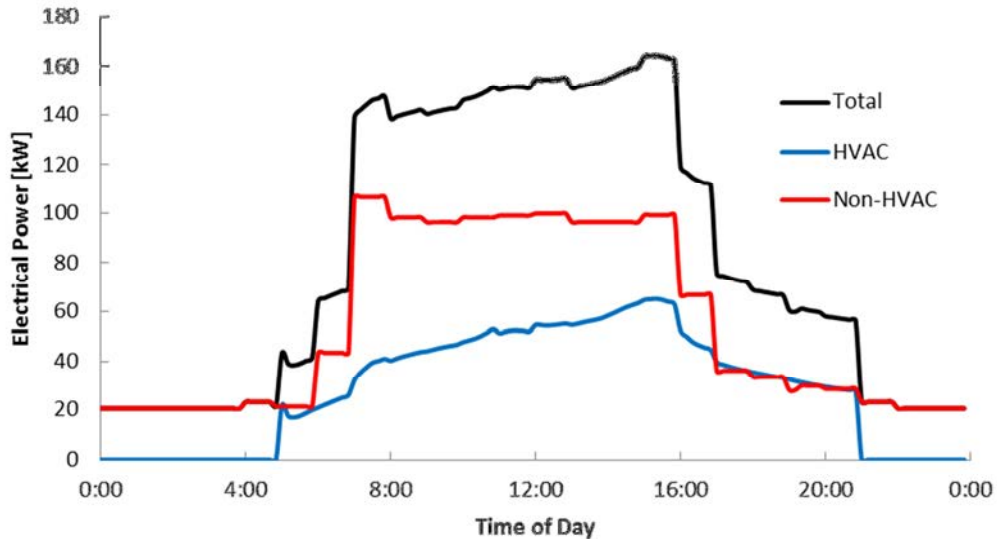
Figure 1-1 Electrical load profile for medium office building

Figure 1-2 shows the peak and representative thermal heating load of the medium office building in Boulder, CO during the winter season. "Operating average" is the load average when the system is on, while the "year average" is the load average taking the zero-load operation into account. For the representative day, the HVAC system is cycling in the early morning in order to maintain constant temperatures within the building. At about 5 am, the temperature setpoints increase to prepare the building for occupancy and the HVAC system adjusts accordingly. The heating load decreases through the morning due to increasing internal gains of occupancy and electrical equipment heat generation. In addition, the ambient temperature and solar irradiance on the building are increasing, reducing the heating load. In fact, thermal cooling is required for certain parts of the building at this time due to these gains. In the evening, ambient temperature, solar irradiance, and internal occupancy are decreasing, resulting in a higher heating load to maintain the temperature setpoints. Finally, at night, the temperature setpoints are reduced and the heating system maintains the lower temperature.

During normal working hours, the thermal load decreases as the electrical load increases, seemingly mirroring each other. This coupling between thermal and electrical demand suggests the application of a CHP system would be appropriate. A SOFC-CHP

system can be operated in modes that produce more thermal output and modes that produce more electrical output. If such a system is desired, dynamically controlling the SOFC system operating mode may be requested.
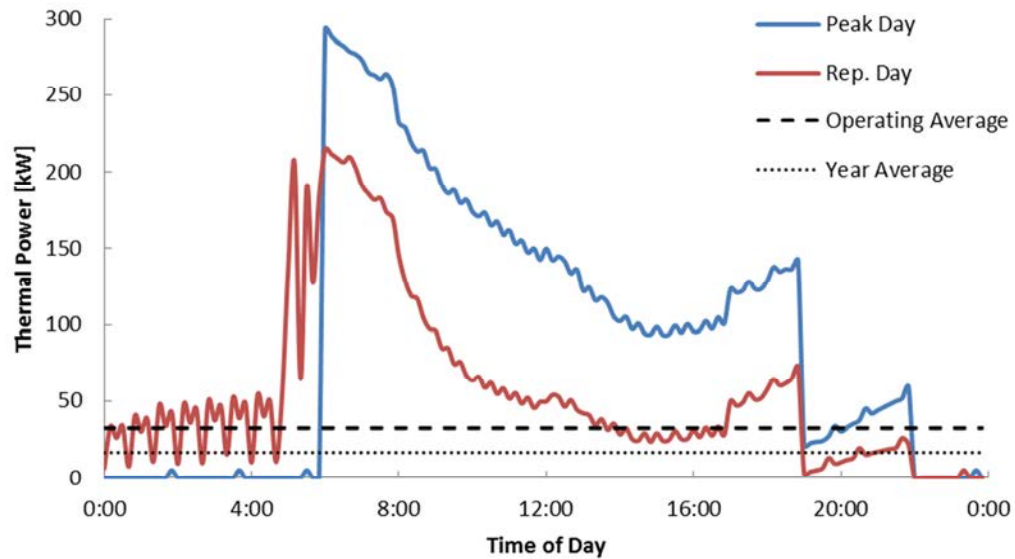
Figure 1-2 Thermal heating load profile for medium office building

Much research is being focused on optimizing DG systems for commercial building applications. Lawrence Berkeley National Laboratory has developed a mixed-integer linear program that has found optimal DG system designs that include photovoltaic arrays, small-scale wind turbines, electricity storage in the form of batteries, and prime movers such as reciprocating engines [33][35]. Pruitt et al. [27] and current research activity at Colorado School of Mines have also shown optimal system designs that include renewable sources, SOFC systems, and thermal and electrical storage. In order to save money over a grid-only building, this research has shown that dynamic operation of the SOFC system in the form of load-following may be required.

Figure 1-3 details example results of a commercial building-DG system design study for a large hotel in San Francisco, CA. This system design and operation results in a 30% decrease in life-cycle costs over a grid-only case while utilizing anticipated near-future technology costs [30]. The figure shows electrical load-following operation of the SOFC system throughout the day, while photovoltaics and wind turbines supplement this generation. Also evident in the figure is the large decrease in grid electricity purchase of the building. This decrease in grid electricity purchase more than covers the initial capital

of the DG system and its operating costs, resulting in cost savings. However, the dynamic capabilities of SOFC systems are, as of yet, relatively unexplored computationally or experimentally and it is yet to be seen whether desired cost optimal system operation is actually feasible. The purpose of this thesis is to develop the computational framework necessary to fully investigate the thermal and electrical dynamic capabilities of SOFC systems in commercial building applications.
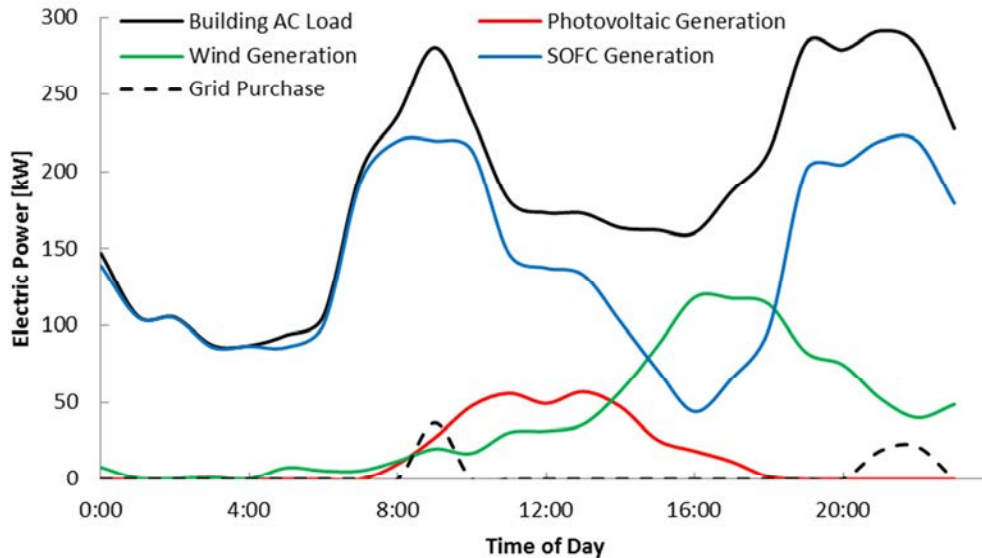
Figure 1-3 Example cost saving DG system operation for a large hotel in San Francisco

1.3   Solid Oxide Fuel Cell Systems as Prime Movers

SOFC systems have the potential to be cheaper, more efficient and cleaner than microturbines and are currently being researched heavily for centralized power plant and small-scale residential applications, alike. Fuel cells fundamentally act as a battery, where chemical energy is directly converted into useful electrical energy without combustion or mechanical parts. As can be seen in Figure 1-4, hydrogen diffuses through the anode diffusion layer to the electrolyte-anode interface. Concurrently, oxygen diffuses through the cathode diffusion layer to the electrolyte-cathode interface where oxygen is reduced, gaining electrons and becoming oxygen ions. These oxygen ions transport through the ceramic electrolyte to the anode where they react with the hydrogen to produce water and electrons. These electrons are then captured through a load circuit where they are then returned to the cathode to again reduce oxygen molecules.
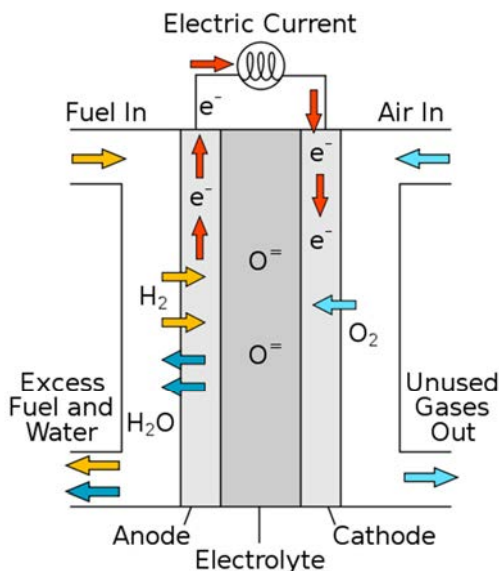
Figure 1-4 Overview of SOFC operation [16]

The table below details the electrochemical reactions occurring in a SOFC and their respective locations. Theoretically, this system's only emission is water vapor. However, any fuel can be used as an input to this system as long as a fuel reforming component prepares the fuel for use in the cell. The use of hydrocarbons inevitably results in emissions of carbon dioxide and carbon monoxide, but the higher efficiency of SOFCs results in fewer emissions per kWh_e produced.

Table 1-1 Electrochemical reactions in solid oxide fuel cells

Location	Reaction
Anode:	$H_2 + O^{2-} \rightarrow H_2O + 2e^-$
Cathode:	$\frac{1}{2} O_2 + 2e^- \rightarrow O^{2-}$
Overall:	$H_2 + \frac{1}{2} O_2 \rightarrow H_2O$

Individual cells generate less than 1 [V] of electric potential and must be assembled into an SOFC stack in order to produce useful voltages. Figure 1-5 illustrates this stack assembly where cells are laid on top of one another. The anode and cathode channel inlets and outlets are attached to manifolds that supply and collect fuel and air for each cell. Thermal coupling exists between individual cells due to the sharing of interconnect plates separating adjacent fuel and oxidant channel flows.
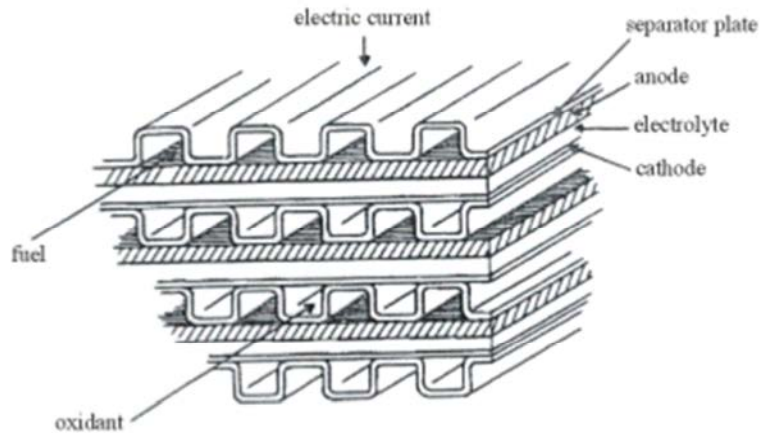
Figure 1-5 Co-flow SOFC stack assembly [9]

Additional components are required to support the stack, creating a SOFC system. Figure 1-6 outlines an example natural gas fueled SOFC system design using an external reformer, anode gas recycle and a tail gas combustor. Heat exchangers are required to heat the fuel and oxidant streams in order to sustain a high stack temperature. The external reformer may partially or fully convert the natural gas into hydrogen for consumption in the SOFC stack, while some reforming may be capable in the stack itself.
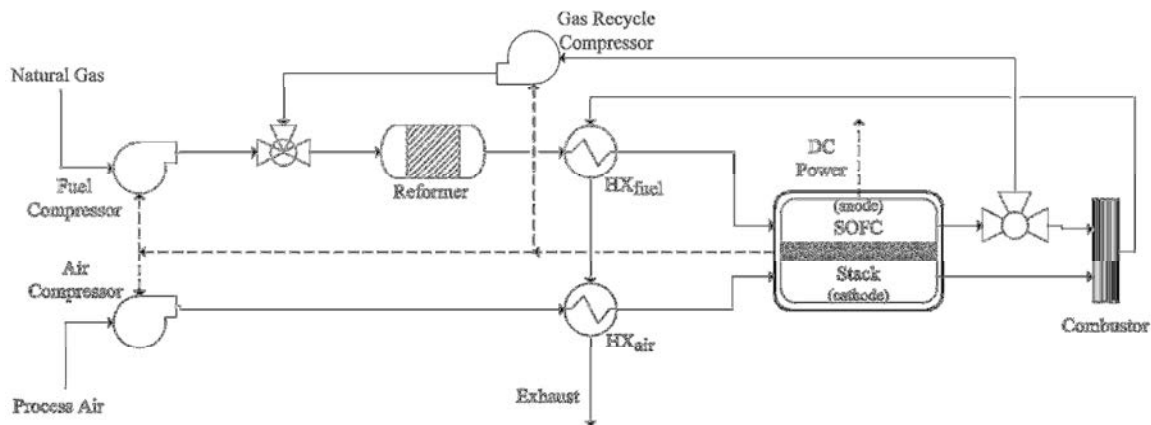
Figure 1-6 Example SOFC system design

SOFC systems also generate high quality exhaust heat which can be recovered and used in the building HVAC system. With SOFC operating temperatures as high as 1000 [℃] and system exhaust temperatures above 300 [℃], high quality exhaust heat can be recovered and used in a building HVAC system. Some SOFC-CHP systems have been shown to have the potential to reach system efficiencies of about 90% [6], or about three times as thermally efficient as centralized power plants.

1.4   Thesis Objectives

The primary objective of this research is to develop dynamic modeling tools that enable the transient simulation of SOFC systems. Due to the mass of the SOFC stack and reformer, and the coupling between stack inlet and outlet conditions, thermal and electrical dynamic response on the order of tens of minutes can be expected as a result of load and system input changes. Detailed investigation into this intra-system coupling and thermal and electrical dynamic response of the SOFC system must be performed to identify system dynamic capabilities and trends for commercial building integration. The objectives of this thesis can be understood as addressing the following statements:

1. Build intermediate-fidelity dynamic models of an SOFC stack and SOFC system.
2. Verify the SOFC stack model against data from literature.
3. Investigate the implications of the SOFC stack dynamic response on the challenges of integrating SOFC systems as load-following units.
4. Compare the dynamic responses of the SOFC stack to the SOFC system with the metrics of settling time and response shape.
5. Develop initial system level insights regarding the impact of SOFC system component configuration on SOFC system dynamic response/settling time.

1.5   Prior Work

Many dynamic SOFC stack computational models have been developed and documented in the scientific literature [1][3][5][14][15][17][19][22][25][28][31][39]. Additionally, very thorough SOFC system models have also been developed and analyzed [6][7][41]. However, few dynamic SOFC system models have been analyzed for total system dynamics and these studies have not been complete in their system modeling approach.

Murshed et al. [22] developed a dynamic, spatially lumped SOFC stack model that was combined with thermally dynamic system component models like tail gas combustor, heat exchangers and steam reformer for an approximate sizing of 20 [kW$_e$].

The SOFC stack model assumed a constant direct relationship between molar composition inside of the stack and flow rates out of the stack, as well as constant gas pressure within the stack. In addition, ohmic overpotential was assumed to be representative of all voltage losses. The modeling approach assumed instantaneous thermal response of gas flows with thermal storage only in the stack solid mass. The system model presented had a fuel heat exchanger upstream of the reformer, with reformer outlet gas supplied directly to the SOFC stack anode inlet. The dynamic system response to a +10% step in current had a thermal settling time on the order of 250 [s] and an electrical settling time of about 100 [s]. Both the electrical and thermal responses were non-oscillatory with a single overshoot and then slow approach towards steady state. This system dynamic response, as well as the presented dynamic response of the stand-alone SOFC stack, does not capture the more complex dynamic shape apparent in higher-fidelity SOFC stack models, thus suggesting an over-simplification in the stack model. In addition, presented thermal and electrical responses appear to be much faster than the dynamics presented in higher-fidelity stack model literature. The over-simplification of the stack model results in artificially simple system dynamic response and is considered insufficient for exploring system dynamics in the context of building integration.

Saarinen et al. [31] developed a dynamic SOFC stack model that was integrated into a system model in a one-dimensional computational fluid dynamics (CFD) modeling environment for an approximate sizing of 5 [kW_e]. As the model was developed to emulate an existing SOFC test station, the SOFC stack model is viewed as a stack within a furnace, which maintains a constant furnace temperature. The system model components included were three heat exchangers and an autothermal reformer. All system component models, excluding the stack, were verified with experimental data taken from the SOFC test system on which the system model was based. All methane entering the stack is assumed to be reformed, composition is assumed to be in constant water-gas shift equilibrium, and only ohmic overpotentials are considered in the electrochemical model. For +90% step in current, the dynamic system model resulted in electrical and thermal response times of about 4 [hr] and an over-dampened response with no overshoot and generally 1st order response. This system model is not representative of a true SOFC system as an installed system would not have the stack in

an enclosed furnace kept at a constant temperature. In addition, the shape of the dynamic response does not appear to capture the more complex dynamic response of higher-fidelity SOFC stack models. Although a higher-fidelity system component model was developed, the limited fidelity of the SOFC stack model renders this study unsuitable for the investigation of true SOFC system dynamics and their implications on building integration.

Xi [39] developed a dynamic, one-dimensional SOFC stack model that was combined with a dynamic, zero-dimensional reformer model. The dynamic stack model included mass and thermal dynamics for the two gas channels and two solid layers (anode-electrolye-cathode and interconnect). In addition, reaction rate equations for internal reforming were included as well as activation, ohmic, and concentration overpotentials in the electrochemical model. The stack model also assumed a constant direct relationship between mass flow rate and pressure drop in order to capture the physical phenomena governed by a momentum balance. The zero-dimensional dynamic catalytic partial oxidation (CPOX) reformer was modeled as solely thermally dynamic and the reformate exits the reformer at the reformer solid temperature. Gas supply manifolds for the CPOX reformer and SOFC stack cathode inlet were modeled as 1st order delays in order to replicate mass transfer dynamics upstream of the reformer and SOFC stack. The dynamic system response to a -50% step in current had a thermal settling time of about 1000 [s] and an electrical settling time of about 500 [s]. Both thermal and electrical dynamic responses exhibited high-order dynamic behavior with oscillations. Although efforts were made to emulate intra-system interaction between components, this study does not include or capture the effects of component coupling due to recuperative heat exchangers or gas recycle. Although it has its benefits for certain applications, CPOX reforming is not ideal for building applications as CPOX results in a nitrogen-rich anode feed stream that negatively impacts SOFC stack electrochemical performance. In addition, CPOX oxidizes some inlet fuel which can reduce system fuel efficiency depending on the system design. Thus, this study is considered insufficient to the investigation of SOFC systems for building applications and the associated dynamics.

1.6   Conclusions Drawn from Prior Work

The previously referenced studies from the literature investigate portions of the complete dynamic SOFC system, but each study neglects important aspects of the complete system. The simplified zero-dimensional SOFC stack model in Murshed et al. [22] does not capture the thermal and electrical dynamics of SOFC stacks shown in one-, two-, and three-dimensional models. In addition, the zero-dimensional construct does not allow for a complete understanding of the complex and spatially dependent interaction between stack mass and gas streams and the implications of these interactions on system components. Although fundamentally thorough in the fluid dynamics of enclosed systems, Saarinen et al. [31] does not include any spatially distributed temperature or reaction rate profiles in the SOFC stack model. In addition, as the system model developed represents a SOFC test facility and includes an autothermal reformer, it does not represent a SOFC system that would be used for building integration.

The approach of Xi [39] to dynamic SOFC stack modeling is very similar to the method described in Chapter 2. This study captures many of the SOFC stack dynamics and the interaction between the CPOX reformer and SOFC stack due to direct coupling. However, this system model does not include system coupling due to heat recuperation from exhaust gases or system design concepts like exhaust gas recycle. Additionally, SOFC systems including CPOX reformers are not as well suited to medium scale (>10 [kW]) stationary power production as external steam reforming.

This thesis investigates the dynamics of a complete and coupled SOFC system that no previous work has accomplished. Presented in this thesis is a thermochemically dynamic, spatially distributed SOFC stack model combined with a thermally dynamic external steam reformer model, as well as exhaust heat recuperation and exhaust gas recycle.

1.7   Modeling and Simulation Methodology

A dynamic SOFC stack model has been constructed in the Fortran language using literature as a guide. The stack model, detailed in Chapter 2, was created specifically to

be integrated into a SOFC system model where system dynamics could be investigated. This system model was designed and built in the TRNSYS environment [37], which is a transient system simulation tool. Available system components like heat exchangers and compressors are available to users who connect component inputs and outputs in order to build a connected thermal system. The SOFC system model is simulated with varying dynamic conditions in the TRNSYS software.

1.8   Thesis Outline

This thesis presents the modeling construct and steady state and dynamic results of a dynamic SOFC system for commercial building applications. Chapter 2 describes the dynamic SOFC stack model equations constructed as the main element dynamically and electrically in the SOFC system. Chapter 3 presents the SOFC stack model verification, steady state and dynamic results. Chapter 4 details the system component models including heat exchangers, compressors and a reformer. Chapter 5 presents the analysis of steady state and dynamic results of the complete SOFC system for multiple operating conditions and load changes. Chapter 6 includes a discussion of the SOFC system results in the context of commercial building applications and suggestions are made for future research opportunities.

CHAPTER 2

DYNAMIC SOLID OXIDE FUEL CELL MODEL

Fuel cell models can be developed with many different levels of detail according to their intended purpose. For example, a fuel cell anode design effort would require a multi-dimensional cell model with complex gas diffusion and chemical reaction mechanism models. In contrast, a thermal integration and packaging design team would require a one- or two-dimensional cell model with more emphasis on radiation heat transfer and manifolding considerations. As computer processors and clock speeds have continued to improve the balance between model fidelity and computational time has become less of an issue and high fidelity models are continually being developed. In the scope of this research, a one-dimensional cell-modeling approach with emphasis on cell-stack dynamic electrochemical and thermal performance is taken.

In this chapter, the approach for modeling a dynamic solid oxide fuel cell is detailed. First, model assumptions and simplifications are discussed followed by the electrochemical and thermochemical sub-models. Lastly, the numerical solution method is described along with a mesh sensitivity analysis.

2.1   The Need for and Scope of the Model

In the case of the problem described in Chapter 1, a dynamic solid-oxide fuel cell model is required to investigate dynamic capabilities and potential control strategies for building-integrated SOFC systems. As the electrical power output of the fuel cell is its primary function, the electrochemical model must be very accurate. Implicitly, the thermal properties and chemical composition of the gases play a large role in the electrical performance of the fuel cell. The thermal power output of the SOFC is also

very important for the system model where exhaust gases are used to preheat inlet gases and may also be used for further integration in commercial building HVAC systems. Therefore, the mass and heat transfer models must be accurate as well. This term, "accurate", must be defined: it means closely replicating the performance of a physical SOFC stack. Since no physical SOFC stack data is available, data from the literature will be used in its stead. Ideally, the percent error between the presented model and literature data will be zero, but this will not be the case as the models are different. This validation process and evaluation of model accuracy is further discussed in Chapter 3.

As is the case when developing any model, the question must be asked: what fidelity is necessary? Higher model fidelity results in longer computational time and more expensive hardware requirements. As the dynamic SOFC model will be integrated into a dynamic system model, computational time must be considered. Ideally, experimental data would be used to tune a high fidelity model and then a process of order reduction would take place to maintain accuracy to experimental data while decreasing computational requirements. However, a line must be drawn as to where one begins this high fidelity model development. In the scope of this research, time does not exist to create a three-dimensional model with complex mass transport and diffusion models.

Xi [39] evaluated several models with differing fidelity. The highest fidelity model in that paper was a 12 state model for each discretization unit, 8 composition states and 4 temperature states. This modeling approach also exists in other pieces of literature [3][14][17]. A variety of other levels of fidelity also exist in the literature. For example, Achenbach [1] developed a dynamic three dimensional, three temperature state model and Murshed et al. [22] developed a lumped (zero dimensional) dynamic SOFC model. By examining the literature, a middle ground was found with a one-dimensional, 12 states per spatial discretization unit model. Therefore, several assumptions have been made to simplify the SOFC model to decrease computational time while also maintaining a high level of accuracy. For example, axial radiation between spatial nodes is neglected, linear extrapolation between cell and stack models is assumed and the flow is assumed to be fully developed. A detailed list of assumptions and respective justifications are presented in Section 2.3.

2.2   General Approach

In order to accurately simulate the SOFC, certain and specific aspects of the fuel cell must be modeled and established. A list of these aspects is below.

1. Electrical charge balance on the solids
2. Gas hydrodynamics in the fuel and air channels
3. Mass balances of each species in the fuel and air channels
4. Chemical reaction rate expressions for methane reforming and associated reactions, hydrogen oxidation and oxygen reduction
5. Energy balances on both gas channels and both solids
6. Boundary conditions for inlet temperature, flow rates and composition and heat loss to surroundings
7. Property databases for thermodynamic, chemical and physical data

The above model components are explained in further detail in the following sections, where a planar, co-flow, Ni/YSZ, anode-supported SOFC is modeled. The model construct was built in the Fortran 90 language for integration into the Fortran based software, TRNSYS [37], which is used for modeling the entire SOFC system.

2.3   Assumptions

In order to develop the fuel cell stack model at an appropriate fidelity for the problem, a series of assumptions were made in order to simplify the numerical SOFC representation. The following section details the assumptions made in the fuel cell stack model and their respective reasoning.

1. One-dimensional fuel cell performance in axial direction

   This assumption limits the model to fuel cell designs where gas channels are in parallel, as other designs such as serpentine channels would require two- or three-dimensional models. However, for co- or counter-flow designs, this assumption is sufficient when considering the scope of the model, especially since the channels are relatively narrow [3][6].

2. Linear extrapolation between cell and stack models

This assumption is implied by assuming a one- or two- dimensional cell model. In reality, a temperature gradient will exist between central cells and the physical boundaries of the fuel cell stack. This assumption will overestimate fuel stack performance as lower performing cells exist within the stack and cell resistances due to cell stacking are not included within the model; however, this approach is typical in literature [1][6][25].

3. Manifolding and enclosure have negligible effect on boundaries

This assumption implies both adiabatic solid boundaries and uniform gas distribution to cells in all axes and simplifies the model by allowing for specification of fixed boundary conditions at the gaseous and solid material boundaries. A physical fuel cell stack will have heat transfer from the cell ends to the stack enclosure which decreases performance. Also, gas distribution would not be uniform in all axes and would result in thermal hot spots and mass transport effects. Such effects are neglected as the research is performed assuming optimized fuel cell system component designs [1][3][6][14][25].

4. Axial radiation between solids is neglected

Radiation between the discretized PEN structure and interconnect solids is assumed to be only between the solids in the respective discretization unit. When considering a high aspect ratio channel, the surface directly across from the radiating surface will have the highest view factor. Quantitatively, the view factor is 0.884 between surfaces in the same discretization unit using a view factor relationship for offset parallel rectangles (46 units, dimensions from Table 3-1). The view factor will decrease with increasing number of nodes, but the addition of this heat transfer component hardly affects cell performance [3][14][39].

5. Discretized gas channels perform as continually stirred tank reactors (CSTR) and fuel cell performs as plug flow reactor

In each discretized unit, flow and temperature variations are ignored as each unit is assumed to be well mixed. This is due to high mass and heat transfer coefficients that result in small concentration and temperature variations across the gas channels in the discretized unit. Plug flow reactor performance can be assumed due to high Peclet number and low Reynolds number [1][3][6][14][25].

6. Lumped solid temperatures

   Temperature gradients within the solids normal to bulk gas velocity do exist in reality and, with moderate effort, can be modeled using conductive heat transfer relationships. Considering that the cell solid layers are thin, intra-cell temperature gradients normal to bulk gas velocity are assumed negligible [3][6][14][22].

7. Internal electronic resistance of electrodes for current collection are negligible

   This assumption allows for an isopotential condition across the unit cell which greatly simplifies the numerical problem by eliminating circuit analysis. This is reasonable as the electrodes are primarily highly conductive metals in order to promote current collection [3][6][14][39].

8. Electrochemical reactions result in 100% current efficiency

   Referring to the efficiency between charge transport and available electrical power, this assumption states that all available charge transport from the oxidation of hydrogen is able to perform electrical work outside the SOFC stack. Also, no electrochemical side reactions occur [3][6][14][39].

9. Fully developed flow

   Due to the low Reynolds number, the mass and heat transport are assumed to be laminar in the unit cell. In addition, the flow is assumed to be fully developed as entry lengths are calculated to be much less than the overall length of the cell. This assumption allows for a constant Nusselt number for the flow resulting in a direct relationship between convective and conductive heat transfer coefficients [3][6][14][39].

2.4   Electrochemical Model

The task of the electrochemical model is to accurately model the electrochemical reactions and relationships that enable prediction of electric power production from the solid oxide fuel cell device. First, an understanding of the electrochemical processes in the fuel cell is established.
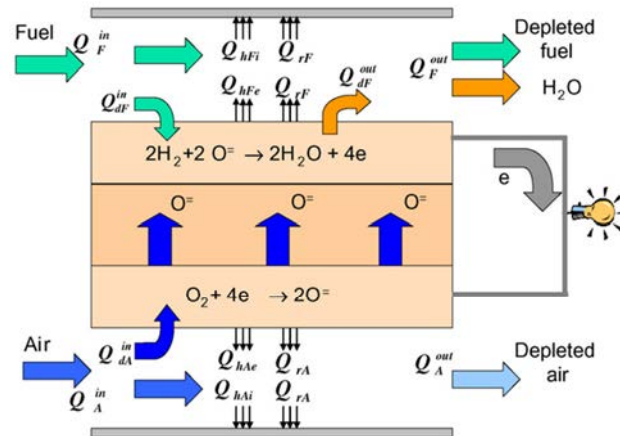
Figure 2-1 Overview of electrochemical process in fuel cells [22]

As can be seen in Figure 2-1, hydrogen diffuses through the anode diffusion layer to the electrolyte-anode interface. Concurrently, oxygen diffuses through the cathode diffusion layer to the electrolyte-cathode interface where oxygen is reduced and gains electrons. These oxygen ions transport through the electrolyte to the anode where they react with the hydrogen to produce water and electrons. These electrons are then captured through a load circuit where they are then returned to the cathode to again reduce oxygen molecules. The table below details the electrochemical reactions occurring.

Table 2-1 Electrochemical reactions in solid oxide fuel cells

Location	Reaction
Anode:	$H_2 + O^{2-} \rightarrow H_2O + 2e^-$
Cathode:	$\frac{1}{2} O_2 + 2e^- \rightarrow O^{2-}$
Overall:	$H_2 + \frac{1}{2} O_2 \rightarrow H_2O$

At the anode, the electron "production" is seen via the oxidation of hydrogen, while at the cathode, the electron "consumption" is seen via the reduction of oxygen. This process is driven by the thermochemical affinity of hydrogen and oxygen to be in the

form of water vapor. The electrochemical cell potential is established from the overall reaction affinity.

2.4.1 Nernst Potential

In order to find the cell operating voltage, the open circuit voltage (OCV) must first be calculated. This is calculated using the Nernst equation presented below as found in O'Hayre et al. [24]:

$$E_N = -\frac{\Delta G°}{nF} - \frac{RT}{nF} \ln \frac{\prod\limits_{\text{Products}} a_i^{v_i}}{\prod\limits_{\text{Reactants}} a_i^{v_i}} \tag{2.1}$$

where E_N is the Nernst potential or OCV, $\Delta G°$ is the resulting change in Gibbs free energy in the overall electrochemical reaction, n is the number of moles of free electrons associated with the reaction, a_i is the activity of species i, and v_i is the stoichiometric coefficient of species i in the overall reaction as given in Table 2-1. The activity can be represented using partial pressures of the participating species and standard state pressure. When applying this definition of activity to the redox reaction occurring in the SOFC, the following equation for OCV is found:

$$E_N = -\frac{\Delta G°}{2F} - \frac{RT}{2F} \ln \frac{\left(p_{H_2O} / p^0 \right)}{\left(p_{H_2} / p^0 \right) \cdot \left(p_{O_2} / p^0 \right)^{1/2}} \tag{2.2}$$

where p_i is the partial pressure of species i, p^0 is the standard state pressure (1 [atm] or 101325 [Pa]) and "2" is the number of free electrons associated with the redox reaction occurring in the SOFC.

2.4.2 Concentration Overpotential

The concentration overpotential is the reduction in cell potential related to mass transport resistance within the electrode diffusion layers. It is within the porous solid where the redox relevant gases diffuse in order to reach the reaction sites at the

electrolyte-electrode boundaries. These reaction sites are called the triple point boundaries (TPB) where electrolyte, electrode and catalyst meet. As the current density increases, the rate of consumption of oxygen and hydrogen increases at a faster rate than the diffusion rate of the gas through the porous electrode.

The concentration overpotentials for the anode and cathode are calculated via the following equations as developed by Aguiar et al. [3]:

$$\eta_{conc,anode} = \frac{RT}{2F} \ln\left(\frac{p_{H_2O,\text{TPB}} \cdot p_{H_2,f}}{p_{H_2O,f} \cdot p_{H_2,\text{TPB}}} \right) \tag{2.3}$$

$$\eta_{conc,cathode} = \frac{RT}{4F} \ln\left(\frac{p_{O_2,a}}{p_{O_2,\text{TPB}}} \right) \tag{2.4}$$

where $p_{i,j}$ is the bulk partial pressure of species i in channel j, and $p_{i,\text{TPB}}$ is the partial pressure of species i at the TPB. The difference in n, which is four for the air channel and two for the fuel channel, is due to the difference in free electrons per mole of reactant in each redox half reaction. Each mole of oxygen and hydrogen, which are both diatomic molecules, contain four and two moles of free electrons, respectively. The relationships between bulk partial pressure, local current density and partial pressure at the TPB for the three species are presented below. The anode diffusion is modeled as an equimolar, counter-current one-dimensional diffusion process and the cathode diffusion is modeled as one-dimensional, self-diffusion according to Aguiar et al. [3] (see also [14][39]).

$$p_{H_2,\text{TPB}} = p_{H_2,f} - \frac{RT\tau_{anode}}{2FD_{eff,anode}} j \tag{2.5}$$

$$p_{H_2O,\text{TPB}} = p_{H_2O,f} + \frac{RT\tau_{anode}}{2FD_{eff,anode}} j \tag{2.6}$$

$$p_{O_2,\text{TPB}} = P_{tot,a} - \left(P_{tot,a} - p_{O_2,a}\right)\exp\left(\frac{RT\tau_{cathode}}{4FD_{eff,cathode}P_{tot,a}} j \right) \tag{2.7}$$

In the equations above, j is the local current density, τ_{anode} and $\tau_{cathode}$ are the thicknesses of the anode and cathode diffusion layers, respectively, and $D_{eff,I}$ is the

effective diffusion coefficient of diffusion layer i. The effective diffusion coefficient for species i, $D_{\mathrm{eff},i}$, is calculated with the following relationship:

$$D_{\mathrm{eff},i} = \frac{\varepsilon_{\mathrm{p}}}{\tau_{\mathrm{tortuosity}}} D_{\mathrm{molecular},i} \qquad (2.8)$$

where ε_{p} is the material porosity, $\tau_{\mathrm{tortuosity}}$ is the tortuosity factor of the material, and $D_{\mathrm{molecular},i}$ is the molecular diffusivity of species i. The material porosity is the percentage of electrode volume that is void space for gases to diffuse through. The tortuosity factor is a measure of both the increased distance the molecules must travel as compared to the geometric electrode thickness and the flow constriction due to changing flow-area due to the non-crystal structure of the electrode. This relationship essentially modifies the gaseous diffusion properties with the porous material diffusion properties.

The molecular diffusivity incorporates both the fluid-fluid and fluid-wall collision mechanism in diffusional transport processes. These mechanisms are mathematically combined via the following relationship:

$$\frac{1}{D_{\mathrm{molecular},i}} = \frac{1}{D_{\mathrm{bulk},i}} + \frac{1}{D_{\mathrm{knudsen},i}} \qquad (2.9)$$

where $D_{\mathrm{bulk},i}$ is the gaseous diffusion property based on the kinetic theory of gases and $D_{\mathrm{knudsen},i}$ is the Knudsen diffusion coefficient that includes material and gaseous properties.

2.4.3 Activation Overpotential

In reaction chemistry, the system must overcome the activation energy, or activation barrier, in order for a reaction to occur. The activation barrier can be exemplified by a spark initiating combustion of fuel. In this case, the spark is providing the required energy to overcome the activation barrier of the combustion reaction in order to initiate combustion. The magnitude of the activation barrier is dependent upon the free energy of the products and reactants. In electrochemical reactions, a certain amount of electric potential is required to overcome the activation barrier of the redox reaction. This

complex reaction chemistry loss component is modeled with the Butler-Volmer equation. This equation calculates the net reaction rate according to the individual forward and backward reaction rates of the redox reaction as follows,

$$j = j_{0,\text{electrode}} \left[\exp\left(\frac{\alpha n F}{RT} \eta_{\text{act,electrode}} \right) - \exp\left(-\frac{(1-\alpha)nF}{RT} \eta_{\text{act,electrode}} \right) \right] \qquad (2.10)$$

where j is the local current density, $j_{0,\text{electrode}}$ is the exchange current density, α is the transfer coefficient, and $\eta_{\text{act,electrode}}$ is the activation overpotential. The transfer coefficient, a measure of the reaction symmetry, is typically taken to be 0.5. The exchange current density is essentially the forward and backward reaction rates at thermodynamic equilibrium. The exchange current density is calculated according to the following relationship:

$$j_{0,\text{electrode}} = \frac{RT}{nF} k_{\text{electrode}} \exp\left(-\frac{E_{\text{electrode}}}{RT} \right) \qquad (2.11)$$

where $k_{\text{electrode}}$ is the pre-exponential factor and $E_{\text{electrode}}$ is the activation energy for the half-reaction occurring at the electrode.

When mass transfer and current transfer occur at similar rates, the Butler-Volmer equation must be modified. The corrected Butler-Volmer equation is shown below as reported by Aguiar et al. [3]. This correction only need be applied to the anode as the correction for the cathode is negligible.

$$j = j_{0,\text{anode}} \left[\frac{p_{H_2,\text{TPB}}}{p_{H_2,\text{f}}} \exp\left(\frac{\alpha n F}{RT} \eta_{\text{act,anode}} \right) - \frac{p_{H_2O,\text{TPB}}}{p_{H_2O,\text{f}}} \exp\left(-\frac{(1-\alpha)nF}{RT} \eta_{\text{act,anode}} \right) \right] \quad (2.12)$$

When applying the typical transfer coefficient and the free electrons, the Butler-Volmer equation can be simplified to the equation below for the cathode.

$$\eta_{\text{act,cathode}} = \frac{RT}{F} \sinh^{-1}\left(\frac{j}{2 j_{0,\text{cathode}}} \right) \qquad (2.13)$$

2.4.4 Ohmic Overpotential

The third and final overpotential is caused by the resistance of the electrolyte to charge transport (both ionic and electronic) through the cell layers. This Ohmic overpotential is calculated according to the following relationship between resistance and current density:

$$\eta_{ohm} = R \cdot j \cdot A_{dis} \tag{2.14}$$

where R is the combined ionic and electronic resistance of the PEN structure, j is the local current density and A_{dis} is the cross-planar area of the discretized fuel cell. The series resistances are combined according to the following:

$$R = \left(\frac{\tau_{anode}}{\sigma_{anode}} + \frac{\tau_{electrolyte}}{\sigma_{electrolyte}} + \frac{\tau_{cathode}}{\sigma_{cathode}} \right) \cdot \frac{1}{A_{dis}} \tag{2.15}$$

where τ_i is the thickness and σ_i is the conductivity of PEN component i. The conductivity used for the electrodes is the electronic conductivity while the ionic conductivity is used for the electrolyte.

2.4.5 Operating Voltage

Having calculated the OCV and assorted overpotentials for the fuel cell, the operating voltage can now be calculated. According to the following relationship:

$$V = E_N - \left(\eta_{conc,anode} + \eta_{conc,cathode} + \eta_{act,anode} + \eta_{act,anode} + \eta_{ohm} \right) \tag{2.16}$$

As temperature increases, the activation losses decrease due to the increased thermal energy in the system, the ohmic losses decrease due to increased ionic conductivity of the electrolyte at high temperatures and the concentration losses increase due to decreased mass transport to reaction sites. As current density increases, the activation losses increase due to the increased rate of energy required to overcome the activation energy, the ohmic losses increase due to Ohm's law and the concentration losses increase due to a growing gap between reaction rate and mass transport.

2.5   Thermochemical Model

In addition to an electrochemical model, a model is needed that captures the internal fuel reforming, heat transfer and mass transfer. First, it is necessary to discuss the chemical species that are present in this fuel cell model. In this research, methane (CH_4) is used to simulate natural gas due to the fact that methane comprises at least 80% of natural gas. This natural gas is then converted in a combination of pre-reformer and internal reforming to produce carbon dioxide (CO_2), carbon monoxide (CO), hydrogen (H_2) and water (H_2O). These species are present in the fuel channel in the model. Nitrogen (N_2) is also added as a possible species in the fuel channel as some pre-reformers (CPOX, ATR) combine air and fuel to reform the fuel which results in nitrogen at the inlet to the fuel cell. In this model, a mixture of 21% oxygen (O_2) and 79% nitrogen are used to model atmospheric air. As these two components make up more than 99% of air, this is a reasonable simplification. Therefore, nitrogen and oxygen are the only two species present in the air channel.

As this model is of a natural gas fed SOFC that has internal reforming capabilities, the reforming reactions must be defined. The first reaction modeled is the steam reforming (SR) reaction where methane reacts with steam (water vapor) to produce carbon monoxide and hydrogen. This highly endothermic reaction is the main internal reforming driving reaction and produces the majority of the hydrogen which is needed for the electricity producing reaction. The mildly exothermic and kinetically fast water-gas shift (WGS) reaction is also modeled where carbon monoxide reacts with water vapor to produce carbon dioxide and hydrogen. Lastly, the reduction-oxidation (redox) reaction that drives the electrochemical properties of the SOFC is modeled. These chemical reaction equations are presented in Table 2-2.

Table 2-2 Present chemical reactions and their locations

Location	Reaction	Chemical Expression
Fuel channel	SR	$CH_4 + H_2O \rightarrow CO + 3H_2$
	WGS	$CO + H_2O \leftrightarrow CO_2 + H_2$
Anode	Ox.	$H_2 + O^{2-} \rightarrow H_2O + 2e^-$
Cathode	Red.	$0.5O_2 + 2e^- \rightarrow O^{2-}$

The following sections detail the mass and energy balances that are created in order to derive the dynamic equations that will define the thermochemical portion of the SOFC model. Each discretized cell unit has twelve dynamic states: six fuel channel species concentrations (CH_4, CO_2, CO, H_2O, H_2, N_2), two air channel species concentrations (N_2, O_2), two gas temperatures (fuel and air channels), and two solid temperatures (PEN, interconnect). Figure 2-2 illustrates the discretized units and how the outlet conditions of one unit are the inlet conditions of the adjacent unit. The pink and green arrows represent mass and energy transport and the blue arrows represent conductive heat transfer between control volumes. The equations presented in this section are for an arbitrary discretized unit i, unless otherwise stated.
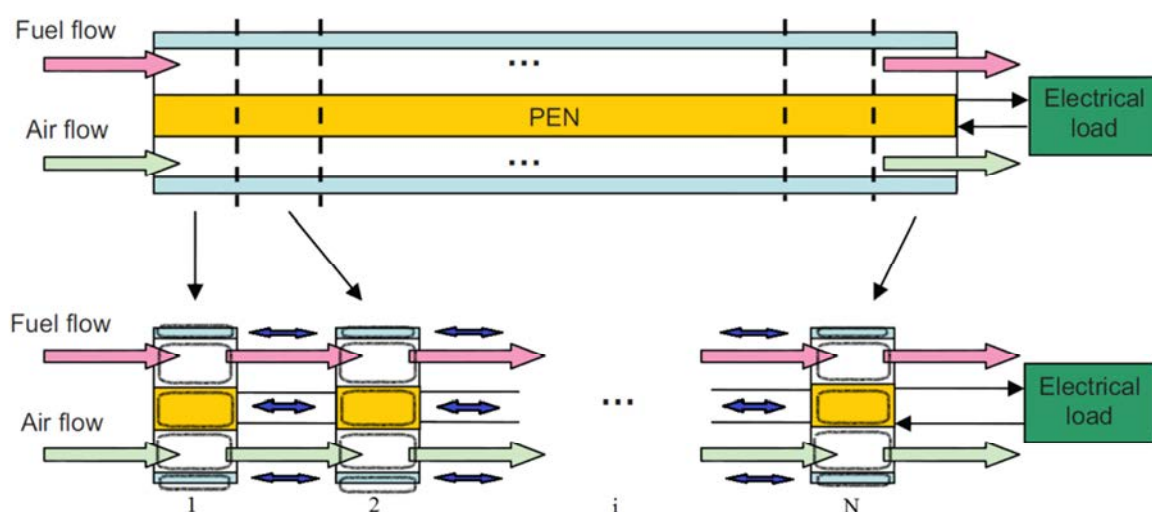
Figure 2-2 Discretization scheme overview [39]

2.5.1 Material Balances

The first major component of the dynamic thermochemical model is the dynamic material balance. For a control volume (see Figure 2-2), the material balance accounts for the storage of mass (or atoms), the net flow of mass, and the production or consumption of the gas species. The differential element of the balance is the time dependent storage of mass which can be accounted for by number of moles, amount of mass, density, or concentration within the control volume. All components of the balance will vary with

time, but there is only one differential variable. In order to remain consistent with the majority of literature, the mass balance was created around the species concentration and is shown in Equation (2.17). This equation is then applied for each species in the fuel channel.

$$\frac{dC_{s_f}}{dt} = \left(\dot{n}_{in,s_f} - \dot{n}_{out,s_f}\right)\frac{1}{V_f} + \sum_{k \in \{SR,WGS,Ox\}} v_{s_f,k}\dot{r}_k \frac{1}{d_f} \tag{2.17}$$

$$s_f \in \{CH_4, CO_2, CO, H_2O, H_2, N_2\}$$

dC_{s_f}/dt is the dynamic storage of atoms in the control volume and differentiates this model from a steady-state model where this would be zero. The middle terms are the molar flow rates into and out of the control volume while the final term is change in moles of a species due to reactions. In the fuel channel, the possible reactions are SR, WGS or Red.

The current density can be used to calculate the reaction rate of the reduction-oxidation reaction occurring at the electrodes. Since the electrochemical processes occurring in the fuel cell are assumed to be instantaneous, it follows that the reduction reaction rate must be equal to the oxidation reaction rate. Faraday's law is then used to arrive at the following relationship:

$$\dot{r}_{Red} = \dot{r}_{Ox} = \frac{j}{2F} \tag{2.18}$$

The reaction rate equation for steam reforming derived by Achenbach and Riensche [2] is employed here. Equation (2.19) details this reaction rate equation:

$$\dot{r}_{SR} = k_0 p_{CH_4} \exp\left(-\frac{E_a}{RT_f}\right) \tag{2.19}$$

with a pre-exponential constant of $k_0 = 0.04274$ [mol s^{-1} m^{-2} Pa^{-1}] and an activation energy of $E_a = 82$ [kJ mol^{-1}].

WGS is assumed to be the third and final possible reaction in the fuel channel. Aguiar et al. [3] developed this reaction rate expression for the equilibrium reaction:

$$\dot{r}_{WGS} = k_{WGS} p_{CO} \left(1 - \frac{p_{CO_2} p_{H_2}}{p_{CO} p_{H_2O} K_{eq,WGS}} \right) \tag{2.20}$$

Where $K_{eq,WGS}$ is the equilibrium constant of the WGS reaction as calculated by a curve fit of data from Moran and Shapiro [21]. Aguiar et al. [3] assume an "arbitrarily high" coefficient k_{WGS} in order to represent the fast kinetics of the WGS reaction. The unit system employed here is based on Pascal and, considering the unit conversion, a value of $k_{WGS} = 0.01$ [mol s^{-1} m^{-2} Pa^{-1}] is chosen. This value best replicates the data from the literature.

The species outlet molar flow rate from the discretized unit is calculated below via the bulk gas velocity and species concentration in the unit. The continually stirred tank reactor and plug flow reactor assumptions are applied here where the concentration of the outlet flow is equal to the concentration of the mass within the control volume.

$$\dot{n}^i_{out,s_f} = u^i_{out,f} C^i_{s_f} A_{c,f} \tag{2.21}$$

The velocity of the gas is assumed to be equal for each species present in the gas. Velocity varies down the length of the cell and is calculated via Equation (2.22). It should be noted that this relationship between mass flow rate and pressure drop is very important in that it takes the place of a full momentum balance that would be required to accurately capture the pressure drop down the length of the cell. Iora et al. [14] produced a SOFC model that included a momentum balance that explicitly modeled the shear stress on the gas at the channel walls. However, as will be shown, the simplification made in this research provides results comparable to the literature while simplifying the numerical problem of solving Navier-Stokes equations for gas channel flows.

$$u^i_{out,f} = \frac{\alpha^i_f \left(p^{i-1}_{tot,f} - p^i_{tot,f} \right)}{\rho^i_{bulk,f} A_{c,f}} \tag{2.22}$$

where α_f is derived by Kee et al. [18] to be:

$$\alpha^i_f = \frac{1}{\mathrm{Re}\, f} \frac{D_{h,f}^2 A_{c,f}}{2 L_{dis}} \frac{\rho^i_{bulk,f}}{\mu^i_{bulk,f}} \tag{2.23}$$

where $\rho_{bulk,f}$ is the fuel channel bulk gas density, $D_{h,f}$ is the hydraulic diameter of the fuel channel, L_{dis} is the length of the discretized unit, $A_{c,f}$ is the cross-sectional area of the fuel channel, and $\mu_{bulk,f}$ is the fuel channel bulk gas viscosity. Ref was shown to be defined as the following by Shah and London [32]:

$$\mathrm{Re}\,f = 14.227 + 1402.5\left(a - \frac{\sqrt{2}}{8}\right)^{1.90}$$

$$where \quad a = \frac{1+b\left(\sqrt{2}-1\right)}{4\left(1+b\right)}; \quad b = \frac{d}{W}$$

(2.24)

where d is the channel height and W is the channel width.

The mass balance in the air channel is calculated in much the same way as the fuel channel. The two differences are the possible reactions and species present. In the air channel, only the reduction reaction may occur and only diatomic nitrogen and oxygen may exist. The following is the mathematical representation of the air channel molar balance.

$$\frac{dC_{s_a}}{dt} = \left(\dot{n}_{in,s_a} - \dot{n}_{out,s_a}\right)\frac{1}{V_a} + v_{s_a,Red}\,\dot{r}_{Red}\,\frac{1}{d_a} \qquad s_a \in \{N_2, O_2\}$$

(2.25)

The reduction reaction rate is calculated in Equation (2.18). Exactly as in the fuel channel, the species molar flow rate out of the discretized unit is directly related to the species molar concentration within the unit and the bulk gas velocity out of the unit. The bulk velocity is calculated via the mass flow rate and pressure difference relationship in Equation (2.22). Bulk viscosity, density and geometric properties are calculated again for the air channel.

2.5.2   Energy Balances

In order to calculate dynamic temperatures of the gas channels and solids, energy balances must be established around the control volumes and control masses, respectively (see Figure 2-2). These energy balances take into account all transfer of energy into and

out of the control volumes via heat transfer, mass transfer and chemical reactions as well as the dynamic storage of energy within the control volume. It is this dynamic storage of energy that is used to calculate the temperature of the control volume.

2.5.2.1 Fuel Channel Energy Balance

A useful fuel channel energy balance can be derived from the following energy balance. The term on the left hand side of the equation is the dynamic storage of internal energy (e_{s_f}) in the fuel channel gas species. The first term on the right hand side is the enthalpy flux due to mass transport in and out of the control volume. The middle term represents the convective heat transfer between the fuel channel gas and surrounding solids. The final term is related to the oxidation reaction occurring at the anode surface where it is assumed that water vapor is produced at the temperature of the PEN solid.

$$\frac{d}{dt}\left(\sum_{s_f} C_{s_f} e_{s_f}\right) = \left(\dot{q}_{in,f} - \dot{q}_{out,f}\right)\frac{1}{l} + \left[h_{f,PEN}\left(T_{PEN} - T_f\right) + h_{f,Int}\left(T_{Int} - T_f\right)\right]\frac{1}{d_f}$$
$$+ \dot{r}_{Ox}\left[h_{H_2O}\left(T_{PEN}\right) - h_{H_2}\left(T_f\right)\right]\frac{1}{d_f}$$

(2.26)

After performing the product rule and applying the relationship between internal energy and enthalpy, the dynamic fuel channel temperature can be isolated:

$$\sum_{s_f} c_{v,s_f} C_{s_f} \frac{dT_f}{dt} = -\sum_{s_f}\left(h_{s_f}\left(T_f\right) - RT_f\right)\frac{dC_{s_f}}{dt} + \left(\dot{q}_{in,f} - \dot{q}_{out,f}\right)\frac{1}{l}$$
$$+ \left[h_{f,PEN}\left(T_{PEN} - T_f\right) + h_{f,Int}\left(T_{Int} - T_f\right)\right]\frac{1}{d_f}$$
$$+ \dot{r}_{Ox}\left[h_{H_2O}\left(T_{PEN}\right) - h_{H_2}\left(T_f\right)\right]\frac{1}{d_f}$$

(2.27)

where $h_{f,PEN}$ and $h_{f,Int}$ are the convective heat transfer coefficients between the fuel channel gas and the PEN and interconnect solids, respectively. The left hand side represents the changing energy of the system due to temperature change of the material. The first term on the right hand side represents the changing energy of the system due to composition changes within the control volume. The enthalpy flux out of the control volume is defined by the following relationship:

$$\dot{q}_{out,f} = u_{out,f} \sum_{s_f} C_{s_f} h_{s_f} \left(T_f \right) \tag{2.28}$$

$h_{s_f}(T_f)$ signifies the molar enthalpy of species s_f at temperature T_f. This enthalpy data includes the heat of formation which results in an energy balance without heat of reactions (ΔH_{rxn}).

2.5.2.2 Air Channel Energy Balance

The air channel energy balance is derived in the same manner as the fuel channel. The resulting energy balance is shown in the below equation. The two differences between this equation and Equation are the present species and the final term due to the mass transport associated with the reduction reaction.

$$\sum_{s_a} c_{v,s_a} C_{s_a} \frac{dT_a}{dt} = -\sum_{s_a} \left(h_{s_a} \left(T_a \right) - RT_a \right) \frac{dC_{s_a}}{dt} + \left(\dot{q}_{in,a} - \dot{q}_{out,a} \right) \frac{1}{l}$$
$$+ \left[h_{a,PEN} \left(T_{PEN} - T_a \right) + h_{a,Int} \left(T_{Int} - T_a \right) \right] \frac{1}{d_a} - 0.5 \dot{r}_{Red} h_{O_2} \left(T_a \right) \frac{1}{d_a} \tag{2.29}$$

The reduction reaction term is multiplied by one half due to the stoichiometric coefficient in the reduction reaction. Each oxygen atom contributes two electrons to the overall redox reaction while each hydrogen atom accepts only one electron. In essence, the reaction rate for the reduction reaction is half that of the oxidation reaction. As in the fuel channel, the enthalpy flux out of the control volume due to mass transport is calculated by the equation:

$$\dot{q}_{out,a} = u_{out,a} \sum_{s_a} C_{s_a} h_{s_a} \left(T_a \right) \tag{2.30}$$

2.5.2.3 PEN Solid Energy Balance

With a control volume established on the PEN solid in the discretized unit, an energy balance can be created. The following equation details the PEN energy balance.

$$\rho_{PEN} c_{p,PEN} \frac{dT_{PEN}}{dt} = q_{cond,PEN} \frac{1}{L_{dis}} - jV \frac{1}{\tau_{PEN}} + \frac{\sigma \left(T_{Int}{}^4 - T_{PEN}{}^4 \right)}{1/\varepsilon_{Int} + 1/\varepsilon_{PEN} - 1} \cdot \frac{1}{\tau_{PEN}}$$

$$- \left[h_{f,PEN} \left(T_{PEN} - T_f \right) + h_{a,PEN} \left(T_{PEN} - T_a \right) \right] \frac{1}{\tau_{PEN}} \qquad (2.31)$$

$$+ \dot{r}_{Ox} \left[h_{H_2} \left(T_f \right) + 0.5 h_{O_2} \left(T_a \right) - h_{H_2O} \left(T_{PEN} \right) \right] \frac{1}{\tau_{PEN}}$$

The left hand side of the equation quantifies the changing energy in the control mass due to changing temperature of the solid. The first term on the right hand side is the heat transfer into the control mass due to conduction axially in the PEN solid. The second term is the energy lost from the control mass due to the electrical work performed by the cell. The third term is the radiation heat transfer from the interconnect solid to the PEN solid. Finally, the last two terms are the convective heat transfer and energy transfer due to the redox reaction, respectively. These terms are the opposite in sign of their respective terms in the fuel and air channel energy balances. τ_{PEN} is the thickness of the PEN solid, σ is the Stephan-Boltzmann constant, and ε_{Int} and ε_{PEN} are the emissivities of the interconnect and PEN solids, respectively.

2.5.2.4 Interconnect Solid Energy Balance

With a control volume defined on the interconnect solid in the discretized unit, an energy balance can also be created. The following equation details the interconnect energy balance.

$$\rho_{Int} c_{p,Int} \frac{dT_{Int}}{dt} = q_{cond,Int} \frac{1}{L_{dis}} - \frac{\sigma \left(T_{Int}{}^4 - T_{PEN}{}^4 \right)}{1/\varepsilon_{Int} + 1/\varepsilon_{PEN} - 1} \cdot \frac{1}{\tau_{Int}}$$

$$- \left[h_{f,Int} \left(T_{Int} - T_f \right) + h_{a,Int} \left(T_{Int} - T_a \right) \right] \frac{1}{\tau_{Int}} \qquad (2.32)$$

The left hand side of the equation quantifies the changing energy in the control mass due to changing temperature of the interconnect solid. The first term on the right hand side is the heat transfer into the control mass due to conduction axially in the interconnect solid. The second term is the radiation heat transfer from the interconnect solid to the PEN solid. Finally, the last term is the convective heat transfer to the gas channels. The

radiation and convection terms are the opposite in sign of their respective terms in the fuel and air channel and PEN solid energy balances.

2.5.3 Boundary Conditions

As mentioned in Section 2.3, the inlet and exhaust manifolding and stack enclosure effects are neglected in this model. This allows for an adiabatic boundary condition at x=0 and x=L for the solids since convection and radiation are neglected at these locations. This is enforced by creating fictitious nodes beyond the boundaries of the fuel cell solids whose temperatures are set to the temperatures of the solids at x=0 and x=L according to their location. This allows for the same solid conductive heat transfer equation to be used at every node and mimics the application of an adiabatic boundary. In terms of the fuel and air channels, the gas channel inlets are at temperature, flow rate and composition conditions set by the model operator or upstream fuel processing equipment. The model boundary conditions are summarized in the table below.

Table 2-3 SOFC model boundary conditions

Location	Boundary Condition		
Fuel channel	$T_f(x=0)=T_{f\|inlet}$	$\dot{n}_{in,f}(x=0)=\dot{n}_{f\|inlet}$	$x_{s_f}(x=0)=x_{s_f\|inlet}$
Air channel	$T_a(x=0)=T_{a\|inlet}$	$\dot{n}_{in,a}(x=0)=\dot{n}_{a\|inlet}$	$x_{s_a}(x=0)=x_{s_a\|inlet}$
PEN solid	$\dot{Q}(x=0)=\dot{Q}(x=L)=0$		
Interconnect solid	$\dot{Q}(x=0)=\dot{Q}(x=L)=0$		

2.5.4 Transport and Thermodynamic Properties

The convective heat transfer coefficients from the previous energy balances are calculated with the bulk thermal conductivity according to the following Nusselt number relationship:

$$Nu = \frac{hD_h}{k} \qquad (2.33)$$

where k is the thermal conductivity, Nu is the Nusselt number and D_h is the hydraulic diameter of the channel. Empirical relationships exist for Nusselt number for only isothermal and isochoric boundary conditions. Although neither of these quite fit the problem at hand, the isothermal condition is closer to the problem, logically, due to the isothermal assumption on the discretization unit level. Shah and London [32] curve fit experimental data to find the following relationship for Nusselt number in rectangular ducts with an isothermal boundary condition:

$$Nu_T = 7.541\left(1 - 2.610\alpha + 4.970\alpha^2 - 5.119\alpha^3 + 2.702\alpha^4 - 0.548\alpha^5\right) \qquad (2.34)$$

where α is the aspect ratio: channel height over channel width.

The convective heat transfer coefficient in Equation (2.33) varies down the length of the cell due to the varying composition which changes the bulk conductivity, k. Many methods to calculate the bulk conductivity and bulk viscosity of a gas mixture exist. In this research, the method of Wilke [38] is adopted to calculate the bulk viscosity and is detailed in the following equation:

$$\mu_{bulk} = \sum_{i=1}^{n} \frac{x_i \mu_i}{\sum_{j=1}^{n} x_j \phi_{ij}} \quad where \quad \phi_{ij} = \frac{\left[1 + \left(\mu_i/\mu_j\right)^{\frac{1}{2}} \cdot \left(M_j/M_i\right)^{\frac{1}{4}}\right]^2}{\left[8\left(1 + M_i/M_j\right)\right]^{\frac{1}{2}}} \qquad (2.35)$$

where μ_i is the viscosity of species i, n is the number of species present in the channel, x_i is the molar fraction of species i, and M_i is the molecular weight of species i. This bulk viscosity value is used in Equation (2.23) for the coefficient relating mass flow rate and pressure drop.

The method of Wassilijewa with the Mason and Saxena modification, according to Reid et al. [29], is used to calculate the bulk thermal conductivity. The equation below details this relationship where the equation for ϕ_{ij} in Equation (2.35) is used again.

$$k_{bulk} = \sum_{i=1}^{n} \frac{x_i k_i}{\sum_{j=1}^{n} x_j \phi_{ij}} \qquad (2.36)$$

Appropriate thermodynamic properties that are required for the energy and mass balances are all temperature dependent in the real world and are modeled as such. Properties like thermal conductivity, viscosity, specific heat and, of course, enthalpy are gathered as functions of temperature from Engineering Equation Solver (EES) [13] and curve fitted with third order polynomials.

2.6   Numerical Solution Technique

The discretization units are solved as whole, coupled system using the finite difference method for the spatial temperature derivative in the axial solid conduction heat transfer. The exact equation for calculating the conductive heat transfer is shown below:

$$q_{cond}^i = k\left(T^{i+1} + T^{i-1} - 2T^i\right)\frac{1}{L_{dis}} \tag{2.37}$$

where k_{PEN} is the thermal conductivity of the solid material, L_{dis} is the discretized unit length and T^i is the temperature of spatial unit i. Re-enforcing the statement in Section 3.5.3, the solid boundary conditions are enforced by setting $T^0 = T^1$ and $T^{N+1} = T^N$ which is setting the conductive heat transfer to zero at the boundary.

In addition to the solid conductive heat transfer, discretized units are coupled via flow rates and enthalpy fluxes according to the equations below.

$$\dot{n}_{in,s}^i = \dot{n}_{out,s}^{i-1} \tag{2.38}$$
$$\dot{q}_{in,s}^i = \dot{q}_{out,s}^{i-1} \tag{2.39}$$

where $\dot{n}_{in,s}^i$ is the molar flow rate of species s into discretization unit i and $\dot{n}_{out,s}^{i-1}$ is the molar flow rate of species s out of unit (i-1). $\dot{q}_{in,s}^i$ is the enthalpy flux into discretization unit i and $\dot{q}_{out,s}^{i-1}$ is the enthalpy flux out of unit (i-1). These equalities are valid since adjacent control volumes share a boundary where mass and energy transfer across. At the gas channel inlet boundaries, the molar flow rates, $\dot{n}_{s|inlet}$, are set as model inputs.

Several performance metrics must also be defined for the use in this document. Fuel utilization is a ratio of the amount of fuel that is actually consumed by the chemical reactions in the SOFC to the amount of fuel provided to the cell. Several mathematical definitions of this metric exist, but the definition presented in Equation (2.40) is commonly employed in the literature [3][14][39].

$$U_{fuel} = \frac{J_{cell}}{\left(4x_{CH_4} + x_{H_2} + x_{CO}\right)n_{electrons} \cdot F \cdot \dot{n}_{fuel|inlet}} \tag{2.40}$$

where J_{cell} is the total current produced by the SOFC, x_s is the molar fraction of species s in the fuel supply, $n_{electrons}$ is the number of free electrons available from hydrogen (taken to be 2), F is Faraday's constant and $\dot{n}_{fuel|inlet}$ is the total molar flow rate at the inlet of the fuel channel.

The air stoichiometric ratio must also be defined. This is a relative measure of the amount of air to the stoichiometric requirement for the redox reaction. Equation (2.41) defines this metric:

$$\lambda_{air} = \frac{x_{O_2}\dot{n}_{air|inlet}}{J/4F} \tag{2.41}$$

where x_{O_2} is the molar fraction of oxygen in the air supply and $\dot{n}_{air|inlet}$ is the total molar flow rate at the inlet of the air channel.

The electrochemical model required its own solution algorithm. This is required since the model input is the average current density across the cell, or the total current requirement of the cell. An iterative method was required to solve for local current density and cell voltage under the requirement of constant axial cell voltage. An available solver from Press et al. [26], named "zbrent", was used as a function zero finder. Since both voltage and local current density must be solved for, zbrent algorithms for each local current density were nested within a zbrent algorithm for overall voltage. More simply, the inner zbrent loop takes a requested cell voltage and calculates the local current densities to create that cell voltage. The outer zbrent loop adjusts cell voltage to create the

requested average current density. The zbrent function makes this nested algorithm very efficient and accurate.

In all, with 76 nodes and with 12 states per node (eight species concentrations and four temperatures), the entire system has a size of 912 states. As the entire system is a numerical system of differential and algebraic equations (DAE), the implicit solver in time, LIMEX [11], is implemented. This solver calculates the Jacobian of the system in order to find the optimal time step. This is very useful when compared to a stiff timestep approach, such as Euler's method, which required a timestep of less than 0.00001 seconds for convergence. Integrating this flexible solver into the model required light manipulation of the model equations and solver construct. For example, the governing differential equations were reorganized into a matrix representation resembling a state-space representation and additional, non-state data was organized into arrays for transfer between sub-programs.
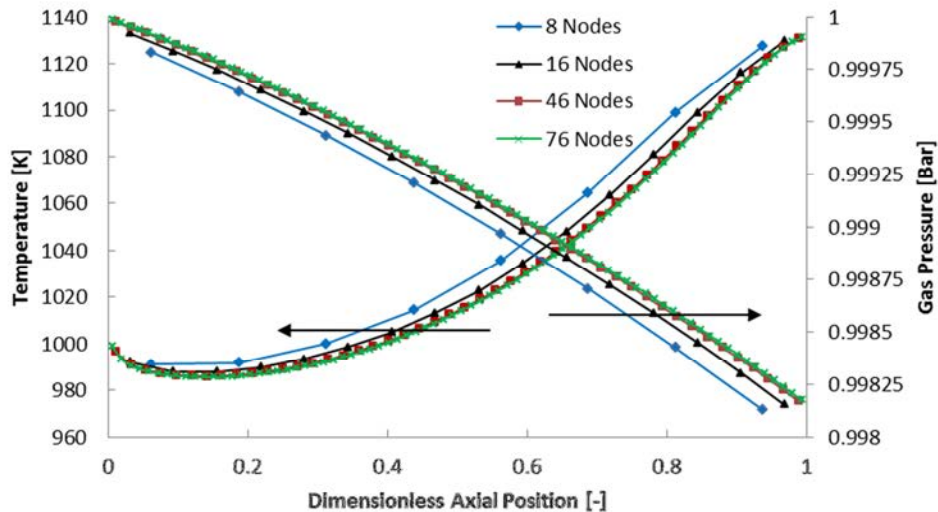
Figure 2-3 SOFC PEN solid temperature and fuel channel bulk pressure as functions of axial position in the cell with a range of node densities

The number of spatial nodes within the SOFC model affects the resolution of the key state variable distributions within a cell, and thereby impacts the validity of the results. Thus, a sufficient node density must be chosen to ensure a reasonable representation of the physical gradients, such as temperature and current density, within the cell. Figure 2-3 details the effects of number of nodes on steady state temperature and

pressure profiles in the PEN structure and fuel channel, respectively. All presented node densities produce the same general shape, but as the number of nodes increase, the changes in spatial profiles diminish. The change in calculated cell voltage between 46 and 76 nodes was ~0.14%, suggesting that such an increase in spatial resolution is unnecessary.
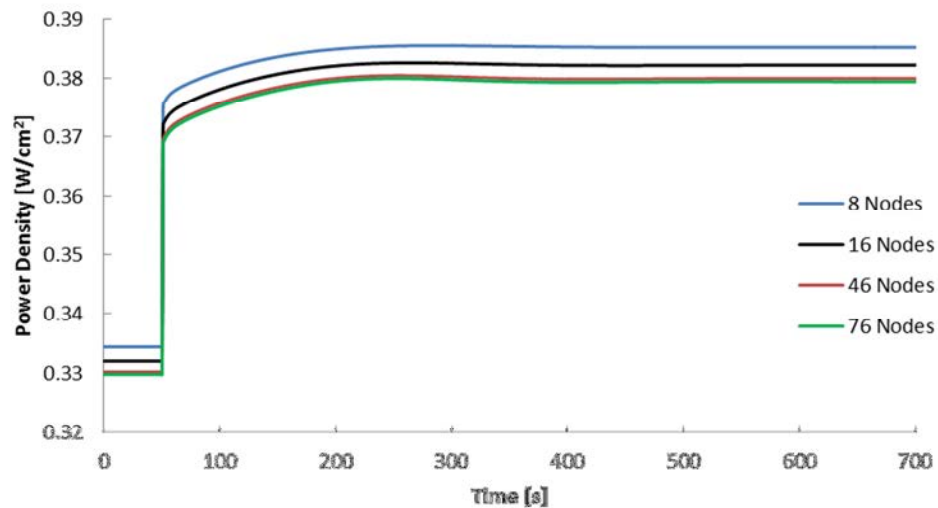
Figure 2-4 SOFC power density as functions of time

The effect of node density on dynamic performance was also investigated. Figure 2-4 shows the dynamic response of cell power density to a current step of 100 [mA/cm^2] as function of grid meshing. The general dynamic shape is preserved across the range of node densities; although, the resulting steady state results are separated again due to the different node densities. Quantitatively, the resulting percent overshoot was 0.0722%, 0.133% and 0.141% for the 8, 46 and 76 node cases, respectively. This is a 5.7% error between the 46 and 76 node cases, but the magnitude of error is very slight. Interestingly, the time of maximum overshoot occurs at different times: 285 [s], 254 [s] and 252 [s] for the same respective cases. Therefore, although it appeared to be dynamically similar, the 8 node case is still 13% off of the 76 node case. This error in timing of maximum overshoot is less than 1% between the 46 and 76 node cases. Based on these steady state and dynamic results, a current density of 46 nodes was chosen as a sufficient balance between accuracy and computational time.

CHAPTER 3

DYNAMIC SOLID OXIDE FUEL CELL MODEL VALIDATION AND CHARACTERISTICS

The dynamic model developed in the previous chapter is a sophisticated tool for simulating the complicated, time-varying physics within a solid oxide fuel cell. The aim of the present chapter is to verify the integrity of the model and gauge its relative precision in predicting the dynamic performance of solid oxide fuel cell stacks at the commercial scale (>10 [kW]). Given the sparse availability of experimental data for model validation, model integrity and output results are verified by comparison to other dynamic models found in the literature.

Once the computational model is verified through results benchmarking, the model parameters are altered to fit a representative stationary SOFC stack design. With a particular stack geometry specified, the chapter concludes with an exploration of the steady state and dynamic stack operating characteristics.

3.1 Model Verification

Verifying the SOFC model requires benchmarking the components of the model in both steady state and dynamic operation. Since the electrochemical sub-model, which is described in Section 2.4, is crucial to the prediction of electricity production in the SOFC, it is validated separately. The overall SOFC model is validated in Section 3.1.2. The main literature studies used to validate the model are that of Aguiar et al. [3][4] and Iora et al. [14]. Aguiar et al. developed a dynamic SOFC model using material and energy balances, but neglected momentum balance, instead favoring a more simplified model formulation that assumed a constant gas velocity throughout the gas channels. By

setting the gas velocity constant, the model produces an increasing gas pressure down the length of the cell. This is not representative of a true system where fluids flow in the direction of decreasing pressure. In contrast, Iora et al. generated a dynamic SOFC model that uses the full Navier-Stokes equations which has the potential to more fully capture the hydrodynamic interactions within the cell. The model by Iora et al. also included the electrochemical model by Aguiar et al. The model presented in this thesis does not include a momentum balance, but uses a computationally simpler method to replicate the physical phenomena captured by the full Navier-Stokes equations.

3.1.1   Electrochemical Sub-model

Aguiar et al. [3] published electrochemical sub-model data including operating voltage, OCV, overpotentials and power density. This data was presented for SOFC parameters shown in Table 3-1, which are then used to calculate the same data for the electrochemical sub-model created in Section 2.4.

Table 3-1 SOFC model parameters for characterization and validation

Parameter	Value	Units	Parameter	Value	Units
SOFC Dimensions:					
Length:	0.1	m	Anode Thickness:	500	μm
Width:	0.4	m	Electrolyte Thickness:	20	μm
Fuel Channel Height:	1	mm	Cathode Thickness:	50	μm
Air Channel Height:	1	mm	Interconnect Thickness:	500	μm
Anode Properties:			**Cathode Properties:**		
Electrical Conductivity:	80E3	$\Omega^{-1}m^{-1}$	Electrical Conductivity:	8.4E3	$\Omega^{-1}m^{-1}$
Diffusion Coefficient:	3.66E-5	m^2s^{-1}	Diffusion Coefficient:	1.37E-5	m^2s^{-1}
PEN Properties:			**Interconnect Properties:**		
Density:	5900	$kg\ m^{-3}$	Density:	8000	$kg\ m^{-3}$
Thermal Conductivity:	2	$J\ m^{-1}s^{-1}K^{-1}$	Thermal Conductivity:	25	$J\ m^{-1}s^{-1}K^{-1}$
Emissivity:	0.8		Emissivity:	0.1	
Heat Capacity:	500	$J\ kg^{-1}K^{-1}$	Heat Capacity:	500	$J\ kg^{-1}K^{-1}$
Electrolyte Ionic Conductivity:		$33.4E3exp(-10.3E3/T_{PEN})$	$\Omega^{-1}m^{-1}$		

The SOFC inlet conditions were set to an undepleted, fully reformed methane and steam mixture (molar steam to carbon ratio (s/c)=2; x_{H_2O}=0.1667, x_{H_2}=0.6667) with a cell temperature of 1073 [K], gas pressures of 1 [Bar] and undepleted air at the cathode. The results of the presented model and those of Aguiar et al. are shown in Figure 3-1 where "Cath." signifies the cathode, "Act." signifies activation loss and "Con." signifies concentration loss. The lines are the presented model data while the symbols are from Aguiar et al. Very good agreement between the two electrochemical models is obtained with the deviation between model outputs much less than 1%. With these highly favorable conditions, the maximum power density occurs at 2.07 [A/cm^2] which points toward an advanced SOFC design. As the SOFC will not be operating under such conditions, further analysis is moot. Electrochemical performance is discussed further in Section 4.2.
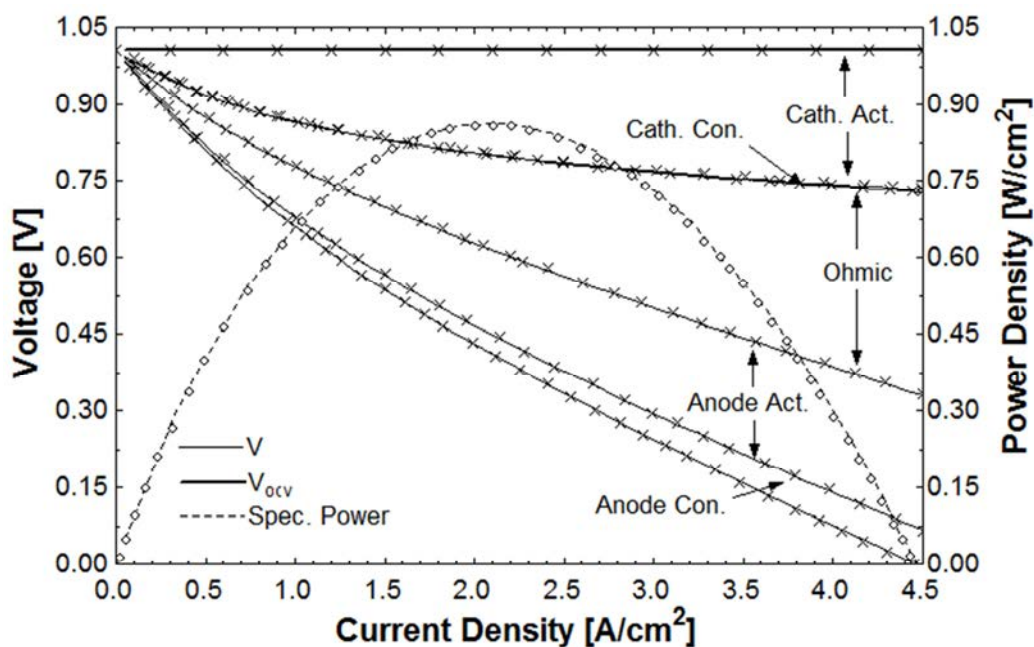
Figure 3-1 SOFC voltage and power density as functions of current density according to parameters in Table 3-1

3.1.2 Steady State SOFC Operation

In addition to the electrochemical model, the thermochemical model is verified by examination of local material temperatures and composition which greatly influence the thermal and electrical output of the SOFC. The outlet conditions are important when

considering that the SOFC is only a part of a system of components that exists to support the SOFC. For this test, presented data from Aguiar et al. [3] and Iora et al. [14] may be applied. The table below describes the operating conditions for the steady state performance validation.

Table 3-2 SOFC operating conditions for characterization and validation

Parameter	Value	Units	Parameter	Value	Units
Fuel Utilization:	75%		Air Ratio:	8.5	
Fuel Temperature:	1023	K	Air Temperature:	1023	K
Fuel Pressure:	1	Bar	Air Pressure:	1	Bar
Fuel Composition:	s/c = 2; 10% pre-reformed		Air Composition:	21% O_2, 79% N_2	
	28.1% CH_4, 2.7% CO_2, 0.5% CO, 56.7% H_2O, 12% H_2				
Average Current Density:	0.5	A cm^{-2}			

The table above describes the fuel composition that results after 10% pre-reforming of methane and achievement of water-gas shift equilibrium. Atmospheric air is used as the cathode oxidant gas. Fuel utilization and air stoichiometric ratio are defined the same in both this document and Aguiar et al. and Iora et al (see Equations (2.40) and (2.41)). The Nusselt number was 3.09 for these model runs. Under these operating conditions, the presented model produced an operating cell voltage of 0.660 [V] and a power density of 0.330 [W/cm^2]. These results are within 0.5% error[1] of data from Aguiar et al. and Iora et al.

Figure 3-2 details the steady state composition profiles for methane, water vapor and hydrogen for the presented model and literature. The crosses mark data from Iora and the points mark data from Aguiar. The maximum error between the literature and the presented model for the hydrogen molar fraction is about 0.8% and 2% for Iora et al. and Aguiar et al., respectively. This error is well within the acceptable range and it is encouraging that the presented model is closer to the more accurate model of Iora et al. This validates the material balances and chemical reactions (redox, SR, WGS) within the presented model.

---

[1] Error is defined as percent error: 100%*(Literature-Model)/Literature
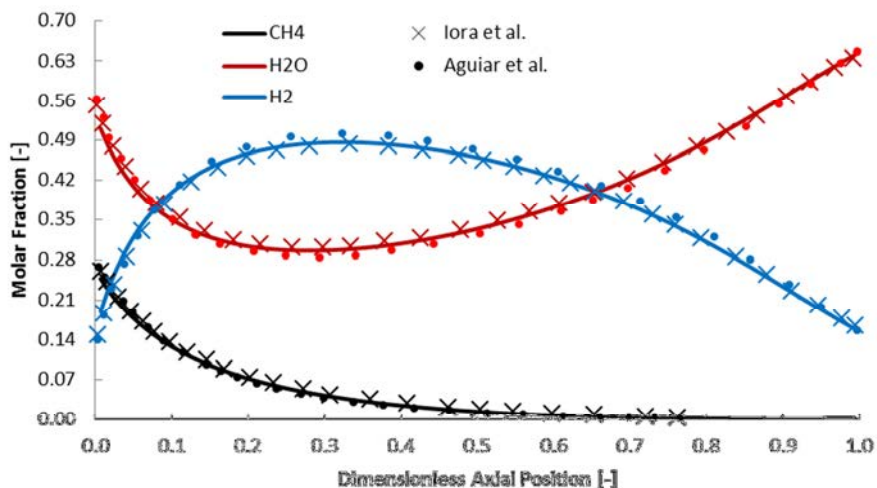
Figure 3-2 Steady state SOFC composition profiles for methane, water vapor and hydrogen for the operating conditions presented in Table 3-2

Figure 3-3 details the temperature profiles within the two gas channels of the SOFC. The maximum percent error for the fuel channel temperature is 0.01% and 0.7% for Iora et al. and Aguiar et al., respectively. Although the magnitude of error between the temperature data seems larger than that of the composition data, the percent error is actually less for the temperature data. Again, the model output is observed to be in excellent agreement the model of Iora et al. Thus, thermochemical model integrity is considered to be satisfactorily demonstrated.
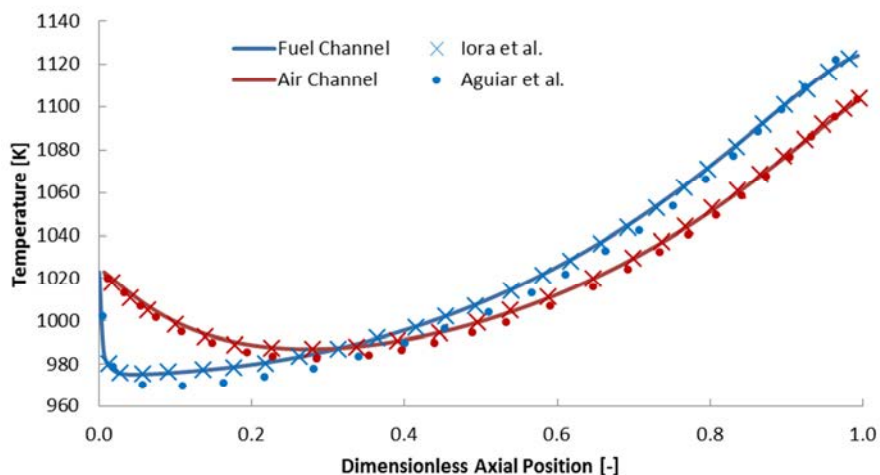
Figure 3-3 Steady state SOFC temperature profiles for the fuel and air channels for the operating conditions presented in Table 3-2

It is important to validate the hydrodynamic equations shown in Equations (2.22)-(2.24) that are intended to emulate a gas phase momentum balance in the reactant gas channels. Figure 3-4 details the pressure, velocity and density profiles in the fuel channel for both the presented model and the Iora model. The maximum deviation between the velocity data is much less than 1%. Thus, hydrodynamic integrity is considered to be satisfactorily demonstrated.
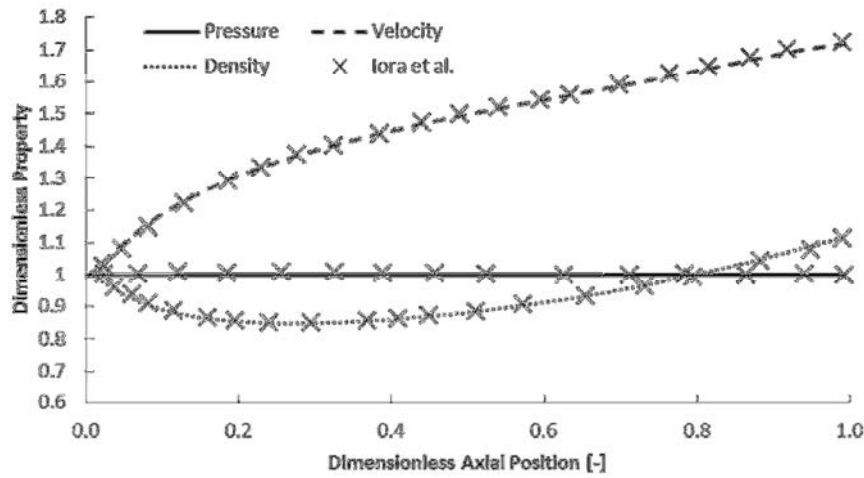
Figure 3-4 Steady state SOFC hydrodynamic data profiles in the fuel channel for the operating conditions presented in Table 3-2

3.1.3 Dynamic SOFC Model Benchmarking

In addition to the steady state operation, benchmarking of dynamic SOFC model output is explored. Aguiar et al. [4] presented dynamic response results for current steps from 0.5 to 0.6 [A/cm^2] and 0.5 to 0.4 [A/cm^2]. Figure 3-5 shows the fuel channel outlet temperature as a function of time for the presented model and the Aguiar model. The cross marks data from the Aguiar model. All error is within 1% for this dynamic temperature data which is acceptable, especially considering the difference between the two model constructs.

Figure 3-6 details results for the presented model and Iora et al. model [14]. In this case, the current density is being ramped from 0.5 to 0.7 [A/cm^2] between time 0 and 60 [s] and then the subsequent dynamics to steady state operation. Fuel channel exit temperature and operating cell voltage data are both presented. The average percent error

is less than 0.1% and 1% for the temperature and voltage data, respectively. The dynamics of the presented model appear to capture all of the dynamics within the literature models. Again, the presented model is well within the acceptable error range and is closer in performance to the Iora model than the Aguiar model.
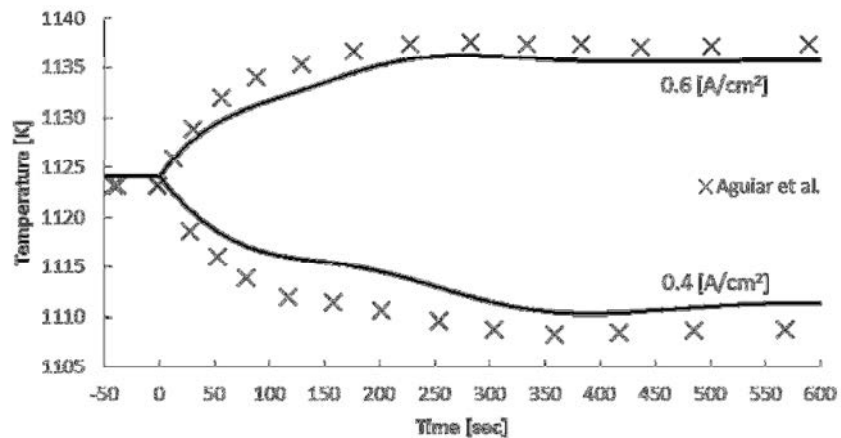
Figure 3-5 Dynamic SOFC fuel channel outlet temperature for comparison to Aguiar et al. [4] results
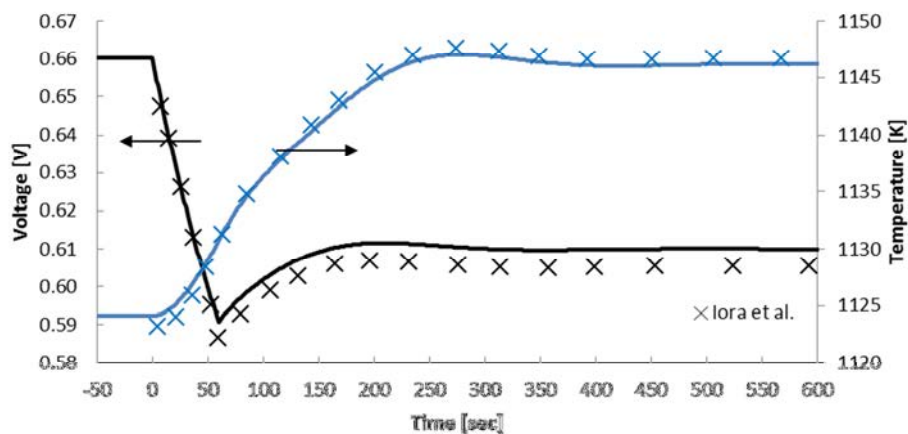
Figure 3-6 Dynamic SOFC fuel channel outlet temperature and operating cell voltage for comparison to Iora et al. [14] results

3.2   SOFC Operating Characteristics

As the SOFC stack plays the largest role in the SOFC system dynamics due to its dynamic response and power producing function, its operation must be examined and

understood. Gas species composition, reaction rate and temperature gradients greatly influence the electronic performance of the system. The following section analyzes the steady state and dynamic performance of the SOFC. SOFC parameters and boundary conditions for this section are as presented in Table 3-1 and Table 3-2.

3.2.1 Steady State Operation

As current density changes, the SOFC will operate differently due to changing temperatures, composition and flow rates. Documenting these changes with current density is the fundamental method of characterizing SOFC operation. Table 3-3 lists the variable outputs of operating voltage, power density, average PEN temperature and gas channel outlet temperatures. As shown in the table, power density increases with increasing current density, as do the various cell temperatures. Operating at higher current densities is not suggested since high thermal gradients and temperatures can permanently damage the cell. Outlet gas temperatures increase with current density, which is useful for system integration: when higher power levels are required and flow rates increased, more recuperated thermal energy is required to heat the system process flows.

Table 3-3 Select SOFC operating output data at varying current densities

Current Density [A/cm^2]	Voltage [V]	Power Dens. [W/cm^2]	Avg. PEN Temp. [K]	Outlet Fuel Temp. [K]	Outlet Air Temp. [K]
0.2	0.7793	0.1559	1008.8	1079.2	1076.2
0.3	0.7288	0.2186	1016.4	1095.5	1089.2
0.4	0.6892	0.2757	1023.7	1109.3	1099.3
0.5	0.6564	0.3282	1030.7	1121.5	1107.6
0.6	0.6284	0.3770	1037.2	1132.3	1114.7
0.7	0.6037	0.4226	1043.6	1142.1	1120.9

The composition of the fuel channel gas has an impact on the electrochemical performance due to the activation and concentration overpotentials and their dependence on composition (see Equations (2.3) and (2.12)). Figure 3-9 details the composition

profile of the fuel channel at a current density of 0.5 [A/cm^2]. Hydrogen is being produced by the conversion of methane and steam in the first third of the cell due to the apparent dominance of the steam reforming reaction here. A net consumption of hydrogen and production of steam is dominating in the later 70% of the cell. Methane is continually depleted signifying the activity of steam reforming through much of the cell.
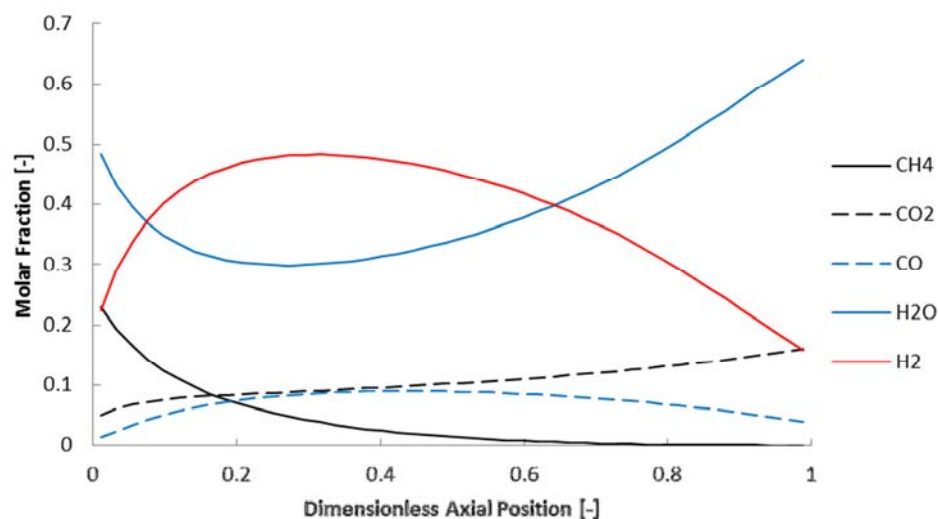
Figure 3-7 SOFC fuel channel species composition profile at 0.5 [A/cm^2]
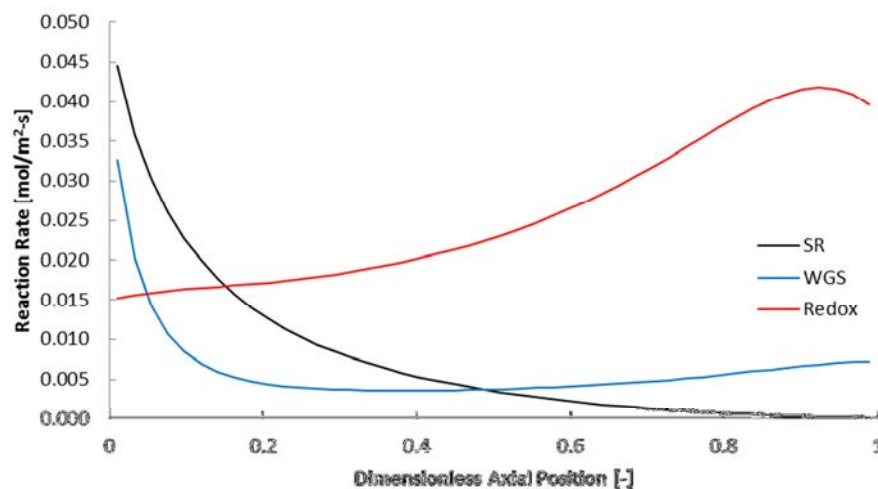
Figure 3-8 SOFC chemical reaction distribution at 0.5 [A/cm^2]

Figure 3-8 confirms the above analysis with the chemical reaction distribution. Clearly, the steam reforming and water gas shift reactions are dominating the entry of the

SOFC while the redox reaction thoroughly governs the second half of the cell. Entry is predominantly SR and WGS due to the high methane species present and lower PEN temperature here, which will be discussed momentarily. Down the cell, as the species composition is changed to a hydrogen rich flow and the SR reaction slows down, the redox reaction rate can increase due to the hydrogen present and, more importantly, the higher solid temperature. Finally, at the cell exit, the SR reaction rate is marginal so the solid temperature is high providing for the maximum redox reaction rate.
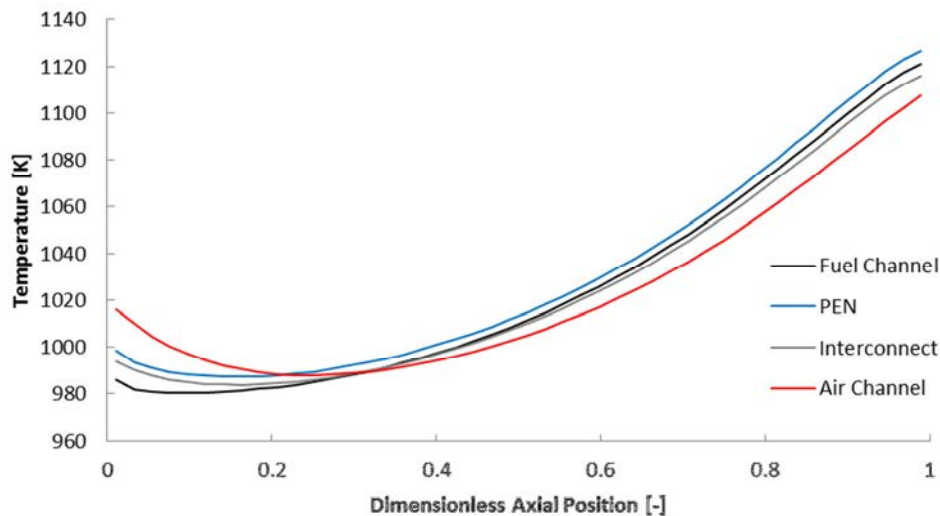
Figure 3-9 SOFC temperature profiles at 0.5 [A/cm^2]

Figure 3-9 details the temperature profiles of the two gas channels and the two solids in the SOFC at this current density. The inlet temperatures of the gases are 1023 [K] and are rapidly cooled in the first tenth and third of the cell for the fuel and air channels, respectively. In addition, the air channel gases are hotter than the PEN and fuel channel in the first third of the cell, providing heat for the endothermic steam reforming reaction that is dominating the first 20% of the cell. As the exothermic redox reaction begins to dominate, the temperatures increase thus providing for further redox. At the cell exit, the depleted air has increased to 1108 [K], a net change of about 85 [℃]. The temperature profiles are very close throughout the cell due to the high Nusselt number of 3.95, resulting in high average convective heat transfer coefficients of 373 and 136 [W/m^2-K] for the fuel and air channels, respectively.

With the previous information in hand, the electrochemical performance can be fully understood and analyzed. Figure 3-10 shows the SOFC OCV and overpotential profiles, as well as the current density profile. The uppermost solid line is the local OCV or Nernst potential with each area beneath it dictated by the noted overpotentials. As a function of gas composition and temperature, the OCV increases in the first 25% of the cell due to rapid increasing hydrogen concentration and decreasing temperature. The OCV decreases over the last 75% of the cell mainly because the temperature is increasing but also due to the increasing ratio of water to hydrogen. The activation overpotentials decrease in magnitude down the cell due to increasing temperature. The cathode concentration overpotential ("Cathode Conc.") is hardly distinguishable as a separate line from the cathode activation overpotential ("Cathode Act.") but is increasing slightly down the length of the cell with temperature. Anode concentration losses are larger than the cathode concentration losses due to the lower concentration of hydrogen. This loss increases with temperature and decreasing hydrogen concentration.

At the tail end of the cell, with the higher temperatures, the current density can be much larger than at the cell inlet while maintaining smaller overpotentials. This combination of local temperatures, gas composition and current density affect the operating voltage which is seen as the bottommost solid line. As described in Section 2.3, the equipotential assumption assumes constant operating voltage across the cell.

An understanding of the hydrodynamics within the SOFC is also important to grasp the importance of model assumptions and SOFC operation. Figure 3-11 details the pressure, velocity and density profiles for the fuel and air channels. These properties are normalized around the inlet properties. The fuel channel pressure is decreasing by less than 0.2%, which is managed by the dramatically increasing fuel channel velocity. Due to the mass transfer through the PEN structure, the velocity must increase to keep pressure decreasing while managing the increasing mass flow rate. The air channel pressure is decreasing by 3.6% due to the mass transfer out of this flow. The density of the air channel gas is greatly affected by the temperature of the flow which results in the decreasing trend in the first 25% and increasing trend in the last 75% of the cell.

Current density impacts the temperature profiles and gradients and gas composition within the stack, which affects the rest of the system components. With the same fuel utilization, air stoichiometric ratio and other parameters as listed in Table 3-2, the steady state operation at 0.2 and 0.7 [A/cm^2] is investigated below. Operating voltages at these operating points are 0.779 [V] and 0.604 [V], respectively.
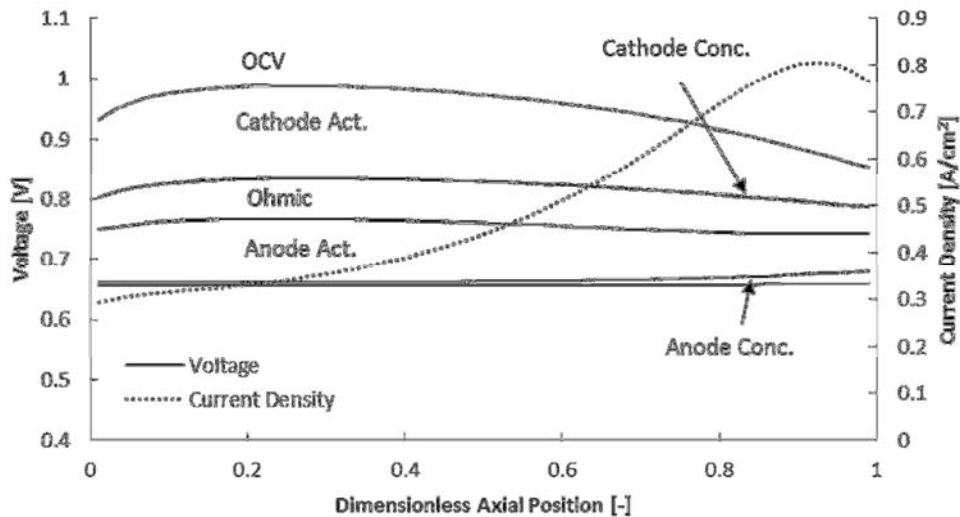
Figure 3-10 SOFC overpotential and local current density profiles at 0.5 [A/cm^2]
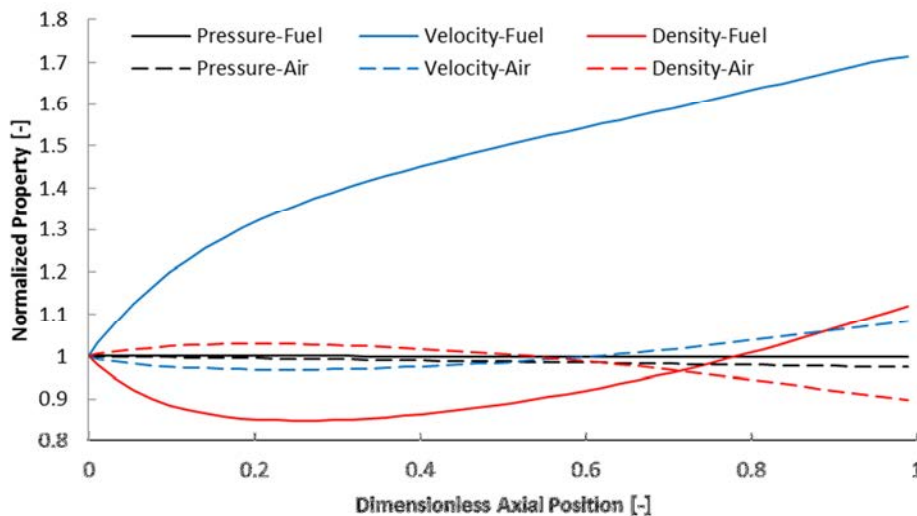
Figure 3-11 SOFC hydrodynamic gas property profiles at 0.5 [A/cm^2]

Figure 3-12 shows the temperature profiles for the fuel and air channels and PEN solid. Due to the decreased amount of redox reaction activity in the cell at 0.2 [A/cm^2], the temperatures are lower than the 0.7 [A/cm^2] case. In fact, the average PEN

temperatures are 1009 [K] and 1044[K] for the 0.2 and 0.7 [A/cm^2] cases, respectively. In addition, due to the decreased flow rates, the velocities in the lower current density case are lower than the 0.7 [A/cm^2] case, resulting in temperature profiles that are very close together. The increased residence time and higher operating cell voltage enable further heat transfer and the generally lower temperature gradients through the cell, both between layers and axially in the same layer. The overall difference between temperature profiles in the two cases also signifies that the SR, WGS and redox reactions are not occurring at equal ratios at the two operating points.
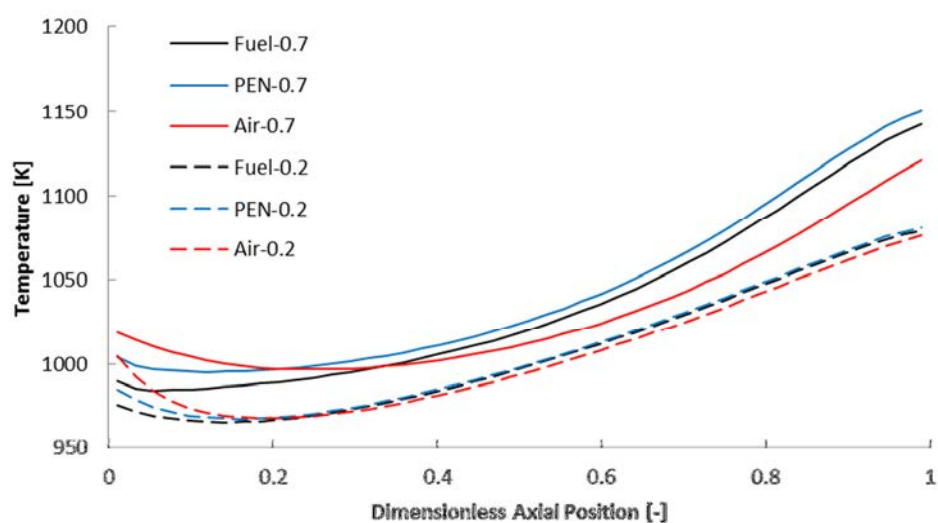
Figure 3-12 SOFC temperature profiles at 0.2 and 0.7 [A/cm^2]
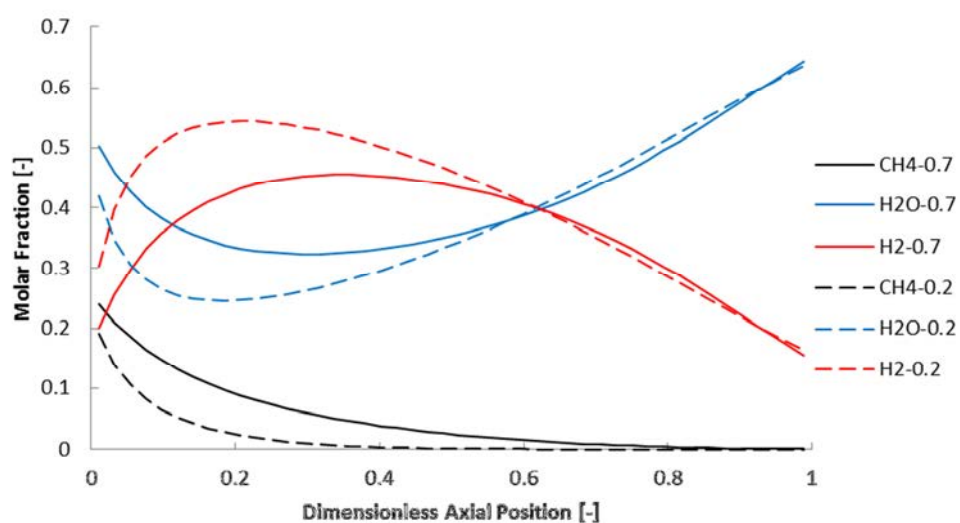
Figure 3-13 SOFC anode gas composition profiles at 0.2 and 0.7 [A/cm^2]

Figure 3-13 details the methane, steam and hydrogen composition profiles at the two operating points. Interestingly, with the same inlet composition, the outlet composition is also about the same. This bodes well for the system where minimal dynamics in outlet composition will have only a small impact on other components, perhaps improving dynamic performance of the system as a whole and allowing for better design of components like heat exchangers and tail gas combustor. The reaction rates are not occurring proportionally at the two operating points with hydrogen being produced and consumed at different rates, especially in the first 50% of the cell.

3.2.2 Dynamic Operation

The main dynamic component of the SOFC system is the ceramic stack and it has the largest impact on the system dynamic response due to its relatively large thermal mass. Thus, stack dynamics are analyzed in this section in terms of gas outlet temperature and power output. Figure 3-14 details the average PEN temperature as a function of time according to various current density steps. Cases without parentheses maintain constant fuel utilization and air stoichiometric ratio throughout the dynamic process (henceforth referred to as "strategy A"), which assumes instantaneous reaction of flow rates. Cases with parentheses indicate flow rates that are kept constant and the fuel utilization and stoichiometric ratio are allowed to vary (henceforth referred to as "strategy B"). All cases initiate at steady state with a current density of 0.5 [A/cm^2].

It is evident that the dynamics of the cell are much faster at higher current densities, or lower efficiencies. Quantitatively, the ±1% settling time[2] of average PEN temperature (henceforth referred to as thermal settling time) for the 0.7 [A/cm^2] case is 299 [s], compared to 724 [s] for the 0.3 [A/cm^2] case. That is, a 142% difference in settling time between these cases is observed and is particularly relevant when considering deploying an SOFC system to meet a building electric load. The thermal settling time of the 0.4 [A/cm^2] case with strategy A is 543 [s] compared to 391 [s] with

---

[2] ±1% settling time is defined as the maximum time value where the results cross the ±1% bounds: Initial-0.99*(Initial-Final) and Initial-1.01*(Initial-Final); where Initial is the initial steady state value and Final is the final steady state value

strategy B. This reduction in settling time suggests that faster thermal dynamic response comes at the expense of lower fuel utilization and, therefore, lower efficiency. The final fuel utilization and stoichiometric ratio are 0.60 and 10.63, respectively. However, the difference in time is less pronounced for the 0.6 [A/cm^2] case where the thermal settling time for strategy A is 360 [s] compared to 391 [s] for strategy B. In this case, settling time is actually increased by maintaining constant flow rates. Final fuel utilization and stoichiometric ratio are 0.90 and 7.1, respectively. Therefore, as seen from these simulations, the direction and magnitude of current density change has a large impact on the stack dynamics.

Figure 3-14 Dynamic average PEN temperature at various current density steps with initial conditions of steady state at 0.5 [A/cm^2]

The difference in step-up and step-down dynamics is due to the changing fuel and air flow rates which result in changing heat transfer rates between the PEN solid and gas streams. This is evidenced by the nearly identical thermal response of the step-up and step-down cases with constant fuel and air flow rates. Consider the equation for heat transfer rate: $\dot{Q} = \dot{m} c_p \Delta T$. As flow rate, $\dot{m}$, increases, the rate of heat transfer also increases, resulting in faster exchange of thermal energy. In contrast, a decreasing flow rate results in slower exchange of thermal energy. As the heat transfer rate is in units of [J/s], integrating a larger rate over time will more quickly settle to the steady state conditions as compared to a lower heat transfer rate. It is this effect of mass flow rate that results in the differing thermal responses of the step-up and step-down cases.

Figure 3-15 shows the dynamic response of the electric power output of the SOFC stack with the same load steps as the previous analysis. Here, the dynamic response of electric power production closely follows the trend of the current steps under which it was produced. There is an instantaneous change in power density showing the

instantaneous change in voltage according to the direct inclusion of current density in the electrochemical overpotentials. For the 0.7 [A/cm^2] case, the ±1% settling time of power density (henceforth referred to as power settling time) is 201 [s] while for the 0.3 [A/cm^2] case, the ±1% settling time is 243 [s]. This change in settling time and the magnitude of settling time are much smaller than the outlet temperatures. This settling in power output is impressive and means that, relatively consistently, within about 4 or 5 minutes, the SOFC can change power output level to meet the building load.

The power settling time of the 0.4 [A/cm^2] case with strategy A is 185 [s] compared to 305 [s] with strategy B. The power settling time of the 0.6 [A/cm^2] case with strategy A is 226 [s] compared to 347 [s] with strategy B. Interestingly, the lower current density case has a slightly faster response than the higher current density case, and constant flow rates again increase the stack settling time. Voltage settling time is consistently longer than power settling time across the cases due to the definition of the settling time metric. Although power output is expected to settling in the same time as voltage, power and voltage change in different proportions during the actual step in current density. After this step, current density is constant allowing for proportional response between power and voltage. It is also the definition of this metric that allows for different settling times for thermal and electrical responses. This definition of settling time was adopted as it includes the instantaneous response of the system to the load step.

The effect of initial conditions, hence initial stack efficiency, on dynamics is investigated. The initial current density for the cases below is 0.3 [A/cm^2] with the same fuel utilization, stoichiometric ratio and other inlet conditions as listed in Table 3-2. Figure 3-16 details the effects of current density steps to 0.2 and 0.24 [A/cm^2] with strategy B ("(2)") and strategy A (no parentheses) on average PEN temperature. With a 20% reduction step in current density to 0.24 [A/cm^2], the thermal settling time is 925 [s] and 631 [s] for strategies A and B, respectively. This compares to the 543 [s] and 391 [s] response for the 0.5 to 0.4 [A/cm^2] current step, which was also a 20% reduction. Initial operating conditions affect the dynamics as this is about a 60% increase in settling time at this higher efficiency operating point. Although not directly comparable to the 0.5 [A/cm^2] cases, the 0.3 to 0.2 [A/cm^2] step results in a thermal settling time of 1106 [s]

and 587 [s] for strategies A and B, respectively. Again, it is apparent that maintaining constant flow rates for a step down in current density results in faster thermal dynamics.
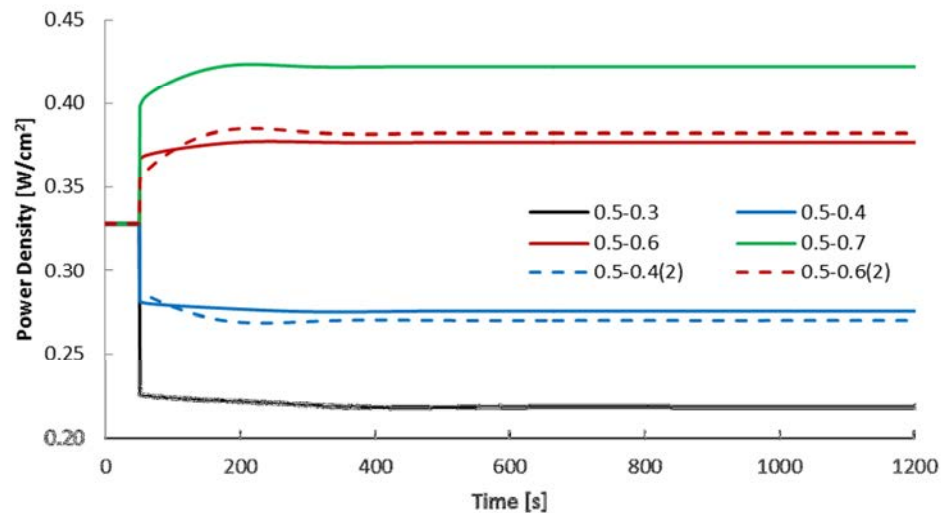
Figure 3-15 Dynamic power density at various current density steps with initial conditions of steady state at 0.5 [A/cm^2]
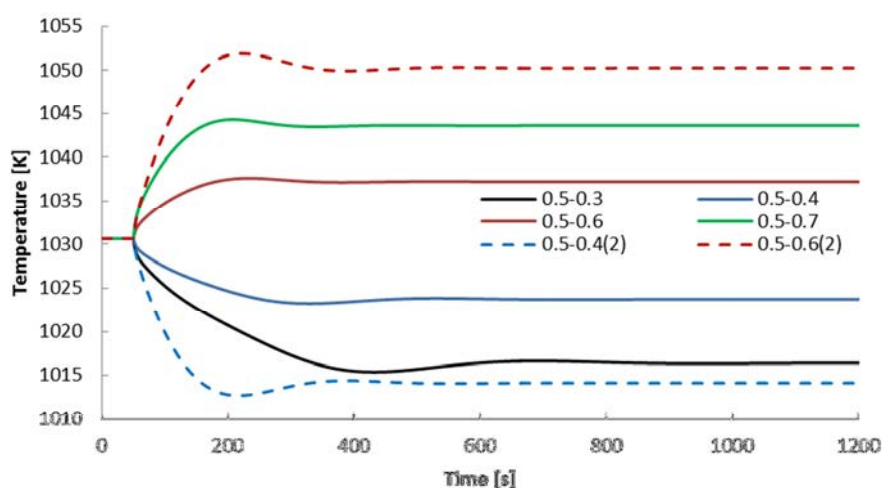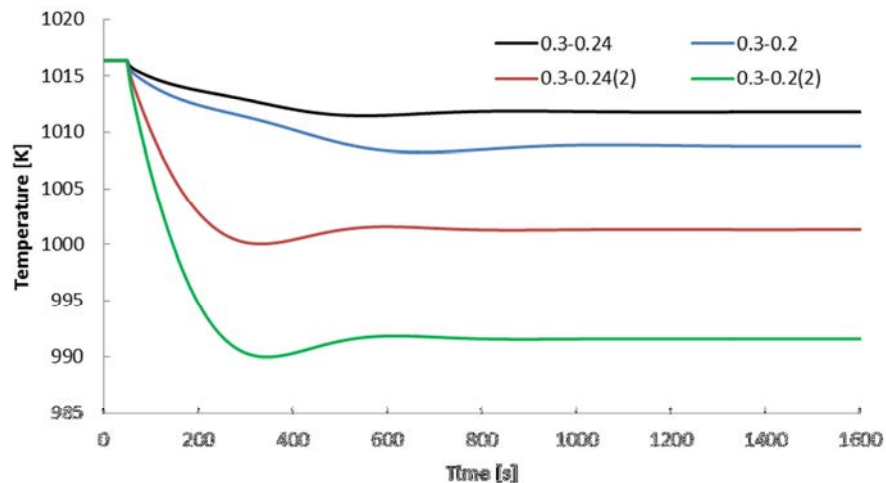

Figure 3-16 Dynamic average PEN temperature at various current density steps with initial conditions of steady state at 0.3 [A/cm^2]

More relevant to the contribution of electrical power to the building load is the dynamic density presented in Figure 3-17. Here, it is shown that a current density step to 0.24 [A/cm^2] results in a power settling time of 305 [s] and 393 [s] for strategies A and B, respectively. This compares to the 185 [s] and 305 [s] response for the 0.5 to 0.4 [A/cm^2] current step. Again, the higher efficiency operation negatively affects dynamic performance, but even so, the power output settles under 7 minutes, which is more than

suitable for a building application. Finally, the 0.3 to 0.2 [A/cm^2] step results in a power settling time of 339 [s] and 358 [s] for strategies A and B, respectively. This is the largest percent change in current density observed and yet the stack still settles within 6 minutes.
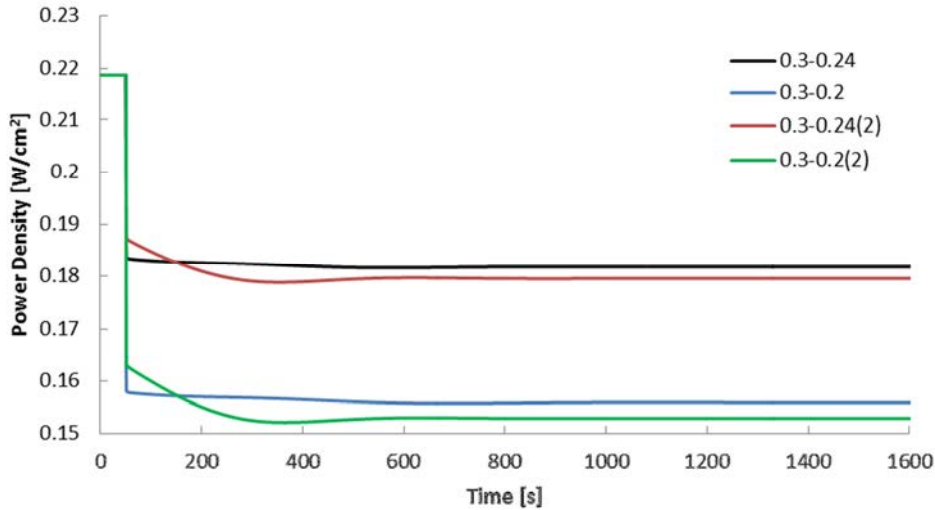
Figure 3-17 Dynamic power density at various current density steps with initial conditions of steady state at 0.3 [A/cm^2]

The oscillations in the response are due to a complex "back-and-forth" between current density and temperature distributions. Figure 3-18 helps to illustrate the effects and will assist in the explanation. After the current load and inlet flow rates are instantaneously changed, the states are not in steady state equilibrium and the energy and mass balances force the states towards equilibrium. For a current load decrease, this process results in a cooling effect on the PEN structure as there is less heat being released from the redox reaction even though there is also less electrical power produced (see Equation (2.31)). This cooling results in decreased operating voltage which reduces the electrical power output. As the cooling progresses at different rates across the cell, the current density and power output also change, but the average current density must stay constant resulting in a current density profile shift to maintain the constant current and a uniform cell voltage. As the current density profile shifts, the cooling rate also changes: essentially, the operating voltage, and current density and temperature profiles are coupled non-linearly. Eventually, the current density and temperature profiles shift to the point where they are past the equilibrium state and rebound due to the mass and energy

balances. The mass and heat capacitance of the gas streams and solids act as a natural dampening and slowly diminish these oscillations.
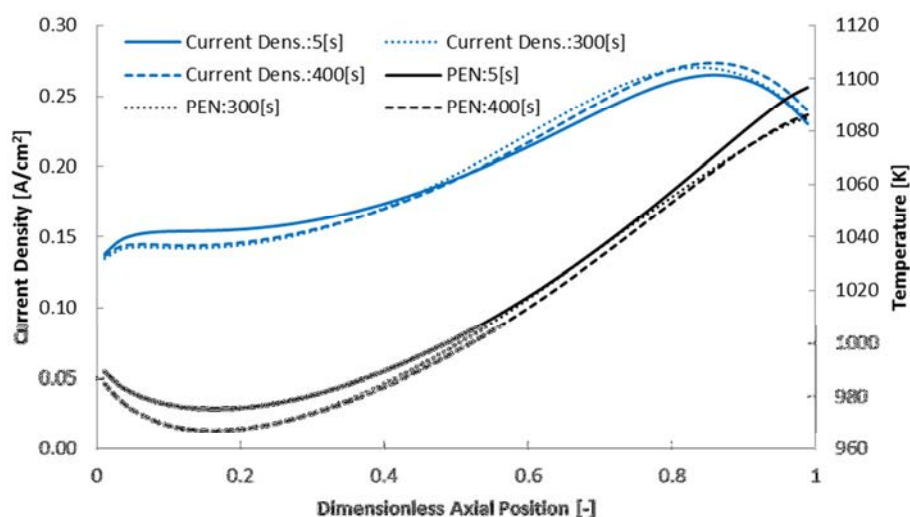
Figure 3-18 Current density and PEN temperature profiles at select times

3.2.3 Dynamic Operation Summary

The thermal, electrical and voltage settling times of the studies presented in Figure 3-14 to Figure 3-18 are presented in

Table 3-4. In brief, the following conclusions on SOFC stack dynamics can be made:

- Maintaining constant flow rates for current load reductions reduces thermal settling time but lengthens electrical settling time.
- Maintaining constant flow rates for current load increases lengthens both thermal and electrical settling times.
- The lower electrical efficiency the stack operates at either initially or finally, the faster the thermal and electrical responses.
- Magnitude and direction of load change does not characterize response times, while initial and final efficiencies do.
- There are inherent minor oscillations in the stack dynamic response.
- With electrical settling times less than 7 minutes, the SOFC stack appears to have fast enough transient response for building applications.

Table 3-4 Dynamic stand-alone SOFC settling time results

Initial Current Density [A/cm^2]	Final Current Density [A/cm^2]	Strategy	Percent Change	±1% Thermal Settling Time [s]	±1% Electrical Settling Time [s]	
					Power	Voltage
0.5	0.7	A	+40%	299	201	230
0.5	0.6	A	+20%	360	226	264
0.5	0.6	B	+20%	391	347	513
0.5	0.4	A	-20%	543	185	389
0.5	0.4	B	-20%	391	305	435
0.5	0.3	A	-40%	724	243	515
0.3	0.24	A	-20%	925	305	654
0.3	0.24	B	-20%	631	393	687
0.3	0.2	A	-33.3%	1106	339	769
0.3	0.2	B	-33.3%	587	358	669

CHAPTER 4

SOFC SYSTEM DESIGN AND COMPONENT MODELING

Since a single cell produces less than 1 [V], many cells must be arranged in electrical-series to boost the voltage to a useful value, this arrangement is called the SOFC stack. The stacks can then be placed in series and/or parallel to produce the required voltage and current requirements for the application. The SOFC stacks alone cannot produce useful power without a system of support components that prepare the reactants for the stack and recuperate heat from waste streams. Optional but preferred components are the tail gas combustor (TGC) for burning the unspent fuel, mixing and splitting valves for exhaust recycle and a pre-reformer for reducing the reforming requirements of the SOFC. The collection of optional and required components are typically called the balance-of-plant (BOP).

This chapter describes the employed SOFC system design and the models of individual components that reside in the BOP. Although all physical components have thermofluidic dynamics, nearly all components in the BOP are assumed to have fast dynamics (i.e., they quickly obtain a quasi-steady state operation). The one exception is the pre-reformer in which a lumped dynamic model is formulated and included in the system modeling effort, due to its tight chemical and thermal coupling with the SOFC stack.

4.1   Overall SOFC System Design

Many possible SOFC system design configurations exist, several variations of which are being developed. These designs have different combinations of pre-reformers, gas recycle and supplementary steam feeds, heat exchanger (HX) configurations, mixing

and ejecting components, and exhaust energy recovery sub-systems. A thorough system design process is required to choose the best combination of configuration concept, operating parameters, and hardware types for the intended application.

For the pre-reformer, for example, a steam reformer, catalytic partial oxidation reformer (CPOX), or auto reformer (ATR) may be employed. The steam reformer uses steam to convert methane into hydrogen. The CPOX reformer uses air to partially oxidize some of the fuel to produce hydrogen. This method is less fuel efficient than steam reforming considering that some of the fuel is spent in the CPOX process, yields less hydrogen and dilutes the fuel stream with nitrogen from the air feed. The dilution of the fuel feed will impede performance of the SOFC where the mole fraction of hydrogen will be decreased. Benefits of the CPOX reformer are that it has fast kinetics and thermal response, and is a comparatively simpler system to realize. ATR is a combination of CPOX and steam reforming and requires both a steam and air supply. This has the benefit of combining the exothermic CPOX reaction and endothermic steam reforming reaction and can be tuned to produce no net heat. However, the fuel feed will also be diluted by nitrogen from the air supply. Choosing the best reformer depends much on the application. CPOX reformers are compact and cheap, whereas steam reformers are more expensive, larger and may require additional expensive equipment (boiler, feedwater pump, etc.). For a small, portable SOFC system, CPOX may be preferred for its size, weight and simpler integration. Steam reformers are better suited for larger scale systems where size limitations are less of an issue for the sake of efficiency.

Braun et al. [7] analyzes several designs that include anode gas recycle, pure hydrogen fed SOFCs, external and indirect and direct internal reforming, steam ejection and hot water storage tanks for exhaust heat recovery. Braun [6] also found anode gas recycle (AGR) to reduce the magnitude of internal thermal gradients within the SOFC stack due to more uniform current density, and improve the lifetime of the system due to reduced risk of carbon coking on SOFC electrodes with the presence of carbon dioxide in the fuel feed stream. As previously mentioned, a separate steam feed line could be included instead of anode gas recycle to provide the steam required for steam reforming. In terms of reforming, Meusinger et al. [20] surmised that direct internal reforming

results in faster SOFC dynamic power response versus indirect internal reforming. However, 100% direct internal reforming results in large thermal gradients due to the large amount of internal reforming occurring at the cell inlet and subsequent large amount of redox occurring at the cell outlet.

For this system design, it was chosen to employ anode gas recycle which required the addition of mixing and splitting valves in order to divert some of the fuel channel exhaust gases to the fuel feed stream. Although direct internal reforming was part of the SOFC stack model and design, a small steam-methane pre-reformer was adopted to help reduce the thermal gradients in the stack. Although this added equipment may increase capital costs, the reduced gradients will improve the lifespan of the stack.

Additional support equipment is required for the SOFC system to function. A tail gas combustor (TGC) was added to mix the fuel and air channel exhaust gases of the SOFC and finish firing the exhausted fuel stream. This added thermal energy compounds with the heat gained in the SOFC stack and can then be recuperated in heat exchangers to preheat the fuel and air streams. Without these preheat heat exchangers, the fuel and air streams would be much too cold for the stack to operate efficiently. Additionally, feed pumps are needed to overcome the head loss in the ducting and system components. Figure 4-1 details the SOFC system. Some of the produced electrical power is used to run the reactant feed pumps while the net electrical power is exported to the building. State points are provided within the figure for reference.
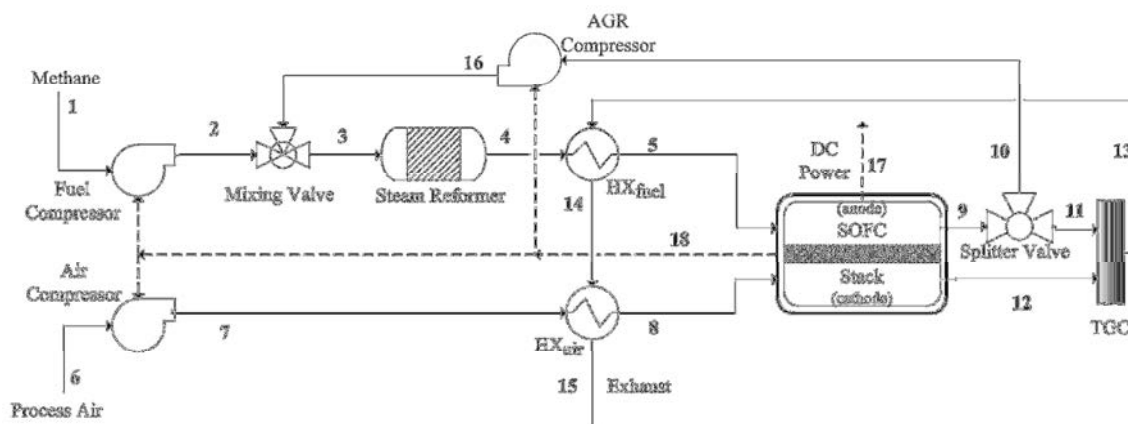
Figure 4-1 SOFC system flow diagram

4.2   SOFC System Component Models

The following section details the mathematical models used to represent the SOFC system balance-of-plant components. All system components are steady state and have adiabatic boundary conditions with the surroundings, the only exception being the dynamic steam reformer. No formulation for system component pressure drop at any operating condition has been included in the system model. All components are modeled in the Fortran 90 language and the system is constructed in TRNSYS [37]. Some components were pre-existing components available with the TRNSYS package and where applicable, are noted as such.

4.2.1   Fuel, AGR and Air Compressors

The system feed pumps use a modified pre-existing pump model in the TESS add-on package to the TRNSYS environment. This routine, known as Type 630 in TRNSYS, is an air compressor model that uses mass flow, inlet gas temperature and operating pressure ratio as inputs and calculates the electrical power required and added thermal energy with a given efficiency. The model uses an iterative algorithm to employ average gas properties between the inlet and outlet of the pump. Type 630 was modified for use as methane and exhaust gas recycle compressors by changing the embedded function for specific heat of the gas and specific gas constant. In addition, the embedded specific heat curve fit was replaced in the air compressor model with a curve fit from EES software to ensure consistency.

The model first calculates the isentropic outlet temperature, $T_{out,ideal}$, according to the polytropic compression process shown in Equation (4.1). In this equation, T_{in} is the gas inlet temperature, P_{in} is the gas inlet pressure, P_{out} is the gas outlet pressure and k is the specific heat ratio of the gas. The specific heat ratio is calculated using the average specific heat capacities, which explains the need for the iterative algorithm.

$$\frac{T_{out,ideal}}{T_{in}} = \left(\frac{P_{out}}{P_{in}} \right)^{\left(\frac{k-1}{k} \right)} \tag{4.1}$$

With a given isentropic efficiency of the compressor, η_s, the outlet temperature, T_{out}, can be calculated from the definition of isentropic compression efficiency, shown in Equation (4.2).

$$\eta_s = \frac{T_{out,ideal} - T_{in}}{T_{out} - T_{in}} \tag{4.2}$$

With the outlet temperature now known, the gas properties at the exit can be calculated, average properties updated, and the process repeated until convergence. Once the converged outlet temperature is found, the following equation is used to calculate the electrical power required to run the compressor, $\dot{W}_{comp,e}$. η_e, is the electrical efficiency of the motor driving the compressor, $\dot{m}$ is the flow rate of the gas and c_p is the average heat capacity across the temperature range.

$$\dot{W}_{comp,e} = \dot{m}c_p\left(T_{out} - T_{in}\right)/\eta_e \tag{4.3}$$

Moran and Shapiro [21] state that typical isentropic efficiencies for compressors are between 75 and 85%, therefore an isentropic efficiency of 80% was chosen and assumed constant. The electric motors driving the compressors are brushless DC motors as they provide higher electrical efficiencies than induction motors, and eliminate the need for a DC/AC converter and its associated losses. An assumed and constant electrical efficiency of 92% was chosen.

4.2.2 Heat Exchangers

The system model employs a pre-existing heat exchanger model from the TRNSYS environment. This routine, known as Type 91 in TRNSYS, simulates a sensible heat exchanger providing outlet temperatures of the hot and cold streams according to the ε-NTU method. The routine utilizes a constant heat exchanger effectiveness that is selected by the user as specifying UA values are outside the scope of this research. For the sake of simplicity in dynamic simulation, it is further assumed that the heat exchanger achieves a constant effectiveness at both the design point and throughout the entire

operating envelope with negligible dynamics. The ε-NTU method is simplified with the constant effectiveness assumption and is defined by Equation (4.4):

$$\dot{q}_{actual} = \varepsilon \cdot \dot{q}_{max} \tag{4.4}$$

where $\dot{q}_{actual}$ is the actual rate of heat transfer from the source to the load fluid, $\dot{q}_{max}$ is the maximum possible rate of heat transfer, and ε is the heat exchanger effectiveness. The constant effectiveness assumption eliminates the need for calculating effectiveness according to heat exchanger geometry and flow conditions. The maximum possible rate of heat transfer is defined by Equation (4.5):

$$\dot{q}_{max} = \dot{C}_{min}\left(T_{hot,in} - T_{cold,in}\right) \tag{4.5}$$

where $T_{hot,in}$ is the temperature of the source fluid at the HX inlet, $T_{cold,in}$ is the temperature of the cold fluid at the HX inlet, and $\dot{C}_{min}$ is the minimum capacity rate of the two fluids. The capacity rate is defined as:

$$\dot{C} = \dot{m} \cdot c_p \tag{4.6}$$

where $\dot{m}$ is the mass flow rate of the fluid, and c_p is the specific heat capacity of the fluid.

The outlet temperatures, T_{out}, are calculated using the actual rate of heat transfer and respective inlet temperatures according to the equations below:

$$T_{hot,out} = T_{hot,in} - \frac{\dot{q}_{actual}}{\dot{m}_{hot}c_{p,hot}} \tag{4.7}$$

$$T_{cold,out} = T_{cold,in} + \frac{\dot{q}_{actual}}{\dot{m}_{cold}c_{p,cold}} \tag{4.8}$$

4.2.3 Tail Gas Combustor

The tail gas combustor combines the non-recycled anode exhaust gases with the depleted air channel exhaust and any unfired fuel is combusted at an adiabatic flame

temperature. The following chemical reactions occur with the complete combustion of methane, carbon monoxide and hydrogen.

Table 4-1 TGC Reactions

Reaction
$CH_4 + 2\,O_2 \rightarrow CO_2 + H_2O$
$CO + \frac{1}{2}\,O_2 \rightarrow CO_2$
$H_2 + \frac{1}{2}\,O_2 \rightarrow H_2O$

The TGC model uses the inlet conditions and known reactions to calculate the outlet composition and species molar flow rates. The adiabatic flame temperature is then calculated according to the following equation:

$$H_{reactants} = \sum_i \dot{n}_{i,reactants} h_{i,reactants}\left(T_{reactants}\right) = H_{products} = \sum_j \dot{n}_{j,products} h_{j,products}\left(T_{products}\right)$$

$$i \in \{CH_4, CO_2, CO, H_2O, H_2, N_2, O_2\} \tag{4.9}$$

$$j \in \{CO_2, H_2O, N_2, O_2\}$$

where $H_{reactants}$ is the total enthalpy present in the reactant or inlet flow, $H_{products}$ is the total enthalpy present in the product or outlet flow, $\dot{n}_i$ is the molar flow rate of species i in the reactant or product stream, and h_i is the specific enthalpy of species i at temperature $T_{reactants}$ or $T_{products}$ according to the stream.

An iterative process, utilizing the same zbrent function as referenced in Section 2.6, finds the product temperature that satisfies the above equation. The specific enthalpy values of the present gas species are calculated via curve fits from the gas property data in EES.

4.2.4 AGR and Methane Feed Mixing Valve

The mixer combines the recycled anode exhaust gases with the inlet methane feed stream and supplies this gas mixture to the reformer. This model utilizes the same method as the tail gas combustor to calculate the adiabatic mixing temperature of the inlet

streams, but without any reactions occurring. With the absence of reactions in the control volume, a molar balance may be written to determine the outlet molar flow rate, $\dot{n}_{outlet}$:

$$\dot{n}_{outlet} = \dot{n}_{CH_4\ Feed} + \dot{n}_{AGR} \tag{4.10}$$

where $\dot{n}_{CH_4\ Feed}$ is the molar flow rate of the methane feed stream and $\dot{n}_{AGR}$ is the molar flow rate of the anode gas recycle stream.

Inlet conditions are used to calculate the outlet composition, which is then employed in the energy balance of the mixer detailed in Equation (4.11):

$$H_{in} = \dot{n}_{CH_4\ Feed} h_{CH_4\ Feed} \left(T_{CH_4\ Feed}\right) + \dot{n}_{AGR} \sum_i x_{i,AGR} h_{i,AGR} \left(T_{AGR}\right) =$$
$$H_{outlet} = \dot{n}_{outlet} \sum_i x_{i,outlet} h_{i,outlet} \left(T_{outlet}\right) \tag{4.11}$$
$$i \in \{CH_4, CO_2, CO, H_2O, H_2\}$$

where H_{in} is the total enthalpy present in the inlet flows, H_{outlet} is the total enthalpy present in the outlet flow, x_i is the molar fraction of species i in the inlet or outlet streams, and $h_i(T)$ is the specific enthalpy of species i at temperature T.

4.2.5 Splitter Valve

The splitter valve splits the anode exhaust gas flow into the anode gas recycle stream and the non-recycle stream sent to the TGC. This component is simply modeled as an adiabatic unit that outputs the recycle and non-recycle stream mass and molar flow rates according to a given splitting percentage. The inlet temperature and composition are preserved for the recycle and non-recycle streams. The equation below details the simple mass balance of the valve:

$$\dot{m}_{in} = \dot{m}_{AGR} + \dot{m}_{F,TGC}$$
$$where: \quad \dot{m}_{AGR} = \alpha \dot{m}_{in} \tag{4.12}$$
$$\dot{m}_{F,TGC} = (1-\alpha) \dot{m}_{in}$$

where $\dot{m}_{in}$ is the mass flow rate into the valve or the total exhaust mass flow rate from the stack fuel channels, $\dot{m}_{AGR}$ is the mass flow rate for anode gas recycle, $\dot{m}_{F,TGC}$ is the mass flow rate of the fuel channel exhaust sent to the tail gas combustor, and α is the ratio of AGR to total stack fuel channel exhaust flow rate.

4.2.6   Steam Pre-Reformer

The reformer is assumed to be a stainless steel cylinder casing filled with steam reforming catalyst. The steam pre-reformer model is based off a model described in Murshed et al. [22]. This model is thermally lumped, adiabatic at its boundaries with the surroundings, and is dynamic in temperature only. It is assumed that the reformate exits the reformer at the reformer solid temperature. Although this model is of a much lesser fidelity than the SOFC, it is important to capture some of the dynamics of the reformer as it has a high thermal mass. Not only do the thermal dynamics of the reformer affect the inlet temperature to the SOFC, but they affect the composition of the inlet gas as well. Included in the model are chemical reactions for steam reforming (SR) and water-gas shift (WGS). Chemical reaction equations for SR and WGS are provided in Table 2-2. Figure 4-2 provides a diagram of the reformer with its control volume for reference.
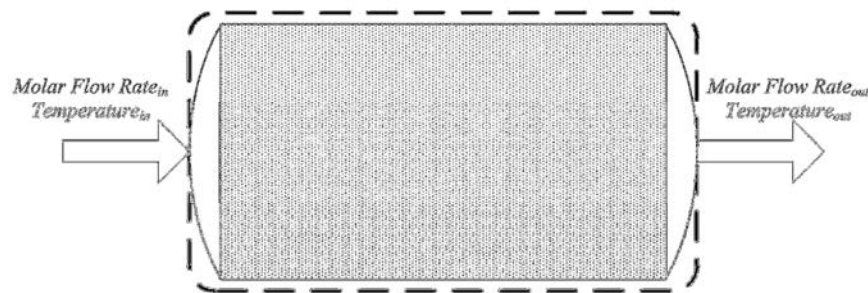
Figure 4-2 Reformer control volume and flows

The model calculates the present reactions in series. In other words, the SR reaction rate is calculated with the inlet conditions and the inlet gas is then reacted according to the SR reaction rate to find the intermediate ("mid") composition. The WGS equilibrium equation is then solved for this "mid" composition and the outlet conditions calculated. The reaction rate equation for SR in [mol/s] as developed by Achenbach and Riensche [2] is reproduced below:

$$\dot{r}_{SR} = k_0 p_{CH_4} \exp\left(-\frac{E_a}{RT_R}\right) A_{rxn} \tag{4.13}$$

where p_{CH_4} is the partial pressure of methane at the reformer inlet, T_R is the reformer solid temperature, A_{rxn} is the given catalytically active surface area. A pre-exponential constant of $k_0 = 0.04274$ [mol s^{-1} m^{-2} Pa^{-1}] and an activation energy of $E_a = 82$ [kJ mol^{-1}] are used.

The intermediate composition is calculated using the above reaction rate according the following equations:

$$\dot{n}_{CH_4}^{mid} = \dot{n}_{CH_4}^{in} - \dot{r}_{SR} \tag{4.14}$$

$$\dot{n}_{H_2O}^{mid} = \dot{n}_{H_2O}^{in} - \dot{r}_{SR} \tag{4.15}$$

$$\dot{n}_{H_2}^{mid} = \dot{n}_{H_2}^{in} + 3\dot{r}_{SR} \tag{4.16}$$

$$\dot{n}_{CO}^{mid} = \dot{n}_{CO}^{in} + \dot{r}_{SR} \tag{4.17}$$

$$\dot{n}_{CO_2}^{mid} = \dot{n}_{CO_2}^{in} \tag{4.18}$$

where $\dot{n}_i^{mid}$ is the molar flow rate of species i at the intermediate stage and $\dot{n}_i^{in}$ is the molar flow rate of species i at the reformer inlet. Notice that carbon dioxide is not affected by the SR reaction.

The WGS equilibrium constant, $K_{eq,WGS}$, is then applied to the intermediate composition according to the following relationship:

$$K_{eq,WGS} = \frac{\left(\dot{n}_{CO_2}^{mid} + \varepsilon_{WGS}\right)\left(\dot{n}_{H_2}^{mid} + \varepsilon_{WGS}\right)}{\left(\dot{n}_{CO}^{mid} - \varepsilon_{WGS}\right)\left(\dot{n}_{H_2O}^{mid} - \varepsilon_{WGS}\right)} \tag{4.19}$$

where ε_{WGS} is the extent of the WGS reaction in [mol/s] and $K_{eq,WGS}$ is the same curve fit equation of Moran and Shapiro data [21] as in the SOFC model.

The outlet composition can then be calculated using the following equations:

$$\dot{n}_{CH_4}^{out} = \dot{n}_{CH_4}^{mid} \tag{4.20}$$

$$\dot{n}_{H_2O}^{out} = \dot{n}_{H_2O}^{mid} - \varepsilon_{WGS} \tag{4.21}$$

$$\dot{n}_{H_2}^{out} = \dot{n}_{H_2}^{mid} + \varepsilon_{WGS} \tag{4.22}$$

$$\dot{n}_{CO}^{out} = \dot{n}_{CO}^{mid} - \varepsilon_{WGS} \tag{4.23}$$

$$\dot{n}_{CO_2}^{out} = \dot{n}_{CO_2}^{mid} + \varepsilon_{WGS} \tag{4.24}$$

where $\dot{n}_i^{out}$ is the molar flow rate of species i at the reformer outlet.

Finally, a dynamic energy balance may be established for calculation of reformer temperature using the control volume definition in Figure 4-2. The following equation details the energy balance:

$$\left(M_{R,case} c_{p,R,case} + M_{R,cat} c_{p,R,cat} \right) \frac{dT_R}{dt} = \sum_i \dot{n}_i^{in} h_i^{in} \left(T_{in} \right) - \sum_i \dot{n}_i^{out} h_i^{out} \left(T_R \right)$$
$$i \in \left\{ CH_4, CO_2, CO, H_2O, H_2 \right\} \tag{4.25}$$

where $M_{R,case}$ is the mass of the stainless steel reformer casing, $c_{p,R,case}$ is the specific heat of the reformer casing, $M_{R,cat}$ is the mass of the reformer catalyst, $c_{p,R,cat}$ is the specific heat of the catalyst, T_{in} is the inlet gas temperature and $h_i(T)$ is the specific enthalpy of species i at temperature T. This dynamic equation is solved using the differential algebraic solver, LIMEX (see Section 2.6). Catalyst data is taken from the manufacturer specification sheet for Matrostech NIAP-03-01 [36] and additional data is taken from the literature [10].

Figure 4-3 shows the reformer dynamics of outlet gas temperature and composition with representative operating conditions of an inlet mixture of 25% CH_4, 18.7% CO_2, 6.3% CO, 38.2 % H_2O and 11.8% H_2 at 895 [K] and 36.9 [kg/hr] with an initial reformer temperature of 850 [K]. Reformer sizing parameters for this case are shown in Table 5-1. The system shows a classical 2nd order response with a ±1% thermal settling time of 306 [s]. Due to the adiabatic nature of the reformer, the outlet temperature of the gas mixture is nearly 100 [°C] cooler than the inlet temperature with the heat sink of steam reforming dominating the chemical reaction activity in the reformer. The steam reformer begins the simulation converting 21% of the methane but reaches a steady state

conversion percentage of 11%. Compared to the dynamics of the SOFC stack, the reformer has a thermal response in similar duration and is important to visualizing and understanding the complete SOFC system dynamics.
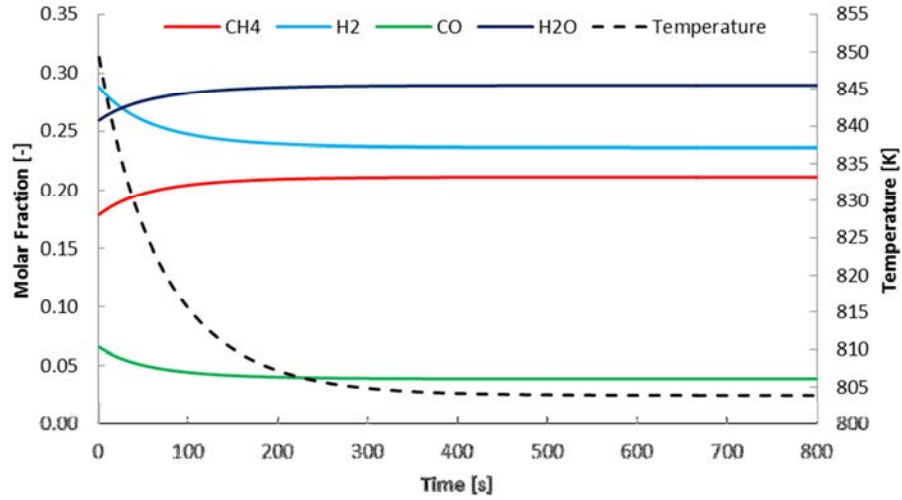
Figure 4-3 Reformer dynamics with representative operating conditions

CHAPTER 5

SOFC SYSTEM OPERATING CHARACTERISTICS

In this chapter the dynamic operating characteristics of a fully integrated SOFC system are analyzed. First, the system design is quantitatively discussed. This is followed by a discussion and analysis of the system operation at steady state operating conditions. Lastly, the dynamic response and component interaction within the system are analyzed in the context of building application requirements. The SOFC system flow diagram with state points is reproduced in Figure 5-1 for reference.
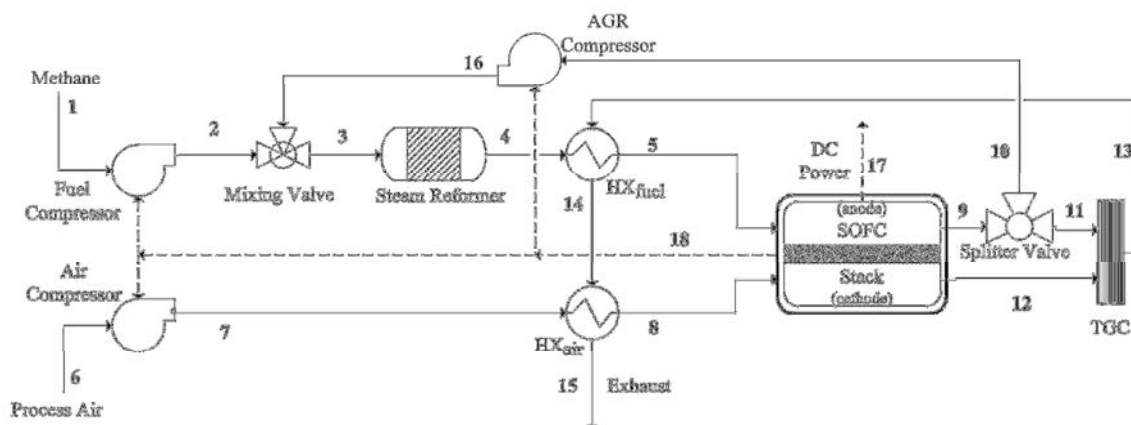
Figure 5-1 SOFC system flow diagram

5.1 System Design Parameters

As it is preferred that the system will operate at steady state at certain times, the steady state system performance is first analyzed and explored. Steady state operation was used to size the reformer and specify the needed heat exchanger effectivenesses. The steam reformer was sized to react about 10% of the inlet methane at an SOFC stack current density of 0.5 [A/cm^2]. The inlet flow rates of methane and air were adjusted until

a suitable SOFC operating voltage was enabled. In addition, heat exchanger effectiveness values were varied within a feasible range until appropriate SOFC inlet temperatures were achieved. As the rest of the components are relatively simple, no sizing or other specifications were required.

It is noted here that the SOFC system under study is not optimized in terms of performance, cost, operating parameter selection, or configuration, but is considered a representative design which will meet the research objectives of elucidating system dynamics and component interactions associated with stationary distributed power applications. Table 5-1 details the system parameters that were chosen. The reformer dimensions are used to calculate the reformer heat capacitance. The number of cells in the stack is chosen to appropriately size the system for a commercial building application, ~45 [kW$_e$].

Table 5-1 SOFC system parameters and operating conditions

Parameter	Value	Units	Parameter	Value	Units
Fuel Utilization:	69%		Stoichiometric Air Ratio:	7.0	
Inlet Fuel Temperature:	26.85	C	Inlet Air Temperature:	26.85	C
Reformer reaction area:	2	m^2	Reformer volume:	0.0111	m^3
Reformer length:	0.25	m	Reformer case thickness:	1.5	mm
Fuel HX effectiveness:	0.6		Air HX effectiveness:	0.8	
Number of cells:	384		Operating SOFC Pressure:	1.3	Atm
AGR Percentage:	50%				

5.2   Steady State SOFC System Operation

Table 5-2 details the temperature, flow rate, composition and pressure at each state point for an operating current density of 0.5 [A/cm^2] and system parameters according to Table 5-1. Methane enters the fuel compressor at 7 [kg/hr] and air enters the air compressor at 687.5 [kg/hr]. The compressor outlet fuel flow is preheated considerably by mixing with the AGR to 622 [C] and is then supplied to the pre-reformer. Since the outlet flow of the reformer is equal to the temperature of the reformer solid, the

reformer temperature is that of state point (4). The flow is cooled to 531 [C] due to the endothermic steam reforming reaction occurring in the reformer. At these conditions, the reformer is reacting 10.9% of the methane flow. The fuel flow is then preheated by the fuel heat exchanger to 786 [C] and fed to the SOFC anode. After being compressed, the air flow is preheated by the air heat exchanger to 757 [C] and fed to the SOFC cathode. These SOFC inlet and operating conditions result in an average PEN temperature of 760.3 [C], with the minimum and maximum being 712 [C] and 878 [C]. Under these conditions, each cell in the stack produces 0.685 [V] and 0.342 [W/cm^2]. The air and fuel flows are exhausted at 857 [C] and 872 [C], respectively. Note that the mass flow rate of the fuel channel exhaust has increased considerably compared to the inlet flow. This is due to the mass transfer of oxygen ions to the fuel flow across the PEN structure. At (11), the flow is still 12% hydrogen which is then mixed and combusted with the air channel exhaust to release the stored chemical energy. This TGC exhaust is then fed to the heat exchangers and then exhausted at 379 [C]. The net DC power is 46.1 [kW] with 12.4% of the gross electric power used to energize the compressors.

Table 5-2 SOFC system state points at 0.5 [A/cm^2]

State Point	Temp. [C]	Flow Rate [kg/hr]	CH_4	CO_2	CO	H_2O	H_2	N_2	O_2	Pressure [Bar]	Elec. Power [kW$_e$]
1	27	7.00	1.00	0.00	0.00	0.00	0.00	0.00	0.00	1.000	-
2	51	7.00	1.00	0.00	0.00	0.00	0.00	0.00	0.00	1.317	-
3	622	36.92	0.25	0.19	0.06	0.38	0.12	0.00	0.00	1.317	-
4	531	36.92	0.21	0.22	0.04	0.29	0.24	0.00	0.00	1.317	-
5	786	36.92	0.21	0.22	0.04	0.29	0.24	0.00	0.00	1.317	-
6	27	687.50	0.00	0.00	0.00	0.00	0.00	0.79	0.21	1.000	-
7	58	687.50	0.00	0.00	0.00	0.00	0.00	0.79	0.21	1.317	-
8	757	687.50	0.00	0.00	0.00	0.00	0.00	0.79	0.21	1.317	-
9	872	59.85	0.00	0.25	0.08	0.51	0.16	0.00	0.00	1.316	-
10	872	29.92	0.00	0.25	0.08	0.51	0.16	0.00	0.00	1.316	-
11	872	29.92	0.00	0.25	0.08	0.51	0.16	0.00	0.00	1.316	-
12	857	664.58	0.00	0.00	0.00	0.00	0.00	0.81	0.19	1.301	-
13	957	694.50	0.00	0.02	0.00	0.04	0.00	0.78	0.17	1.301	-
14	932	694.50	0.00	0.02	0.00	0.04	0.00	0.78	0.17	1.301	-
15	379	694.50	0.00	0.02	0.00	0.04	0.00	0.78	0.17	1.301	-
16	872	29.92	0.00	0.25	0.08	0.51	0.16	0.00	0.00	1.317	-
17	-	-	-	-	-	-	-	-	-	-	46.1
18	-	-	-	-	-	-	-	-	-	-	6.5

With such a high exhaust temperature and flow rate, substantial heat can be recovered and used for domestic hot water or HVAC components. By adding a heat recovery loop and exhausting the gases at 120 [C], a maximum of 49.4 [kW] of thermal energy can be recovered. Without this recovery, the system efficiency is 47.4%. Adding heat recovery with a nominal 70% effectiveness enables a combined heat and power (CHP) system efficiency of 83.0% with a system thermal-to-electric ratio (TER) of 0.75. Considering that the U.S. national average centralized power plant thermal efficiency is less than 35%, this CHP operation results in far superior fuel conversion efficiency at substantially smaller power scales.

In order to compare system performance at a different operating point, Table 5-3 presents system state point data at an SOFC current density of 0.3 [A/cm^2]. The methane and air flow rates are specified to maintain the same fuel utilization and air stoichiometric ratio as in Table 5-1. At this operating point, the reformer is converting 11.3% of the inlet methane and the system is producing a net power output of 28.8 [kW$_e$]. This 40% decrease in current load results in a 38% decrease in power output. This linearity makes the control problem of electric power output to the building much simpler. As noted in Section 3.2.1, the SOFC produces a consistent molar composition across operating conditions; this translates to the system and is apparent when comparing these system results to those of Table 5-2.

Flow temperatures are about 30-40 [℃] cooler across the system with the reformer exactly 30 [℃] cooler, and the SOFC average PEN temperature 37.3 [℃] cooler. This consistent decrease in temperature across the system means that system components, especially heat exchangers, are stressed in approximately equal proportion at this load setting. This is important for the lifespan of the components as part-load operation of the system is desired and even stresses equate to longer lifespans. The electrical efficiency of the system is 49.3% with a CHP efficiency of 82.9% and TER of 0.68. Therefore, decreasing the current load of the system with constant parameters improves the electrical efficiency, hardly affects the CHP efficiency, but slightly decreases the TER. When integrating the SOFC system into a building, it is necessary to consider the effects of load and other operating conditions on the combination of

electrical and thermal output. For example, when increasing the electrical load of the system, either a control strategy can be used to decrease the TER to maintain constant thermal output, or heat storage may be required to take advantage of the available energy.

Table 5-3 SOFC system state points at 0.3 [A/cm^2]

State Point	Temp. [C]	Flow Rate [kg/hr]	Molar Composition							Pressure [Bar]	Elec. Power [kW$_e$]
			CH$_4$	CO$_2$	CO	H$_2$O	H$_2$	N$_2$	O$_2$		
1	27	4.20	1.00	0.00	0.00	0.00	0.00	0.00	0.00	1.000	-
2	51	4.20	1.00	0.00	0.00	0.00	0.00	0.00	0.00	1.317	-
3	595	22.15	0.25	0.19	0.06	0.38	0.12	0.00	0.00	1.317	-
4	501	22.15	0.21	0.23	0.03	0.28	0.24	0.00	0.00	1.317	-
5	754	22.15	0.21	0.23	0.03	0.28	0.24	0.00	0.00	1.317	-
6	27	412.50	0.00	0.00	0.00	0.00	0.00	0.79	0.21	1.000	-
7	58	412.50	0.00	0.00	0.00	0.00	0.00	0.79	0.21	1.317	-
8	731	412.50	0.00	0.00	0.00	0.00	0.00	0.79	0.21	1.317	-
9	833	35.91	0.00	0.25	0.08	0.50	0.16	0.00	0.00	1.316	-
10	833	17.95	0.00	0.25	0.08	0.50	0.16	0.00	0.00	1.316	-
11	833	17.95	0.00	0.25	0.08	0.50	0.16	0.00	0.00	1.316	-
12	823	398.75	0.00	0.00	0.00	0.00	0.00	0.81	0.19	1.308	-
13	923	416.70	0.00	0.02	0.00	0.04	0.00	0.78	0.17	1.308	-
14	899	416.70	0.00	0.02	0.00	0.04	0.00	0.78	0.17	1.308	-
15	365	416.70	0.00	0.02	0.00	0.04	0.00	0.78	0.17	1.308	-
16	833	17.95	0.00	0.25	0.08	0.50	0.16	0.00	0.00	1.317	-
17	-	-	-	-	-	-	-	-	-	-	28.8
18	-	-	-	-	-	-	-	-	-	-	3.9

5.3   Dynamic SOFC System Operation

The dynamic system operation is investigated much the same way as the SOFC stack dynamics were investigated in Section 3.2: load changes in different magnitudes and directions, and different initial conditions are explored. Although the SOFC stack model can be run with steps in current density, the system model implemented in TRNSYS is unable to consistently obtain numeric convergence with instantaneous steps. Therefore, current ramps are performed over 50 seconds which closely simulates a current step when considering the long dynamic response of the system.

5.3.1   0.5 to 0.4 [A/cm^2] Current Ramp

Figure 5-2 details the electrical dynamics of the SOFC system for a 50 second current ramp from 0.5 to 0.4 [A/cm^2] with constant fuel utilization and air stoichiometric ratio. The ±1% settling time for the net DC power output is 999 [s] or about 17 minutes compared to 3 minutes for the stand-alone SOFC stack. This 20% reduction in current load results in an 18.5% reduction in power output with a final value of 37.6 [kW$_e$]. The dynamics of the response are slightly oscillatory in nature, but are fairly tame; results with more dramatic dynamics are discussed further in this section. The voltage response initially increases, with the overpotentials instantaneously adjusting for the decreased current density. As the current density stops changing, the voltage then slowly decreases to its steady state value due to the decreasing PEN solid temperature as discussed below.
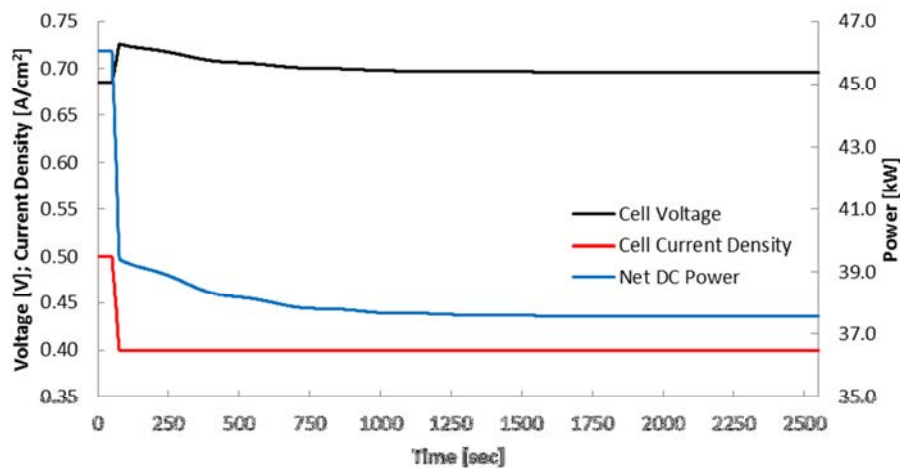

Figure 5-2 SOFC system electrical dynamics for ramp from 0.5 to 0.4 [A/cm^2]

Figure 5-3 shows the thermal response of the in-system SOFC stack for this current load change. The average PEN temperature is slowly decreasing due to the decreasing amount of redox reaction occurring in the cell. This lower conversion of chemical energy and the simultaneous increase in cell efficiency allows for the gas flows to carry heat out of the cell until the PEN solid reaches its steady state temperature. The average PEN temperature settles within 1% of its steady state value 1500 [s] after the load begins to change. Most noticeable in this figure are the more visible oscillations of the outlet gas temperatures. This occurs due to the inherent dynamics in the SOFC stack (see Section 3.2.2), especially during decreasing load changes. Recall that these dynamics

occur due to the complex coupling between temperature and current density profiles. These dynamics are much more defined than the stand-alone SOFC stack case due to the coupling of inlet and outlet stack gas temperatures from AGR and exhaust heat recuperation.
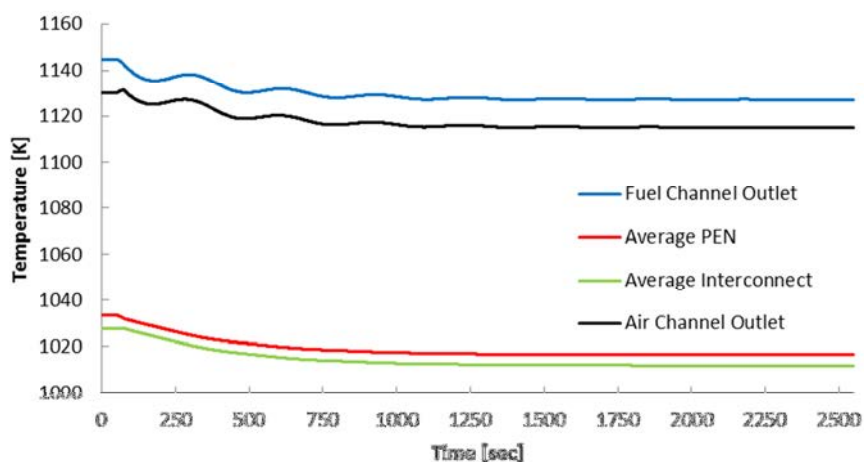

Figure 5-3 In-system SOFC stack thermal dynamics for ramp from 0.5 to 0.4 [A/cm^2]
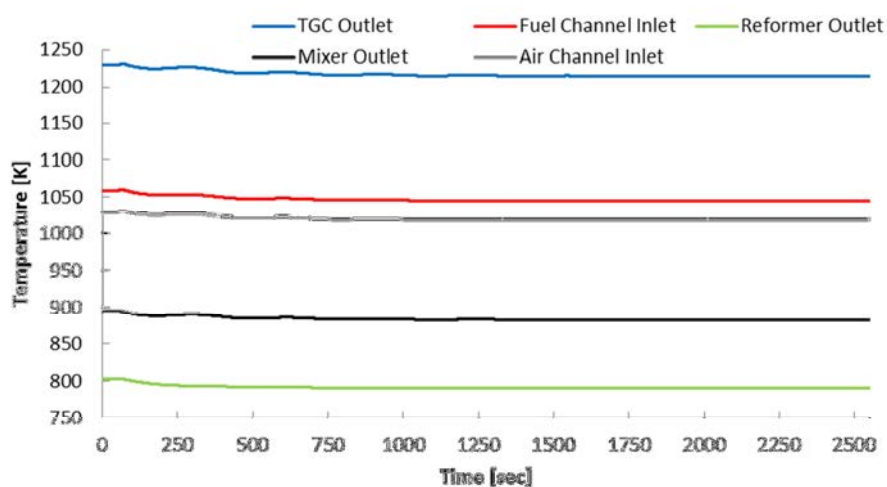
Figure 5-4 SOFC system flow thermal dynamics for ramp from 0.5 to 0.4 [A/cm^2]

Figure 5-4 details the temperatures of select state points in the system. The coupling between SOFC anode outlet and inlet is illustrated where the fuel channel inlet temperature is changing due to the AGR and recuperative heat exchangers. Since the reformer operates adiabatically, its thermal mass dampens out the fuel gas temperature dynamics thereby helping to manage the coupled oscillations at the stack. The reformer appears to have a relatively simple 1st order response with a ±1% settling time of 1322

[s]. The reformer response is actually oscillatory due to the oscillating inlet temperature, but the resolution of the figure does not transmit these small oscillations. Although there is a transient response in the system components, the magnitude of these changes are small with the reformer temperature decreasing only 1.7% and TGC outlet temperature decreasing 1.2%. Compared to the results in Section 3.2.2, the system thermal dynamics are about 230% longer and the system electrical dynamics are about 550% longer.

5.3.2   0.5 to 0.6 [A/cm^2] Current Ramp

Figure 5-5 details the electrical dynamics of the SOFC system for a 50 second current ramp from 0.5 to 0.6 [A/cm^2] with constant fuel utilization and air stoichiometric ratio. The ±1% settling time for the net DC power output is 769 [s] or about 13 minutes. Also seen in Section 3.2.2, an increase in current load has faster dynamics than a 20% decrease in load. This 20% increase in current load results in an 18.1% increase in power output with a final value of 54.4 [kW$_e$]. The oscillatory dynamics seen in the 20% decrease in current load are hardly visible, suggesting that the response is much more docile at lower efficiencies. As opposed to the stand-alone SOFC stack response, there is no overshoot in the power output which results in lower stresses on the power conditioning while converting the DC power to useable AC power for the building.

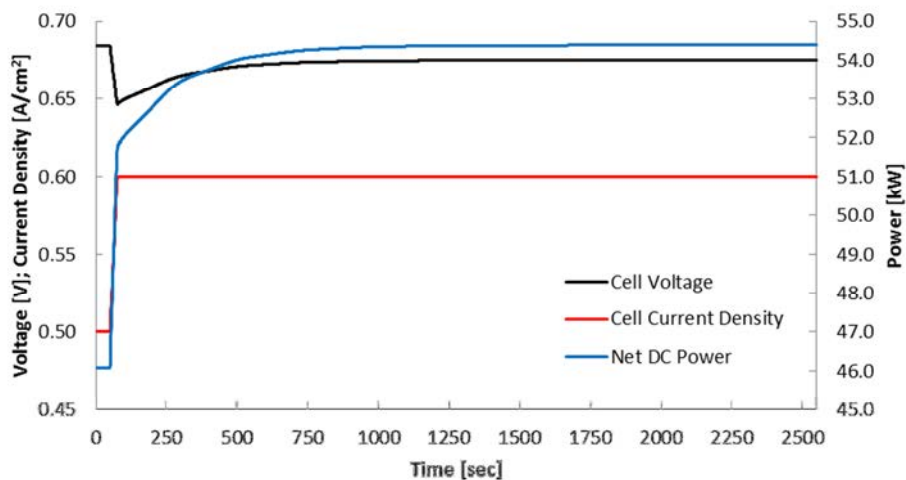

Figure 5-5 SOFC system electrical dynamics for ramp from 0.5 to 0.6 [A/cm2]

Figure 5-6 shows the thermal response of the in-system SOFC stack for this current load change. The average PEN temperature increases due to the increasing amount of redox reaction occurring in the cell and increasing gas inlet temperatures. The average PEN temperature settles within 1% of its steady state value of 1048 [K] in 1046 [s]. The fuel channel outlet temperature settles within 1% of its steady state value of 1160 [K] in the same time. The oscillations of the outlet gas temperatures are less defined than the previous case, further enforcing the correlation between lower efficiency operation and simpler dynamic response.
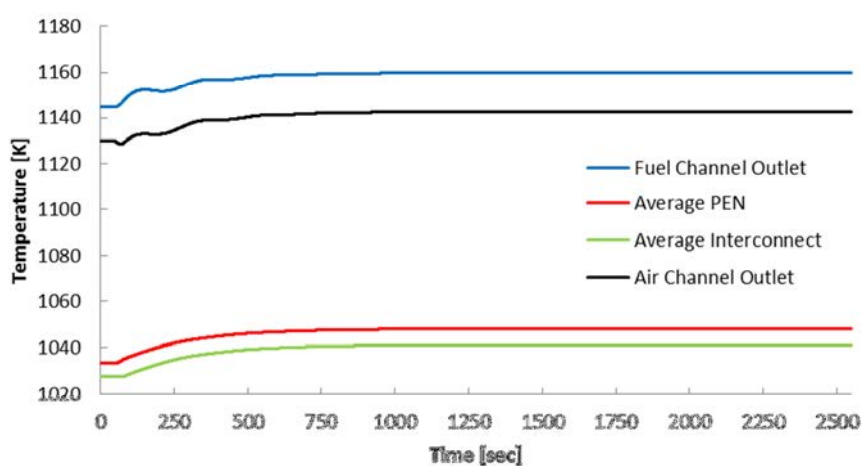

Figure 5-6 In-system SOFC stack thermal dynamics for ramp from 0.5 to 0.6 [A/cm^2]

5.3.3   0.5 to 0.3 [A/cm^2] Current Ramp

Figure 5-7 shows the electrical dynamics of the SOFC system for a 50 second current ramp from 0.5 to 0.3 [A/cm^2] with constant fuel utilization and air stoichiometric ratio. This 40% decrease in current load results in a 1% settling time for net power output of 1543 [s] which is only about a minute longer than the 20% reduction case. However, the response is much more defined in its oscillations which are driven by the more dramatic and longer thermal dynamics of the SOFC stack at this higher efficiency operating condition. The results for the 0.5 to 0.3 [A/cm^2] and the 0.5 to 0.4 [A/cm^2] current steps in the stand-alone SOFC cases (see Section 3.2.2) are not as different as these system results, which signifies that the anode outlet/inlet coupling through AGR

and TGC heat recuperation is negatively affecting the thermal and electrical response of the system.
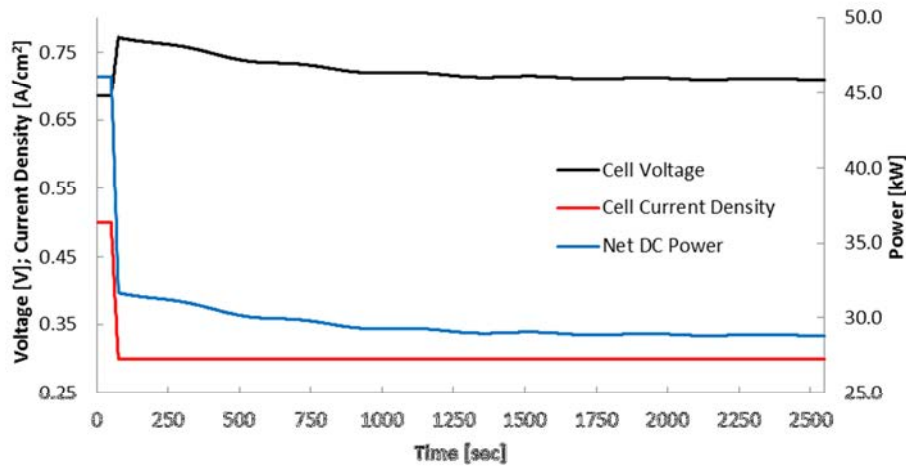

Figure 5-7 SOFC system electrical dynamics for ramp from 0.5 to 0.3 [A/cm^2]

5.3.4   0.3 to 0.24 [A/cm^2] Current Ramp

The negative impact of recycled stream coupling on system performance is further evidenced in Figure 5-8 which shows the electrical dynamics of the SOFC system for a 50 second current ramp from 0.3 to 0.24 [A/cm^2] with constant fuel utilization and air stoichiometric ratio. This 20% decrease in current load results in a 1% settling time for net power output greater than 7000 [s]. As seen in the figure, the system is oscillating, seemingly without any dampening at all. The system is so under-damped at this operating point that capturing the full response computationally is estimated to take at least 35 hours (this 7000 [s] simulation needed 24 hours). The results for the 0.3-0.24 [A/cm^2] stand-alone SOFC case (see Section 3.2.2) was not as oscillatory; however, the system coupling is creating a dramatically under-damped system response. Removing the AGR component of the system or including a bleed valve on the TGC exhaust would help to manage and control this response. Nevertheless, a control system is needed, especially for high efficiency operation such as this. Such oscillation in power output will likely damage the power conditioning equipment that makes the SOFC system and building integration possible.
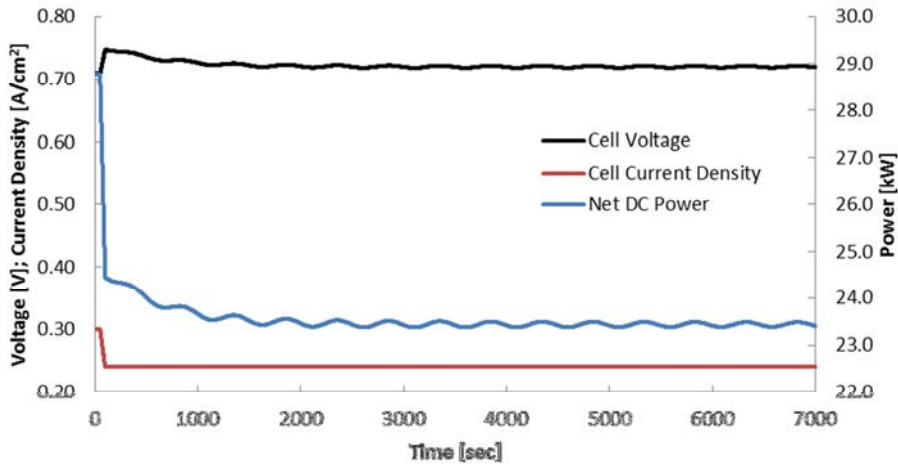
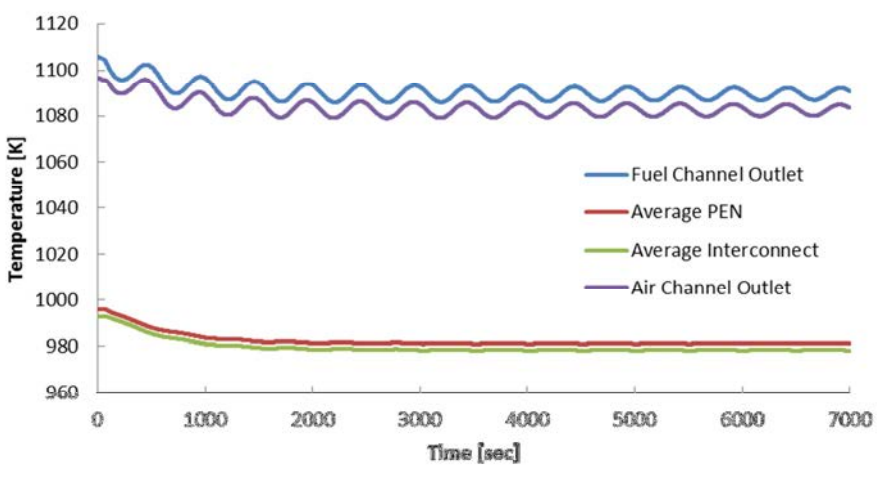Figure 5-8 SOFC system electrical dynamics for ramp from 0.3 to 0.24 [A/cm^2]

Figure 5-9 In-system SOFC stack thermal dynamics for ramp from 0.3 to 0.24 [A/cm^2]
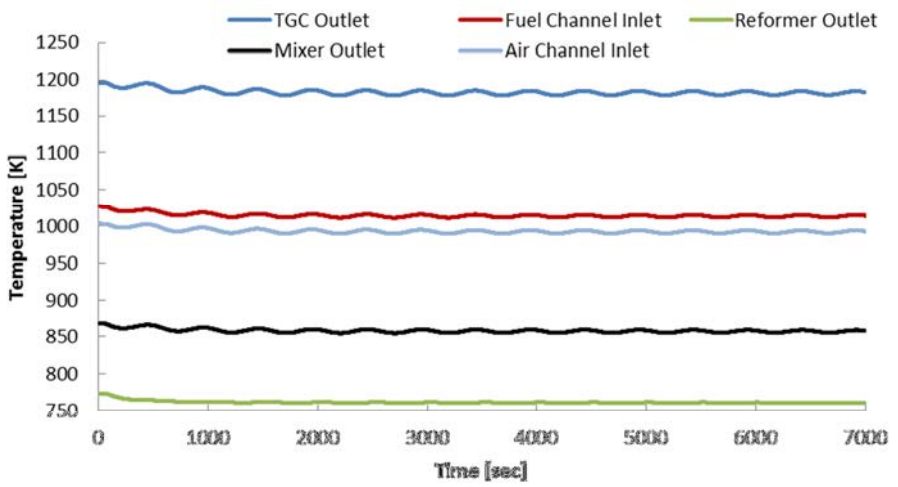

Figure 5-10 SOFC system flow thermal dynamics for ramp from 0.3 to 0.24 [A/cm^2]

Figure 5-9 shows the SOFC stack thermal dynamics for this case. The dampening, however small, is apparent here where the oscillations are slightly diminishing in magnitude with time. The average PEN temperature is oscillating as well, which is undesirable for the stack, where fast and violent dynamics such as this can create thermal gradients that damage the stack and decrease the lifespan of the stack. Figure 5-10 further details the system thermal dynamics which are oscillating as the SOFC outlet temperatures are. There is little dampening available for the flow in the SOFC where mass transport is much too fast to dampen the thermal oscillations through the system. Again, it is evident that a control system is needed to dampen the system. Murshed et al. [23] successfully integrated a non-linear model predictive control algorithm to maximize net DC power output of an SOFC system that also reduces the length of thermal and electrical responses of the system. Aguiar et al. [4] included a PID control strategy to change air flow rates in order to obtain a desired fuel channel outlet gas temperature. With proper tuning and adjustment, such a strategy such as these may prove successful in dampening SOFC system oscillations.

5.3.5 0.5 [A/cm^2] Methane Flow Rate Ramp

As a building integrated system, the produced TER is important in dictating how the system can be integrated. To investigate thermal-to-electric ratios possible and the dynamics in changing the TER, the methane flow rate was ramped from 7 to 9 [kg/hr] in 50 [s] while maintaining a 0.5 [A/cm^2] cell current density and keeping all else constant. Figure 5-12 displays the thermal dynamics of the SOFC system streams. As expected, the temperature at the tail gas combustor outlet increases during the mass flow ramp but then begins to oscillate while slowly approaching steady state. The SOFC inlet streams and reformer follow the same trend. The mixer outlet temperature decreases during the mass flow ramp since more cool methane is entering before the increased mass flow can circulate through the anode and back to the mixer. Following this, the mixer outlet also oscillates with the AGR, which is shown in Figure 5-12.

In Figure 5-12, the anode and cathode exhaust temperatures are shown to not follow the trend of the TGC outlet at first, but only increase very slightly before

decreasing into a large oscillation trend similar to the TGC outlet. The exhaust temperatures only increase slightly since the majority of the increased SOFC inlet thermal energy is absorbed by the PEN structure, as evidenced by the red line, and the increased total rate of steam reforming due to increased methane concentration. The increasing outlet temperatures then decrease as the increasing heat sink of steam reforming dominates fuel channel heat balance. In addition, the temperature profile in the PEN changes with the shifting composition and reaction rate profiles, essentially becoming more U-shaped than J-shaped and reducing the amount of heat transfer to the gas flows at the cell exit. As the average PEN temperature slowly increases with the additional thermal energy available in the inlet streams and the inlet stream temperatures themselves increase due to shifting heat transfer rates in the heat exchangers, the outlet stream temperatures also increase, resulting in the oscillation.
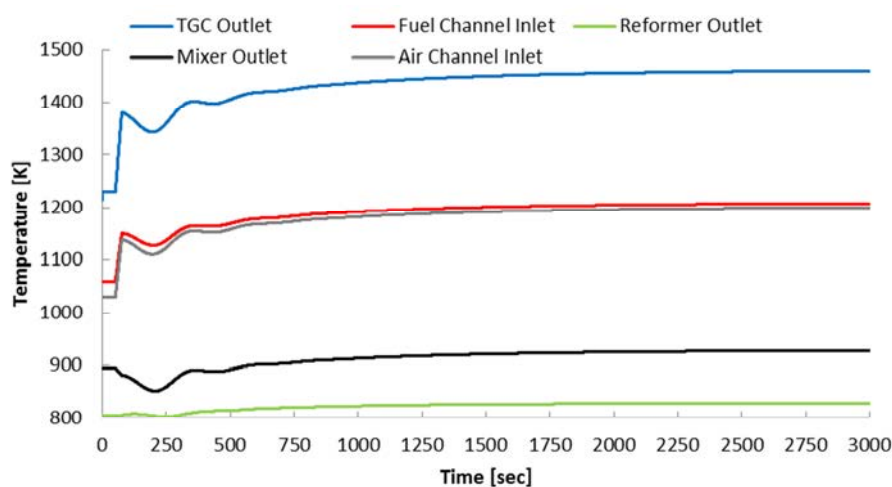
Figure 5-11 SOFC system flow thermal dynamics for methane mass flow ramp from 7 to 9 [kg/hr]

The increasing PEN temperature results in an increase in cell voltage, as shown in Figure 5-13. The voltage and power output follow the increasing mass flow rate of fuel and continues to increase afterward with the increasing PEN temperature. This increasing temperature results in smaller overpotentials and improved electrical efficiency. However, this comes at the cost of lower fuel utilization which is only 46.7% in the SOFC. The overall system electrical efficiency is 47.3% with a net production of 59.1 [kW$_e$]. By adding a heat recovery loop and exhausting the gases at 120 [C], a nominal

70% heat recovery effectiveness brings the system efficiency to 86.3% with a TER of 0.83. Therefore, although the fuel utilization may not be acceptable at first glance, the system CHP efficiency is higher with this increased methane flow rate. In addition, although this case was run with the intention of increasing TER above 1, TER was only increased 10.7% and the magnitude of thermal energy recovery was increased 41.2%.
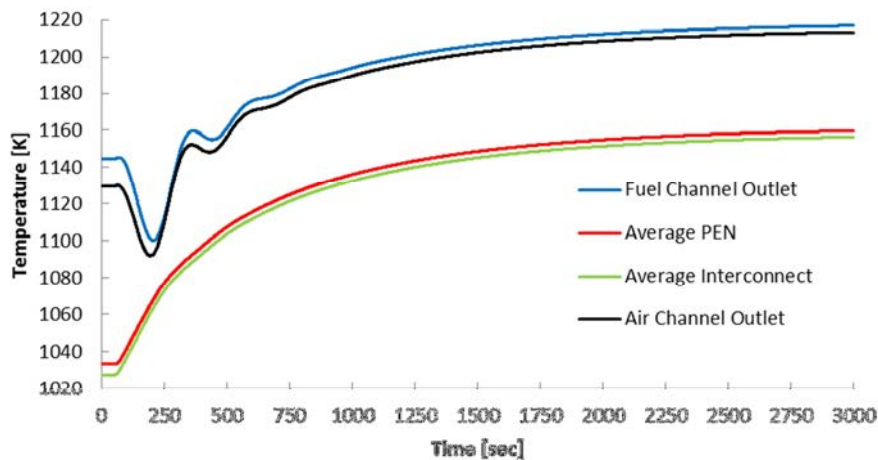
Figure 5-12 In-system SOFC stack thermal dynamics for methane mass flow ramp from 7 to 9 [kg/hr]
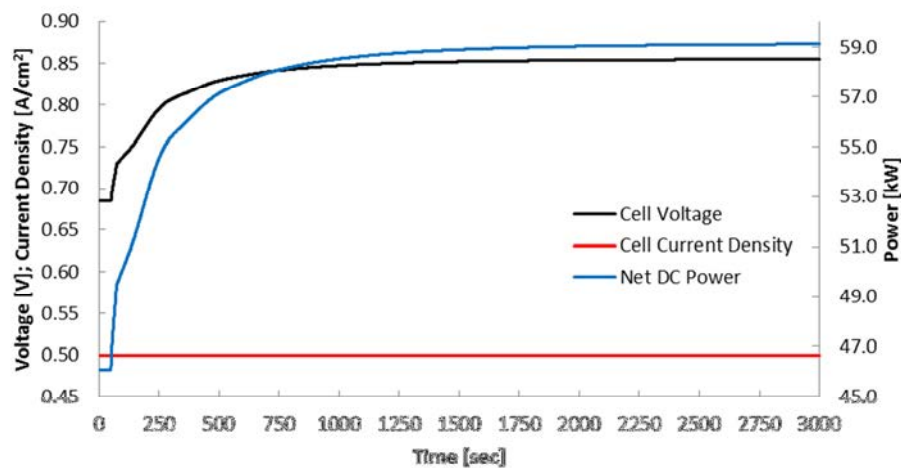

Figure 5-13 SOFC system electrical dynamics for methane mass flow ramp from 7 to 9 [kg/hr]

Table 5-4 presents the steady state operation of the SOFC system at this lower fuel utilization. It is interesting to note that the reformer is also operating at a higher temperature and appropriately converting more methane than in the higher fuel utilization

case at 12.2% compared to 10.9%. This reduces gradients within the stack by reducing the amount of steam reforming required in the stack and allowing for more distributed redox reaction rates and solid and gas temperatures.

Table 5-4 SOFC system state points at 0.5 [A/cm^2] and fuel utilization of 46.7%

State Point	Temp. [C]	Flow Rate [kg/hr]	Molar Composition							Pressure [Bar]	Elec. Power [kW$_e$]
			CH$_4$	CO$_2$	CO	H$_2$O	H$_2$	N$_2$	O$_2$		
1	27	9.00	1.00	0.00	0.00	0.00	0.00	0.00	0.00	1.000	-
2	51	9.00	1.00	0.00	0.00	0.00	0.00	0.00	0.00	1.317	-
3	655	40.92	0.25	0.12	0.13	0.27	0.23	0.00	0.00	1.317	-
4	555	40.92	0.21	0.17	0.09	0.17	0.36	0.00	0.00	1.317	-
5	935	40.92	0.21	0.17	0.09	0.17	0.36	0.00	0.00	1.317	-
6	27	687.50	0.00	0.00	0.00	0.00	0.00	0.79	0.21	1.000	-
7	58	687.50	0.00	0.00	0.00	0.00	0.00	0.79	0.21	1.317	-
8	927	687.50	0.00	0.00	0.00	0.00	0.00	0.79	0.21	1.317	-
9	944	63.85	0.00	0.15	0.18	0.36	0.31	0.00	0.00	1.315	-
10	944	31.92	0.00	0.15	0.18	0.36	0.31	0.00	0.00	1.315	-
11	944	31.92	0.00	0.15	0.18	0.36	0.31	0.00	0.00	1.315	-
12	940	664.58	0.00	0.00	0.00	0.00	0.00	0.81	0.19	1.298	-
13	1188	696.50	0.00	0.02	0.00	0.05	0.00	0.77	0.16	1.298	-
14	1144	696.50	0.00	0.02	0.00	0.05	0.00	0.77	0.16	1.298	-
15	483	696.50	0.00	0.02	0.00	0.05	0.00	0.77	0.16	1.298	-
16	944	31.92	0.00	0.15	0.18	0.36	0.31	0.00	0.00	1.317	-
17	-	-	-	-	-	-	-	-	-	-	59.1
18	-	-	-	-	-	-	-	-	-	-	6.6

5.4   Reliability Considerations

The durability of SOFC stacks must be considered and preserved during steady state and dynamic operation. Due to the brittle materials and sensitive catalyst present in the stack, certain operating conditions can destroy or damage the stack and its chemically active surfaces. Thermal stresses caused by temperature gradients (above about 1 [°C/mm]) in the cell structure can result in delamination and failure of the PEN solid. In addition, rapid thermal cycling can impart thermal stresses on manifold seals and PEN solid that result in material failure. Catalyst deactivation must also be considered as low voltage (less than about 0.6 [V]) and high hydrocarbon presence can destroy the chemical activity of the catalyst [8].

In the cases studied in this research, cell voltage was maintained sufficiently high (above 0.65 [V]) to avoid electro-oxidation of the catalyst by supplying gases at high temperatures to the stack. As methane is the highest considered hydrocarbon in this research and there is never a predicted molar fraction of methane above 0.25 at the stack fuel channel inlet, there is no concern of coke deposition. In addition, thermal gradients in the PEN solid were analyzed to be within the maximum acceptable value. Due in part to the planform layout, the maximum temperature gradient in the PEN solid was found to be no greater than 0.43 [°C/mm]. However, there is a concerning amount of rapid thermal cycling in the SOFC stack as evidenced by Figure 5-14. An in-depth analysis of stack design and individual parts is necessary to quantify the effects of this cycling on the stack durability and reliability. However, the periodicity of about 8 minutes and continual oscillation and cycling provides an intuitional response that this operation may seriously damage the PEN solid or other areas like manifolding seals or metal-ceramic interfaces.
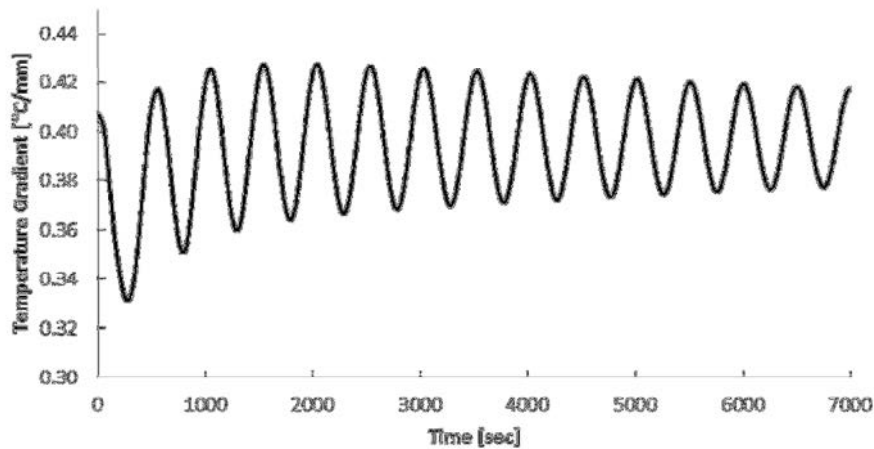

Figure 5-14 Maximum temperature gradient in PEN solid for current density ramp from 0.3 to 0.24 [A/cm^2]

5.5 SOFC System Operation Summary

A summary of the thermal and electrical settling times of the studies presented in Figure 5-2 to Figure 5-13 is presented in Table 5-5. In brief, the following conclusions on SOFC system dynamics are made:

- A control system is necessary to dampen the system's thermal and electrical responses, especially for low load operation, or removal of intra-system coupling is required for more stable transient response. Temperature control methods must be in place to avoid deleteriously high temperature operating regimes, for example, complying with service temperature limits of heat exchangers, combustors and recycle blowers.

- SOFC stack dynamic trends in terms of settling time translate to the system response, where lower SOFC efficiency results in faster dynamic responses.

- Generally for the load range presented, a current load change will result in a proportional net DC power output change.

- Increasing the system TER above 1.0 may require additional equipment and controls.

- Net DC power output takes on the order of ~500-1500 [s] to get to steady state operation for the load range presented, making the system-building integration problem more difficult than suggested by the SOFC stack dynamics.

Table 5-5 Dynamic SOFC system settling time results

Initial Current Density [A/cm^2]	Final Current Density [A/cm^2]	Strategy	Percent Change	±1% Thermal Settling Time [s]	±1% Electrical Settling Time [s]	
					Power	Voltage
0.5	0.5	Flow rate ramp	0%	2600	1738	1738
0.5	0.6	A	+20%	1046	769	1307
0.5	0.4	A	-20%	1500	999	2096
0.5	0.3	A	-40%	1938	1543	2445
0.3	0.24	A	-20%	>7000	>7000	>7000

CHAPTER 6

CONCLUSIONS

Dynamic SOFC stack and system models have been created to investigate the dynamic responses of an SOFC stack and system, examine the potential of SOFC systems as load-following units, and develop initial insights regarding the effects of system design on SOFC system dynamic response. The system model includes steady-state heat exchanger, compressor, mixer, and tail gas combustor models, and dynamic pre-reformer and SOFC stack models. A primary motivation for this work is to develop dynamic modeling tools to simulate the transient operation of SOFC systems intended for commercial building applications. In particular, optimization studies [27][30] have shown that the cost optimal dispatch of a distributed SOFC-CHP system in a commercial building can be based on load-following operating strategies. Furthermore, a literature review has shown that previous investigations into SOFC system dynamic capabilities have either not had a high-fidelity SOFC stack model or have not captured the intra-system coupling due to exhaust heat recuperation or gas recycle.

The SOFC dynamic stack model developed was one-dimensional, co-flow configuration, and internal reforming capable. Linear extrapolation between the cell and stack levels was assumed. Dynamic mass and energy balances were developed around spatially discretized control volumes. In addition, a momentum balance was approximated using a relationship between flow rate and pressure drop. Activation, concentration and ohmic overpotentials were considered in the electrochemical sub-model. The SOFC stack model integrity was established by benchmarking it with other stack models given in the literature and a maximum error of 2% was found.

In this work, preliminary investigations into the dynamic response of the SOFC stack alone suggest the potential for successful load-following operation in a building

integrated application. The average thermal and electrical settling time for the stack was found to be on the order of seven minutes, while the maximum presented settling time was about 18 minutes for thermal output. Considering most optimization studies are performed using an hourly timestep, this dynamic capability is sufficient for near cost optimal operation. Essentially, the power output demand changes on an hourly basis and the SOFC stack has been shown to have the capability to change power output and settle to steady state well within that hour.

Interesting stack thermal and electrical dynamics were also revealed, however. For instance, slight oscillations were observed in stack thermal and electrical dynamic response. These oscillations are theorized to be due to a complex coupling between internal solid temperature and reaction rate (reforming reactions and current density) distributions axially through the cell. In addition, the nature of the stack dynamic response changed according to the efficiency or power output. At high efficiency or low power output, the settling times were longer and oscillations more defined. In contrast, low efficiency or high power output resulted in shorter dynamic response and less defined oscillations.

The dynamics of the SOFC system were observed to be much longer and oscillatory. On average, both the stack thermal and electrical responses were found to be longer when the stack was integrated into a complete system than as a stand-alone component. In particular, the stack settling time was found to be about 100% longer in duration and the electrical power output settling time was shown to be about 400% longer in duration when operating in the SOFC system. In addition, oscillations in system response were shown to be amplified as compared to the stand alone stack investigation. Although this system oscillation originates in the inherent stack oscillations, this amplification is due to the coupling between stack outlet conditions, temperature especially, and stack inlet conditions brought on by anode gas recycle and exhaust gas heat recuperation. The system is shown to be less dampened with these design elements. Interestingly, the adiabatic external reformer actually serves to dampen the system due to the thermal mass absorbing and desorbing heat during the oscillations. The fuel and air

supply stream reheat heat exchangers, however, reintroduce these oscillations due to the oscillating nature of the exhaust gases through the tail gas combustor.

One case is presented where the SOFC system appears to have lost all of its dampening abilities, suggesting a severely non-linear relationship between system dampening and operating conditions. This necessitates a control system that can artificially dampen the system as a SOFC system settling time of over two hours is insufficient for near cost optimal building integrated system operation. An actuator for such a system could be a controlled bleed or diverter valve on the TGC exhaust gas stream to allow for less heat transfer at the heat exchangers. Or, a controlled fresh air feed stream to the TGC inlet will allow for control of TGC exhaust temperatures.

These SOFC system results suggest that a system redesign may enable faster and more stable thermal and electrical dynamic performance. For example, moving the fuel supply stream reheat heat exchanger upstream of the external reformer would allow for the reformer to dampen the thermal oscillations before SOFC stack fuel stream inlet. In addition, anode gas recycle, although it provides improved steady state SOFC stack performance, is not assisting in improving system dynamic response. Without AGR, there will be less coupling between the outlets and inlets of the SOFC stack and oscillations may be reduced.

6.0   Recommendations for Future Work

Although many interesting SOFC system dynamics have been revealed much work still remains to enable these systems as building integrated DG systems. Control systems are necessary to maintain acceptable operating conditions within the stack and system components. Control systems may also be able to improve the dynamic settling time of the system and reduce the oscillations in the thermal and electrical response of the system. Detailed control system investigations would identify what dynamic capabilities could be extracted from a SOFC system.

The impact of SOFC system design on dynamic response should also be investigated. As shown in this research, AGR and heat exchanger arrangements are

tightly coupling the system components and resulting in oscillations that are impacting the time to reach steady state. Detailed dynamic analysis of assorted system configurations, including design concepts like separate steam feed to the reformer rather than AGR and different heat exchanger arrangements, should be performed to identify the optimal SOFC system design for dynamic performance.

The impact of SOFC stack and system assumptions should also be investigated. First, heat exchanger effectiveness is assumed to be constant across the system operating conditions. This is unrealistic in that it essentially assumes that the heat exchanger geometry is changing dynamically with the system conditions. An appropriate heat exchanger UA should be designed for and the heat exchanger models updated accordingly to utilize the ε–NTU method. Secondly, the external steam reformer model fidelity should be increased by integrating a spatially discretized model into the SOFC system model. The model presented in this research is simplistic in its approach and an approach similar to the presented SOFC stack model should be implemented. Thirdly, pressure drop through system components as a function of mass flow rate should also be included in the system model. This would create a more complete SOFC system model that captures the pressure effects of changing operating conditions. Next, the effects on dynamic performance by SOFC stack designs should be investigated. Iterative studies on planform dimensions and aspect ratio, flow direction (counter-flow, co-flow, cross-flow), and PEN solid dimensions (electrode and electrolyte thicknesses) may present an optimal stack design that may improve upon the performance presented in this research. Lastly, the SOFC stack model can be improved by adding manifolding considerations and interconnect current collection losses. The presented model assumes equivalent cell operation throughout the SOFC stack as well as uniform distribution of flow to the cells in the stack and zero electrical losses in the interconnect plates. These assumptions are overestimating stack performance. Ideally, a three-dimensional stack and manifold model should be created to, at the very least, verify these simplifying assumptions and investigate the effects of non-uniform cell operation in the stack on system dynamic performance.

Finally, the dynamic SOFC stack model should be experimentally validated. Dynamic SOFC stack experimental data are scarce, but this is necessary to ensure the accuracy and precision of the stack model. This research assumes that the simulated dynamic results in literature are valid. Transient data that would prove most valuable for dynamic stack validation are: inlet and outlet gas and solid temperatures, inlet and outlet fuel composition, and voltage and current output of the stack.

REFERENCES CITED

[1] Achenbach, E. (1994). Three-dimensional and time-dependent simulation of a planar solid oxide fuel cell stack. *Journal of Power Sources, 49*, 333-348.

[2] Achenbach, E., & Riensche, E. (1994). Methane/steam reforming kinetics for solid oxide fuel cells. *Journal of Power Sources, 52*, 283-288.

[3] Aguiar, P., Adjiman, C. S., & Brandon, N. P. (2004). Anode-supported intermediate temperature direct internal reforming solid oxide fuel cell. I: Model-based steady-state performance. *Journal of Power Sources, 138*, 120-136.

[4] Aguiar, P., Adjiman, C. S., & Brandon, N. P. (2005). Anode-supported intermediate-temperature direct internal reforming solid oxide fuel cell. II: Model-based dynamic performance and control. *Journal of Power Sources, 147*, 136-147.

[5] Bhattacharyya, D., & Rengaswamy, R. (2009). A Review of Solid Oxide Fuel Cell (SOFC) Dynamic Models. *Industrial and Engineering Chemistry Research, 48*, 6068-6086.

[6] Braun, R. J. (2002). *Optimal Design and Operation of Solid Oxide Fuel Cell Systems for Small-scale Stationary Applications.* (Doctor of Philosophy), University of Wisconsin - Madison.

[7] Braun, R. J., Klein, S. A., & Reindl, D. T. (2006). Evaluation of system configurations for solid oxide fuel cell-based micro-combined heat and power generators in residential applications. *Journal of Power Sources, 158*, 1290-1305.

[8] Braun, R. J., Vincent, T. L., Zhu, H., Kee, R. J. (2012). Analysis, Optimization, and Control of Solid-Oxide Fuel Cell Systems. *Advances in Chemical Engineering, 41*.

[9] Carrette, L., Friedrich, K. A., & Stimming, U. (2001). Fuel Cells - Fundamentals and Applications. *Fuel Cells, 1*, 5-39.

[10] Ding, Y., & Alpay, E. (2000). Adsorption-enhanced steam-methane reforming. *Chemical Engineering Science, 55*, 3929-3940.

[11] Ehrig, R. (2000). LIMEX (Version 4.2A1). Berlin, Germany: Konrad-Zuse-Zentrum fuer Informationstechnik Berlin (ZIB).

[12] Electric Power Monthly March 2012. (2012). (DOE/EIA-0226). from U.S. Energy Information Administration

[13] Engineering Equation Solver (EES). (2011). Middleton, Wisconsin: F-Chart Software.

[14] Iora, P., Aguiar, P., Adjiman, C. S., & Brandon, N. P. (2005). Comparison of two IT DIR-SOFC models: Impact of variable thermodynamic, physical, and flow properties. Steady-state and dynamic analysis. *Chemical Engineering Science, 60*, 2963-2975.

[15] Jiang, W., Fang, R., Khan, J. A., & Dougal, R. A. (2006). Parameter setting and analysis of a dynamic tubular SOFC model. *Journal of Power Sources, 162*, 316-326.

[16] Kattke, K. J. (2010). *The Development of Novel, High-Fidelity Modeling Tools for Thermal Management of Planar and Tubular Solid Oxide Fuel Cell Systems.* (Master of Science), Colorado School of Mines, Golden, CO.

[17] Kazempoor, P., Ommi, F., & Dorer, V. (2011). Response of a planar solid oxide fuel cell to step load and inlet flow temperature changes. *Journal of Power Sources, 196*, 8948-8954.

[18] Kee, R. J., Korada, P., Walters, K., & Pavol, M. (2002). A generalized model of the flow distribution in channel networks of planar fuel cells. *Journal of Power Sources, 109*, 148-159.

[19] Li, J., Cao, G.-Y., Zhu, X.-J., & Tu, H.-Y. (2007). Two-dimensional dynamic simulation of a direct internal reforming solid oxide fuel cell. *Journal of Power Sources, 171*, 585-600.

[20] Meusinger, J., Riensche, E., & Stimming, U. (1998). Reforming of natural gas in solid oxide fuel cell systems. *Journal of Power Sources, 71*, 315-320.

[21] Moran, M. J., & Shapiro, H. N. (2008). *Fundamentals of Engineering Thermodynamics* (6 ed.). Hoboken, New Jersey: John Wiley & Sons, Inc.

[22] Murshed, A. M., Huang, B., & Nandakumar, K. (2007). Control relevant modeling of planer solid oxide fuel cell system. *Journal of Power Sources, 163*, 830-845.

[23] Murshed, A. M., Huang, B., & Nandakumar, K. (2010). Estimation and control of solid oxide fuel cell system. *Computers and Chemical Engineering, 34*, 96-111.

[24] O'Hayre, R., Cha, S., Colella, W., & Prinz, F. B. (2009). *Fuel Cell Fundamentals* (2 ed.). New York: John Wiley & Sons, Inc.

[25] Padulles, J., Ault, G. W., & McDonald, J. R. (2000). An integrated SOFC plant dynamic model for power systems simulation. *Journal of Power Sources, 86*, 495-500.

[26] Press, W. H., Teukolsky, S. A., Vetterling, W. T., & Flannery, B. P. (1992). *Numerical Recipes in Fortran: The Art of Scientific Computing* (2 ed.). New York: Cambridge University Press.

[27] Pruitt, K. A., Braun, R. J., & Newman, A. M. (2012). *Optimal Design and Dispatch of Distributed Generation Systems: Evaluating Shortfalls in Existing Approaches*. Division of Economics & Business. Colorado School of Mines. Golden, CO.

[28] Qi, Y., Huang, B., & Luo, J. (2006). *Nonlinear State Space Modeling and Simulation of a SOFC Fuel Cell*. Paper presented at the American Control Conference, Minneapolis, Minnesota, USA.

[29] Reid, R. C., Prausnitz, J. M., & Poling, B. E. (1987). *The Properties of Gases and Liquids* (4 ed.). New York: McGraw-Hill.

[30] Rhuberg, R. (2012). Internal study of building optimization using HOMER. Colorado School of Mines. Golden, CO.

[31] Saarinen, J., Halinen, M., Ylijoki, J., Noponen, M., Simell, P., & Kiviaho, J. (2007). Dynamic Model of 5 kW SOFC CHP Test Station. *Journal of Fuel Cell Science and Technology, 4*, 397-405.

[32] Shah, R. K., & London, A. L. (1978). *Laminar Flow Forced Convection in Ducts*. New York: Academic Press.

[33] Siddiqui, A. S., Marnay, C., Firestone, R. M., & Zhou, N. (2007). Distributed Generation with Heat Recovery and Storage. *Journal of Energy Engineering, 133*, 181-210.

[34] Smith, A. D., Mago, P. J., & Fumo, N. (2011). Emissions spark spread and primary energy spark spread – Environmental and energy screening parameters for combined heating and power systems. *Applied Energy, 88*, 3891-3897.

[35] Stadler, M., Marnay, C., Siddiqui, A., Lai, J., & Aki, H. (2009). *Integrated Building Energy Systems Design Considering Storage Technologies.* Paper presented at the European Council for an Energy Efficienct Economy 2009 Summer Study, La Colle sur Loup, Cote d'Azur, France.

[36] Steam Reforming Catalysts. St. Louis, Missouri: Matros Technologies, Inc.

[37] TRNSYS (Version 17). (2010). Madison, Wisconsin: Solar Energy Laboratory, University of Wisconsin.

[38] Wilke, C. R. (1950). A viscosity equation for gas mixtures. *Journal of Chemical Physics, 18*, 517-519.

[39] Xi, H. (2007). *Dynamic Modeling and Control of Planar SOFC Power Systems.* (Doctor of Philosophy), University of Michigan.

[40] Xu, J., & Froment, G. F. (1989). Methane Steam Reforming, Methanation and Water-Gas Shift: I. Intrinsic Kinetics. *American Institute of Chemical Engineers, 35*, 88-96.

[41] Zink, F., Lu, Y., & Schaefer, L. (2007). A solid oxide fuel cell system for buildings. *Energy Conversion and Management, 48*, 809-818.